ECOLE INTERNATIONALE DE
PHYSIQUE DES PARTICULES ELEMENTAIRES
KUPARI-DUBROVNIK (Yougoslavie)

1977

ANTIPROTON INDUCED REACTIONS

A. FRIDMAN

Centre de Recherches Nucléaires de Strasbourg

DIVISION DES HAUTES ENERGIES
CENTRE DE RECHERCHES NUCLEAIRES
STRASBOURG

INSTITUT DE PHYSIQUE
UNIVERSITE DE BELGRADE
BELGRADE

ANTIPROTON INDUCED REACTIONS

A. FRIDMAN

Centre de Recherches Nucléaires de Strasbourg

Lecture given at the International School of Elementary Particle Physics
KUPARI – 1977

C O N T E N T S

1. INTRODUCTION

The question that one can of course ask is: Why should one study $\bar{p}$ induced reactions? If one takes the attitude that it is worth while to study strong interactions physics, two simple answers can be given to this question. First of all let us note that there is not a great variety of processes which can be investigated, as the targets to which one has acces today are essentially nucleons. Therefore we certainly need to investigate all the possible hadron-hadron interactions if we want to have a complete as possible picture of production phenomena. In this respect $\bar{p}N$ interactions give information which may contribute to a better understanding of production phenomena. The second answer that can be given is that $\bar{p}N$ collisions have a peculiar property. These collisions are one of the most simple ways to study systems having a total baryonic number $B = 0$ and hence to form mesons. Thus $\bar{p}N$ collisions offer the possibility of studying a special class of reactions, the annihilations ones, in which no baryons are present in the final state. Furthermore, for reactions with outgoing baryons, the comparison with pp reactions will certainly be useful for an understanding of multiparticle production in terms of phenomenological models.

In principle, one can also study $B = 0$ systems by means of virtual $\pi\pi$ interactions as illustrated in the following diagram.

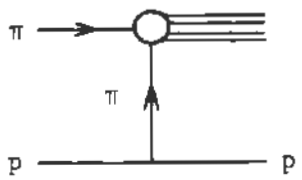

Apart from the uncertainties introduced by the fact that one cannot be sure that one is really dealing with a virtual π, there is also another inconvenience. The $\pi\pi$ initial state is in a definite G-parity state, $G = 1$, while $\bar{p}N$ is in mixture of $G = \pm 1$ states. In this sense $\bar{p}N$ interactions allow a more general study of $B = 0$ systems apart from the fact that it is easier to study real collisions than virtual ones.

Once one is convinced that $\bar{p}$ induced reactions can bring some new insight into strong interactions physics, one may be willing to study $\bar{p}p$ as well as $\bar{p}n$ interactions. These studies are complementary, because different initial isospin ($I = 0,1$ for $\bar{p}p$ and $I = 1$ for $\bar{p}n$) values give access to different charge partitions in the final state. To clarify this point let us give some simple examples by considering reactions with one-pion production, i.e. $\bar{p}p \to \bar{p}p\pi^o$, $\bar{p}n\pi^+$ and $\bar{p}n \to \bar{p}p\pi^-$. In the first case the $\bar{N}\pi$ systems can be emitted in the $I = 3/2, 1/2$ isospin state, whereas the $\bar{p}\pi^-$ in the $\bar{p}n \to \bar{p}p\pi^-$ reaction is always in a $I = 3/2$ state. One sees thus that for studying $I = 3/2$ $\bar{N}\pi$ systems it is more convenient to use the $\bar{p}n \to \bar{p}p\pi^-$ channel instead of the $\bar{p}p \to \bar{N}N\pi$ one.

Moreover the symmetry properties of the initial state, which are different in $\bar{p}p$ and $\bar{p}n$ interactions, lead to investigations of different production features. Let us take a simple example as $\pi^+\pi^-$ pairs production in the reactions $\bar{p}p \to \bar{p}p\pi^+\pi^-$ and $\bar{p}n \to \bar{p}n\pi^+\pi^-$. As will be seen below $\bar{\Delta}^{--}(\bar{p}\pi^-)$ and $\Delta^{++}(p\pi^+)$ will be produced in equal amounts in the $\bar{p}p \to \bar{p}p\pi^+\pi^-$ channel [C-invariance]. In contrast, for the $\bar{p}n \to \bar{p}n\pi^+\pi^-$ reaction one will observe equal amounts of $\bar{\Delta}^{--}(\bar{p}\pi^-)$ and $\Delta^-(p\pi^-)$ [G-invariance]. Therefore the $\bar{p}p \to \bar{p}p\pi^+\pi^-$ reaction will allow us to study the quasi two-body $\bar{p}p \to \bar{\Delta}^{--}\Delta^{++}$ state. Such a study will not easily be made with the $\bar{p}n \to \bar{p}n\pi^+\pi^-$ reaction, where the π^- is resonating alternatively with the $\bar{p}$ or the n to form a $\bar{\Delta}^{--}(\bar{p}\pi^-)$ or a $\Delta^-(n\pi^-)$ resonances (see Fig.1.1). These simple examples merely show that a complementary picture of $\bar{p}$ induced reactions is obtained by studying $\bar{p}p$ and $\bar{p}n$ interactions. In addition, the knowledge of the total $\bar{p}p$ and $\bar{p}n$ cross-sections permits a direct (although tedious) isospin decomposition of the total cross-section.

Let us now state somewhat more precisely what we mean by the symmetry properties which are an essential feature of $\bar{p}N$ interactions. To this end we consider the reaction $\bar{p}p \to 1 + X$ where X is any system recoiling against the outgoing particle denoted by 1. By applying the charge-conjugation operator C to this reaction one obtains $p\bar{p} \to \bar{1} + \bar{X}$. This initial state is almost identical with the former $\bar{p}p$ state. One already foresees that this will lead to some peculiar properties for the final state. In fact, for unpolarized colliding particles the initial $\bar{p}p$ state is an eigenstate of the $R_N(\pi)C$ operator. Here $R_N(\pi)$ represents the π rotation operator around any axis perpendicular to the incoming $\bar{p}$ line of flight[1]. This is vizualised in Fig.1.2, which shows that after the $R_N(\pi)C$ operation, one obtains the same initial state, but 1 is transformed into $\bar{1}$

emitted in a different direction. Defining a right-handed coordinate system, where the z and x axes are along the beam direction and the normal $\bar{N}$, respectively (see Fig.1.2) one sees that 1, which is emitted with polar θ and azimuthal φ angles, is transformed into $\bar{1}$, with the corresponding polar and azimuthal emission angles $\pi - \theta$ and $-\varphi$, respectively. One may thus relate the c.m. angular distribution (W) of 1 with that ($\bar{W}$) of $\bar{1}$, i.e.[1]

$$W(1, \theta, \varphi) = \bar{W}(\bar{1}, \pi - \theta, -\varphi).$$

Two cases can occur: the transformed $\bar{1} + \bar{X}$ system can be identical with or different from the original $1 + X$ one. When the final states are identical ($\bar{1} + \bar{X} = 1 + X$), one will have a relation between c.m. distributions of particles belonging to the same reaction. If the states differ one will have relations between different reactions. In this case $\bar{1} + \bar{X}$ will be as frequent as $1 + X$; hence the reactions $\bar{p}p \to 1 + X$ and $\bar{p}p \to \bar{1} + \bar{X}$ must have equal cross-sections. Let us note that 1 can be composed from a set of particles. Thus if 1 is, for instance, a resonance Δ^{++}, one must also have an equal amount of $\bar{\Delta}^{--}$ in the same reaction or the conjugated one $\bar{p}p \to \bar{1} + \bar{X}$.

For the $\bar{p}n$ interaction the situation is somewhat more complicated, as the $\bar{p}n$ state is an eigenstate of the $U = T_I(\pi)R_N(\pi)C$ operator (see Fig.1.2). Here $T_I(\pi)$ is the π rotation operator around the first (or x) axis in isospin space. This operator changes essentially a particle into its charge symmetric one $T_I(\pi)a = a_S$. [The $CT_I(\pi)$ operation is essentially the G operator]. Now the U operator changes the $1 + X$ final state into the $\bar{1}_S + \bar{X}_S$ state [note that $(\bar{1})_S = \bar{1}_S$]. In the same manner as for the $\bar{p}p$ case one will obtain a relation between the $\bar{p}n \to 1 + X$ and $\bar{p}n \to \bar{1}_S + X_S$ reaction such as (See the example of Fig.1.3),

$$W(1, \theta, \varphi) = \bar{W}(\bar{1}_S, \pi - \theta, -\varphi).$$

This time there are the states $1 + X$ and $\bar{1}_S + \bar{X}_S$ which are produced with equal cross-sections if $1 + X \neq \bar{1}_S + \bar{X}_S$. Table 1.1 summarizes some of the relations obtained from the symmetries just discussed.

TABLE 1.1 - Some consequences of the C-invariance and G-invariance for $\bar{p}p$ and $\bar{p}n$ collisions, respectively.

$\bar{p}p$	$\bar{p}p \to 1 + X$ and $\bar{p}p \to \bar{1} + \bar{X}$ have same cross sections if $1 + X \neq \bar{1} + \bar{X}$ 1 is as frequent as $\bar{1}$ in the same reactions if $1 + X = \bar{1} + \bar{X}$ $W(1, \theta, \varphi) = \bar{W}(\bar{1}, \pi - \theta, -\varphi)$ Examples : $\bar{p}p \to \pi^+\pi^-\pi^o$: c.m. angular distribution of π^+ and π^- reflected from one another ; c.m. angular distribution of π^o is symmetric $\bar{p}p \to \bar{p}p\pi^+\pi^-$: same amount of $\bar{\Delta}^{--}$ and Δ^{++} c.m. angular distribution of $\bar{p}$ (π^-) is reflected from the p(π^+) distribution
$\bar{p}n$	$\bar{p}n \to 1 + X$ and $\bar{p}n \to \bar{1}_S + \bar{X}_S$ have the same cross sections if $1 + X \neq \bar{1}_S + \bar{X}_S$ 1 is as frequent as $\bar{1}_S$ in the same reaction if $1 + X = \bar{1}_S + \bar{X}_S$ $W(1, \theta, \varphi) = \bar{W}(\bar{1}, \pi - \theta, -\varphi)$ Examples : $\bar{p}n \to \pi^-\pi^-\pi^+$: all the c.m. angular distributions are symmetric $\bar{p}n \to \bar{p}n\pi^+\pi^-$: same amount of $\bar{\Delta}^{--}$ ($\bar{p}\pi^-$) and Δ^-($n\pi^-$); c.m. angular distribution of $\bar{p}$ is reflected from those of the n

Taking the attitude that $\bar{p}$ interactions should be studied, we will discuss in the following some specific aspects of $\bar{p}$ induced reactions. Before doing this we will first look into the difficulties introduced by using a complex nucleus in order to study interactions on neutrons. Then we will discuss resonance hunting in $\bar{p}n$ reactions, which is certainly one of the most important feature related to the analysis of inelastic reactions.

We will not attempt here to make a review of multiparticle production phenomena in $\bar{p}N$ interactions which have been extensively studied in recent years. Instead we will discuss some two-body final states shoving thus that even in this simple case many problems remains unvolved. We will then discuss the problems of total and annihilation $\bar{p}N$ cross-sections. Afterward the multiplicity distributions as well as their correlated statistical moments will be investigated. Finally, we will present some general features of annihilation reactions.

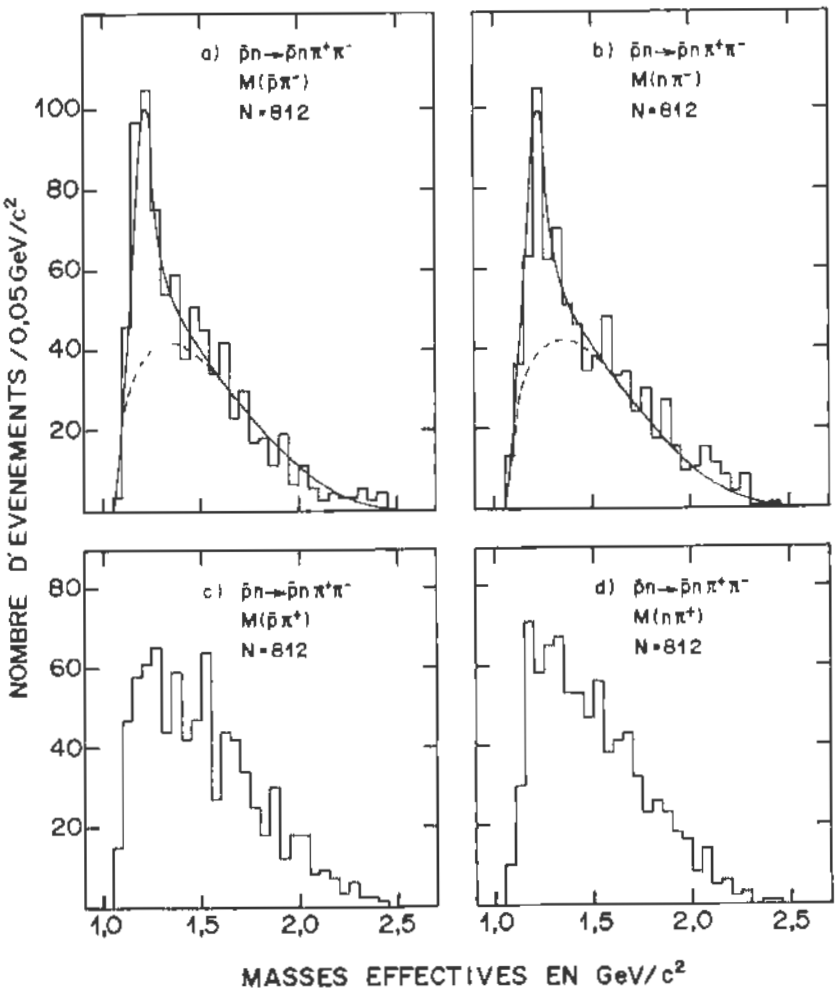

Figure 1.1

The $N\pi$ [$M(N\pi)$] and $\bar{N}\pi$ [$M(\bar{N}\pi)$] effective mass distributions for the $\bar{p}n \to \bar{p}n\pi^+\pi^-$ reaction at 5.55 GeV/c [taken from Phys. Rev. D6, 767 (1972)]. The full curves are obtained by fitting the data with incoherent mixture of phase space (dashed lines) and Breit - Wigner functions due to the $\Delta(1236)$ and $\bar{\Delta}(1236)$ resonances. Note that the $M(\bar{p}\pi^-)$ and $M(n\pi^-)$ [as well as the $M(\bar{p}\pi^-)$ and $M(n\pi^+)$] distributions are nearly similar as required by G - invariance In particular one has (within errors) the same amount of $\bar{\Delta}^{--}$ and Δ^- production rate.

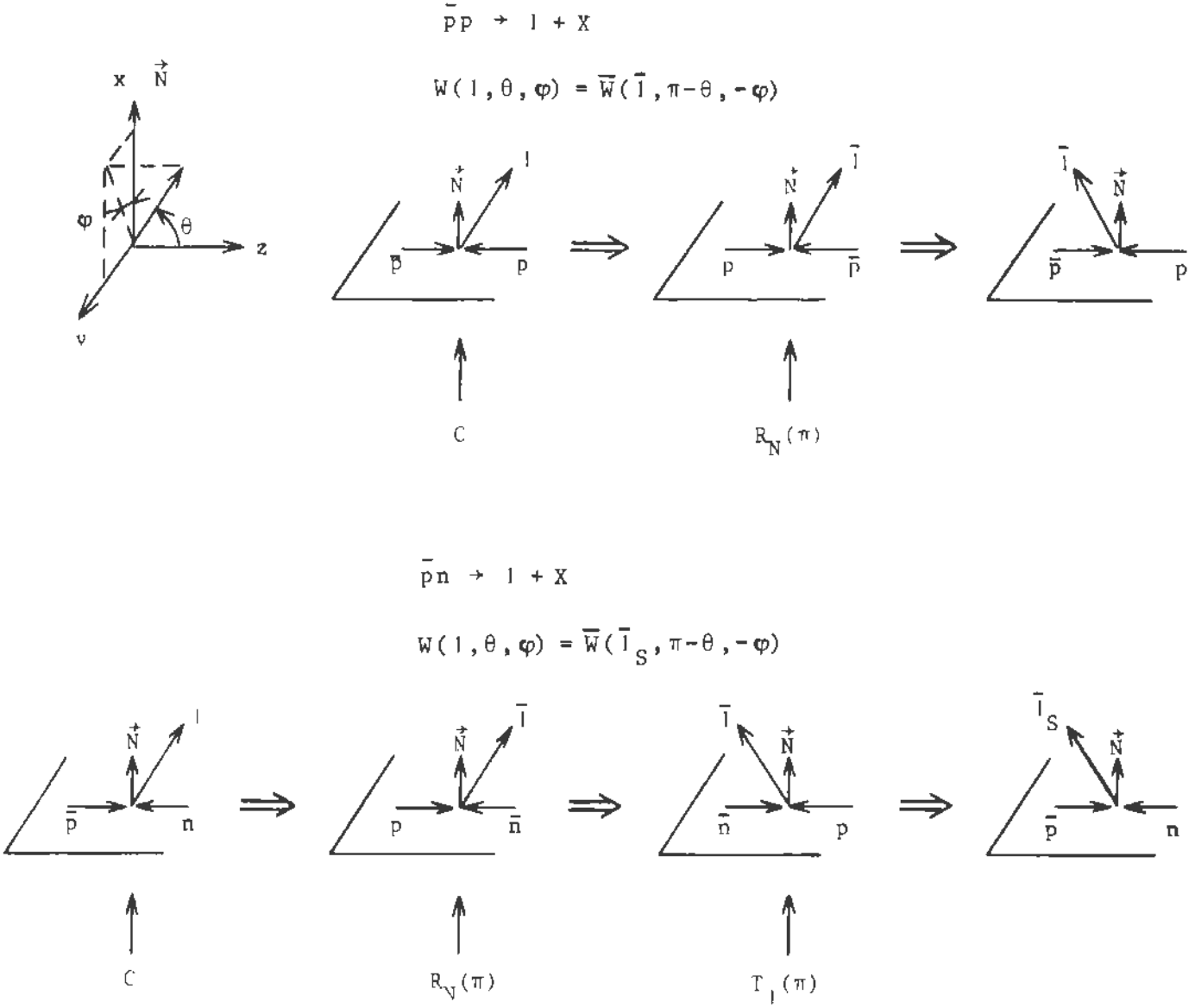

Figure 1.2

Diagrams illustrating the transformation of the initial and final state for unpolarized $\bar{p}p$ [$\bar{p}n$] collisions introduced by applying the $CR_N(\pi)$ [$CR_N(\pi)T_1(\pi)$] operators. Here C is the charge conjugation operator, $R_N(\pi)$ is the π rotation operator around any axis perpendicular to the incoming $\bar{p}$ line of flight in the c.m. system. The $T_1(\pi)$ operator is the π rotation operator around the first axis in isospace, changing essentially a particle in its charge symmetric ones. Note that the definition of the φ emission angle (top left) is sligthly different form that given in reference (1).

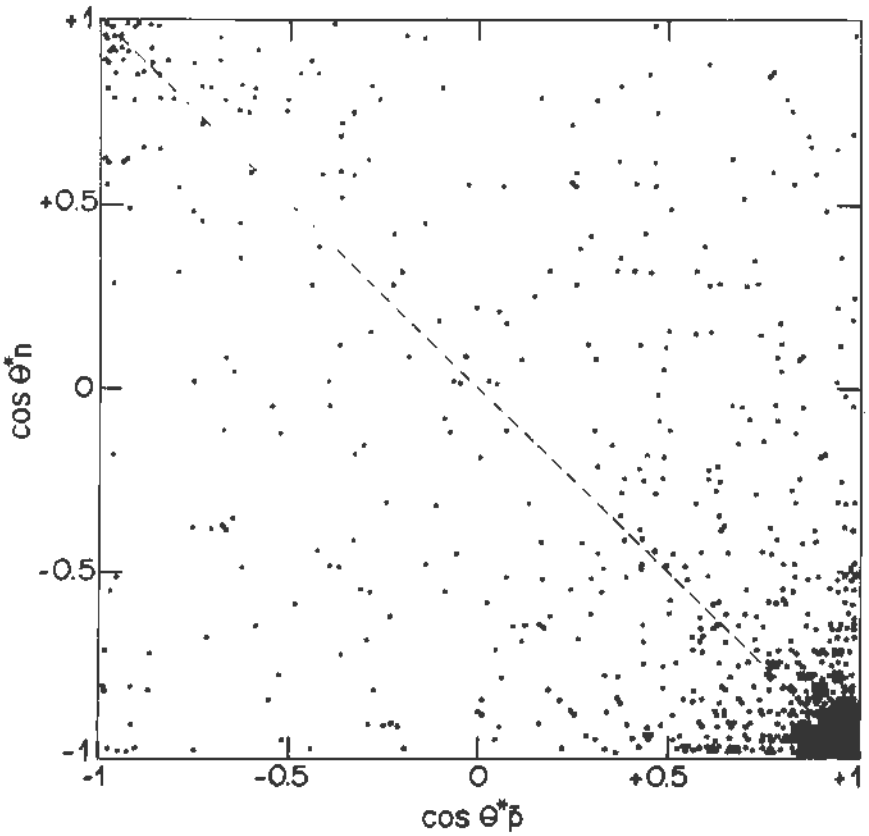

Figure 1.3

The cosine of the n c.m. angle ($\cos\theta^*_n$) versus the cosine of the $\bar{p}$ c.m. production angle ($\cos\theta^*_{\bar{p}}$) for the $\bar{p}n \to \bar{p}n\pi^+\pi^-$ reaction at 5.55 GeV/c. This plot is symmetric with respect to the second diagonal as required from G - invariance (see text)

2. USE OF BOUND NUCLEONS AS TARGETS

2.1 - The spectator model

The utilization of a complex nucleus for studying interactions on neutrons introduces many complications in the data analysis. However, this is sometimes the only possibility to study hadron - neutron reactions and in particular $\bar{p}n$ interactions. The deuteron, which is the most simple nucleus, is very convenient for this purpose. Indeed the deuteron has a small binding energy (B = 2.23 MeV), namely the bound nucleons are almost on their mass shell. An equivalent statement consists in saying that the average distance between the two nucleons is rather important with respect to the dimensions of the nucleons. This can be seen from the asymptotic wave function of the deuteron given by[2]: $\Psi(r) \sim e^{-\alpha r}/r$, r being the magnitude of the two-nucleon relative coordinate. Here $1/\alpha = \hbar/\sqrt{Bm} \sim 4$ fm gives the average distance between the two nucleons each having a mass m. One already foresees that because of the relatively large distance it is likely that a beam particle will interact with one nucleon, the other being a spectator. In a slightly more quantitative form the validity conditions of the spectator scheme can be expressed as:

- the average distance between the two nucleons is larger than the range of the nuclear force estimated with the expression $\mu \approx \hbar/(m_\pi c) = 1.4$ fm (m_π being the pion mass and c the velocity of light),
- the bound nucleons have to be "frozen" during the interaction.

The last statement means that the characteristic time of the deuteron $\tau = 2\pi\hbar/B \approx 2 \times 10^{-21}$ s has to be greater than the interaction time. This latter time can be estimated from the relation $\tau' \approx \mu/(\beta_{inc} c)$, $\beta_{inc} c$ being the velocity of the incident particle. The $\tau' < \tau$ condition is already fulfilled when the beam particle is about 1 GeV/c, since one has $\tau' \approx 0.5 \times 10^{-23}$, 0.6×10^{-23} s for a pion and a nucleon beam, respectively. Thus for high-energy interactions one can assume that if the beam particle interacts with one of the bound nucleons, the second nucleon, the spectator, does not participate in the reaction (apart from the over-all energy - momentum conservation). This is the basis of the impulse approximation model worked out some twenty years ago[3].

The spectator nucleon is described by means of the deuteron wave function. The $\Psi(r) \sim e^{-\alpha r}/r$ is an asymptotic expression which becomes singular for small r. The wave function has then to be slightly modified for small r.

A possible modification is for instance $\Psi(r) \sim e^{-\alpha r}/r[1 - e^{-\mu r}]$ with $\mu \gg \alpha$ in order to conserve the asymptotic behaviour for $\Psi(r)$. This last expression which satisfies the boundary conditions $[\Psi(r \to 0,\infty) \to 0]$ is also written in the form of $\Psi(r) \sim [e^{-\alpha r} - e^{-\beta r}]/r$. This is the well-known Hulthèn wave function[2], the Fourier transform of which gives the wave function in momentum space, i.e.

$$\varphi(p) \sim \frac{1}{(p^2 + \alpha^2)(p^2 + \beta^2)} \quad .$$

Here p is the momentum of the nucleons inside the deuteron and represents then also the momentum of the spectator. Generally one takes the values $\alpha = 46$ MeV/c and $\beta = 260$ MeV/c. There exist, of course, other expressions for the deuteron wave function[4]. Some of them are used in Fig.2.1 in order to calculate the momentum distribution of the nucleons inside the deuteron given by $p^2|\varphi(p)|^2$ [Ref.5]. The angular distribution of the spectators is isotropic in this approximation.

The impulse approximation model is of course an oversimplified picture. Let us only enumerate some of the effects neglected in the simple approach discussed here[6]:

i). The Fermi motion of the neutron target yielding an important spread in the c.m. energy.

ii). The cross-section variation of the studied reaction in the c.m. energy range introduced by the Fermi motion of the target.

iii). The influence of the flux factor due to different beam neutron momentum configurations.

iv). The screening or shadow effects.

v). The off-mass-shell properties of the bound nucleon.

vi). The influence of the exclusion principle.

Apart from points (i) and (iv) we will not discuss here the influence of the various effects just mentioned. Let us only mention that the influence on the spectator angular distribution of flux factor corrections is often counterbalanced by the influence of the cross section variation [point (ii)]. In any case the simple picture discussed here gives a rather good description of the spectator nucleons. This means, in particular, that the spectator protons (p_s) tend to be emitted isotropically in the laboratory frame, whereas their laboratory momentum follow roughly the distributions given by the various deuteron wave functions. Figure 2.2 presents some p_s distributions for exclusive and semi

inclusive reactions. For the semi inclusive reactions (no fitted events) there is an accumulation of events in the forward direction (for the definition see Fig.2.2) resulting from coherent events and from those having a spectator neutron in the final state. For these cases, spectator proton events can be selected by choosing small momentum protons in the nearly isotropic part of the p_s angular distribution or those emitted backward in the laboratory frame.

The momentum of the neutron target before the collision take place (Fermi motion) introduces a large and non-negligible spread in the available c.m. energy. Thus for an incident $\bar{p}$ momentum of 5.5 GeV/c the c.m. energy spread introduced because of the Fermi motion would be obtained with a stationary nucleon target by changing the incident beam momentum by ~ 1 GeV/c. This means that for each incident laboratory momentum one measures phenomena which are averaged over a high c.m. energy range. It is, of course, also possible to select events in smaller c.m. energy intervals, but this leads to subsamples with reduced statistics.

In order to analyse the interactions on neutrons, one is often interested to study quantities evaluated in the c.m. of the collisions[6]. To this end one has to define the energy - momentum four vector associated with the neutron target. Two different methods are used for this purpose. Disregarding off - mass-shell effects one simply assumes that the mass of the neutron target is real. Then the energy of the neutron (E_n) is equal to that of the proton (E_p), while their laboratory ($\vec{p}_N$) momenta are opposite since the deuteron is at rest in the laboratory frame. One has

$$E_n = E_p$$

$$\vec{p}_n = -\vec{p}_p$$

This method has the advantage of treating the two nucleons on the same footing, but does not assure strict energy conservation, as the mass of the deuteron $m_d' = E_n + E_p$ is greater than its real value (Fig.2.3). The second method consists in assuming that the spectator proton is on its mass shell even before the beam - neutron interaction takes places. In contrast the neutron target is considered as a virtual particle (denoted by primed symbols). Then one has strict energy conservation yielding

$$E_{n'} = m_d - E_p$$

$$\vec{p}_{n'} = -\vec{p}_n$$

The mass $m_{n'} = \sqrt{(E_n^2 - \vec{p}_{n'}^2)}$ follows a distribution as shown in Fig.2.3, but has a value smaller than the real neutron mass. Here one has the inconvenience of assuming that only the neutron is not on its mass shell. Of course both methods give results approaching each other when the c.m. available in the collision increases.

2.2 - Cross-sections

There are the curves of Fig.2.1 which are essential for calculating cross-sections in reactions where a spectator proton is present in the final state. Generally in a given experiment not all the spectator protons can be detected as they have small momentum. In many cases an important fraction of them are under the threshold detection of the experimental apparatus. Thus, in a deuterium-filled bubble chamber, spectator protons can only be seen if they have a momentum greater than 80 — 100 MeV/c (about 1/3 of them). To estimate the exact fraction of events having invisible p_s depends on the wave function chosen to describe the deuteron. Although all the used wave functions give similar p_s momentum distribution, the cross-section calculations based on the detected part of the p_s (essentially p_s with momentum greater than 100 MeV/c) depend on the chosen deuteron wave function. This is illustrated in Table 2.1, which gives the ratio between the cross-section calculated with the Hulthèn (σ_H) wave function and other types of functions (σ_i) when only p_s with momentum greater than 100 MeV/c are detected[5]. It is then worth wile to note that it is rather crucial to use the same method for determining cross-sections if one interested in investigating s - channel effects.

Let us now add some remarks about screening effects. For total cross-sections there is a simple procedure for taking into account screening or shadowing effects[6]. Indeed, in the framework of the Glauber model, the elastic $\bar{p}d$ scattering amplitude can be expressed as a sum of the $\bar{p}p$ and $\bar{p}n$ elastic scattering amplitudes and also from a contribution due to double scattering processes. By means of the optical theorem one then obtains the well-known Glauber formula[7] relating the total $\bar{p}d$ cross section $[\sigma_t(\bar{p}d)]$ with the total $\bar{p}N$ $[\sigma_t(\bar{p}N]$ cross-sections, i.e.

$$\sigma_t(\bar{p}d) = \sigma_t(\bar{p}p) + \sigma_t(\bar{p}n) - \delta\sigma$$

TABLE 2.1 - Fraction of spectator having their laboratory momentum smaller than 0.1 GeV/c calculated with various deuteron wave functions (column 2). Column 3 gives the ratio between the cross-section calculated with the Hulthèn wave function (σ_H) and the other types of function (σ_i). The calculations are made by building the entire momentum spectra using p_s momenta greater than 100 MeV/c

Wave function [a]	Percentage	σ_H/σ_i
Hulthèn	80.61	1
Gartenhaus - Moravcsik II	83.22	0.87
Gartenhaus - Moravcsik III	83.06	0.87
McGee	79.50	1.06

(a) Ref. 4

Here $\delta\sigma$ is the cross-section defect which is identified with the double scattering term in the elastic $\bar{p}d \to \bar{p}d$ process. For an elastic reaction such a simple procedure (addition of amplitudes) cannot be used, as the production processus is described by squaring amplitudes. Therefore one utilizes sometimes a correction method based rather on plausibility than on exact arguments[6]. For high-energy reactions, where the elastic scattering amplitudes are mainly imaginaries, one has $\delta\sigma > 0$[7]. One may then consider $\delta\sigma$ as resulting from the shadowing of one nucleon by the other inside the deuteron, each of them giving a $\delta\sigma/2$ contribution. A similar argument can also be made for inelastic reactions (neglecting any interference phenomenon). Then $\sigma_i(n)$, the cross-section of the i-th channel on a neutron target, will be obtained by adding a $\delta\sigma_i/2$ term to the measured $\sigma_i^m(n)$ value. All these $\delta\sigma_i$ obtained from the various channels have to obey the constraint $\delta\sigma = \Sigma_i \delta\sigma_i$. A further hypothesis can now be made assuming that the proportion of screening in each channel is the same as for the total cross-section, namely[6].

$$\frac{\delta\sigma}{\sigma_t(n)} = \frac{\delta\sigma_i}{\sigma_i(n)}$$

[here $\sigma_t(n) \equiv \sigma_t(\bar{p}n)$]

This relation, although without real justification, in any case fulfil the constraint $\delta\sigma = \Sigma\, \delta\sigma_i$. For the cross defect one can take the simplified expression[7]

$$\delta\sigma = A\,\sigma_t(p)\,\sigma_t(n) ,$$

where

$$A = \frac{1}{4}(1 - \alpha_n\,\alpha_p)\,\langle r^{-2}\rangle .$$

Here α_N is the ratio of the real to the imaginary part of the $\bar{p}N$ elastic scattering amplitude at zero four-momentum transfer and $\langle r^{-2}\rangle$ is the average inverse square of the neutron - proton distance in the deuteron. From the expression

$$\sigma_i(n) = \sigma_i^m(n) + \frac{\delta\sigma_i}{2} ,$$

one obtains

$$\sigma_i(n) = \sigma_i^m(n) + \frac{A}{2}\,\sigma_i(n)\,\sigma_t(p) ,$$

hence

$$\sigma_i(n) = \frac{\sigma_i^m(n)}{1 - A\,\sigma_t(p)/2} .$$

This formula, which gives corrections of about 10%, has to be considered with some care because of the crudeness of the above calculation. Nevertheless, it is believed that this kind of estimate gives the order of magnitude for the screening effects in inelastic processes.

2.3 - The break-up reaction

There is one type of reaction in which the spectator scheme cannot be applied easily. This is the so-called break-up reaction $\bar{p}d \to \bar{p}pn$, in which the outgoing nucleon of smaller laboratory momentum cannot be identified with certainty as being the spectator nucleon. The reason for this is that the $\bar{p}N \to \bar{p}N$ scattering is usually dominated by diffraction scattering (the scattered $\bar{p}$ tends to be scattered with small four momentum transfer). The recoiling nucleon has then a laboratory momentum comparable in magnitude to that which the spectator nucleon would have because of its Fermi motion. Apart from this intrinsic difficulty the situation is further complicated by interference phenomena and double scattering.

Therefore the break-up reaction is generally analysed in the framework of the Glauber formalism[9]. Spectator nucleon assignments can, however, be made on the basis of statistical arguments or by selecting specific region in the three-particle phase space. One can, for instance, associate with each outgoing nucleon having a momentum $\vec{p}_N$ a probability

$$W_N = \int_{\vec{p}_N}^{\infty} |\varphi(\vec{p}_n)|^2 d\vec{p}_n \; / \; \int_0^{\infty} |\varphi(\vec{p}_n)|^2 d\vec{p}_n$$

of being a spectator[10]. Here φ is the deuteron wave function in the momentum space. Then a possible way to identify spectator protons is to choose reactions where W_n is small and W_p large. At 5.55 GeV/c incident momentum a $W_n/(W_p + W_n) \leqslant 0.15$ cut[10] leads to the characteristic spectator distributions for the outgoing proton (Fig.2.4). This method is not very efficient as only ~ 10 % of the initial sample was used. Nevertheless, the discussed event selection allowed the study of the differential $\bar{p}n \to \bar{p}n$ cross-section shown in Fig.2.4. Indeed the exponential slope of the four momentum transfer (t) distribution fitted with an e^{bt} function has nearly the same values [$b = (8.4 \pm 0.8)\,GeV/c^{-2}$] that obtained by analysing the $\bar{p}d \to \bar{p}d$ scattering at 5.55 GeV/c using the Glauber formalism[11].

The way discussed above for isolating $\bar{p}n \to \bar{p}n$ events does not permit a direct determination of the total elastic $\bar{p}n$ cross-section [$\sigma_e(\bar{p}n)$]. Nevertheless, an estimate can be obtained by assuming that the ratio of the real to imaginary part of the $\bar{p}n$ scattering amplitude is negligible. Using then the optical theorem one obtains for the elastic $\bar{p}n$ differential cross-section

$$\frac{d\sigma}{dt} = \frac{[\sigma_t(\bar{p}n)]^2}{16\pi} e^{bt}$$

leading to

$$\sigma_e(\bar{p}n) = \frac{[\sigma_t(\bar{p}n)]^2}{16} \frac{1}{b}$$

[In the example discussed here one obtains $\sigma_e(\bar{p}n) = (16.5 \pm 2.4)$mb.]

One can also use a more complex nucleus for studying the $pn \to pn$ scattering or even more complicated interactions on neutrons. Recently, inelastic reactions on a neutron target were studied using an ^{4}He beam at 8.56 GeV/c entering in a hydrogen filled bubble chamber[12]. This corresponds to a p momentum of 2.15 GeV/c in the system where the ^{4}He is at rest. The study of the reaction

$p\,^4He \to p\,n\,^3He$ showed that about 90 % of this reaction occurs with a ^3He spectator (^3He_s), the rest having a spectator neutron (n_s) in the final state. Figure 2.5 presents the angular and momentum distribution of the spectators in the system where the ^4He is at rest. As can be seen from this figure, the n_s and ^3He_s present the characteristic spectator distributions, namely the ^3He_s and n_s tend to be emitted isotropically and with small momentum. This time there is no difficulty in identifying the spectator[12].

Using the events with ^3He_s at 8.56 GeV/c one obtains the elastic $pn \to pn$ differential cross-section shown in Fig.2.6. The fact the distribution tends to zero when $|t| \to 0$, t being the four-momentum transfer between the incident and outgoing p, is due to the binding energy of the ^4He (one always needs some non-zero value for t in order to break the ^4He). Apart from the $|t| = 0$, the distribution shown in Fig.2.6 is intended to represent the $pn \to pn$ elastic scattering. One notices the presence of the diffraction peak as well as the large exchange $pn \to np$ contribution.

As stated before, in collisions on deuterons, the fact that two outgoing nucleons have comparable momenta leads to difficulties in identifying the spectator. In addition, this may yield to suppression of some kinematical configuration as a consequence of the generalized Pauli principle. Such a situation does not occur with the ^4He whenever it dissociates into n and ^3He. The use of ^4He to study interactions on neutrons also has some inconveniences. The neutron target is more virtual than in the deuteron case as its binding energy inside the ^4He is B = 20.6 MeV. If one assumes that the outgoing ^3He is on its mass shell when the interaction occurs, the quoted experiment gives for the virtual neutron target a mass distribution with an average of ~ 0.89 GeV/c^2 and a dispersion of ~ 30 MeV/c^2. One sees that the mass of the virtual neutron is not too far from the real value, although the deviation is greater than for the deuteron case.

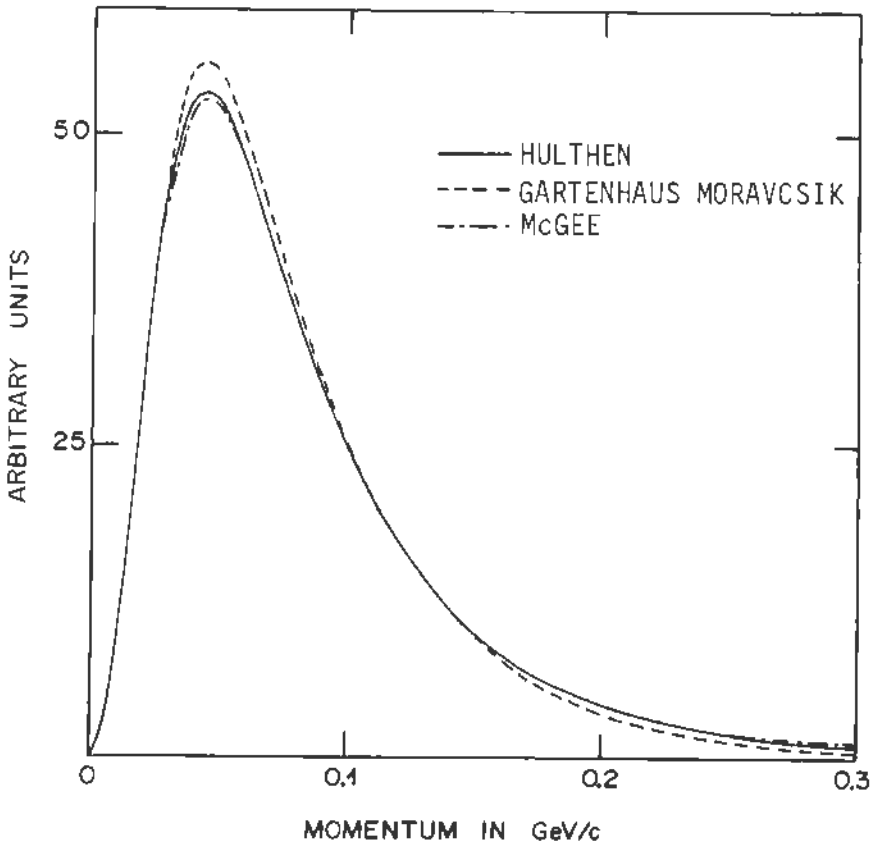

Figure 2.1

Distributions of momenta of the nucleons inside the deuteron obtained from various deuteron wave functions. On the present scale no difference appears between the solutions II or III of the Gartenhaus - Moravcsik wave function [see Table 2.1 and reference (4)]

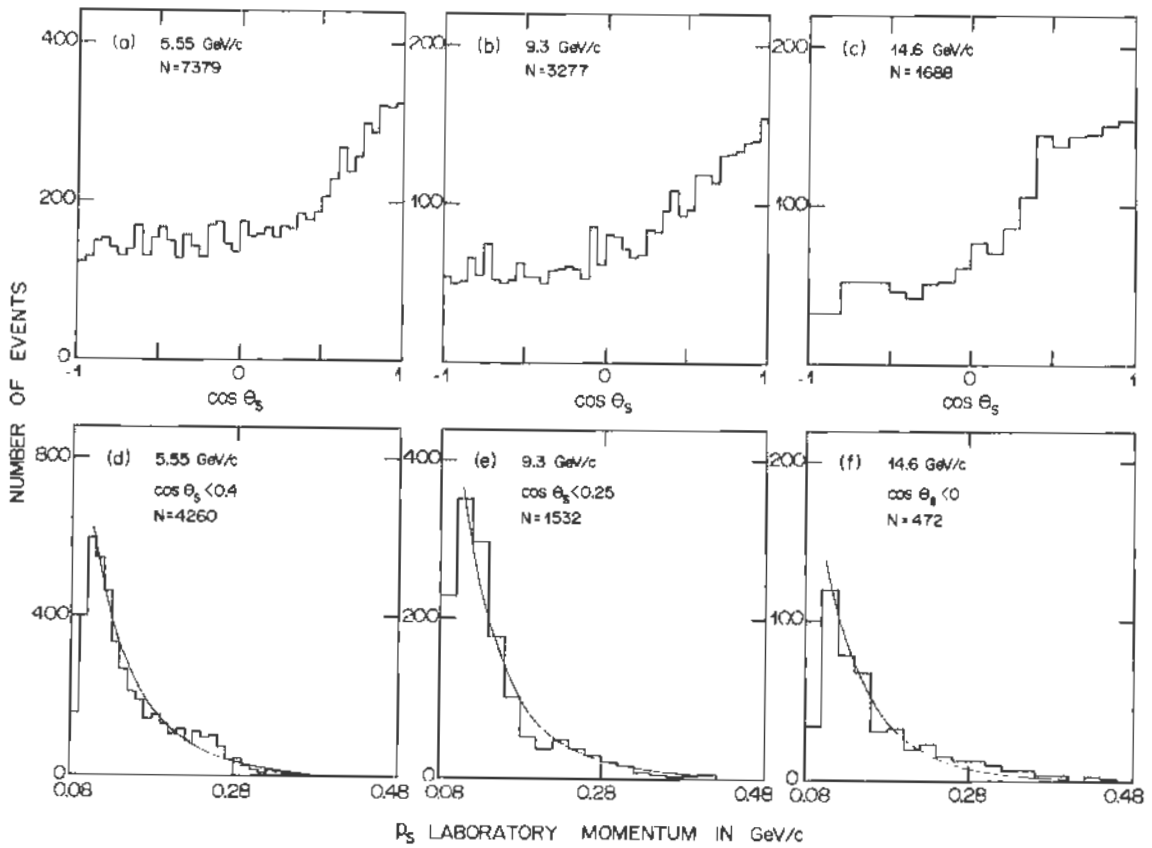

Figure 2.2a

The laboratory $\cos\theta_s$ distributions for the four pronged (no fitted) events in $\bar{p}d$ interactions at (a) 5.55, (b) 9.3 and (c) 14.6 GeV/c incident momentum, θ_s being the emission angle of the stopping track defined with respect to the incoming beam direction. The forward accumulation is due to coherent events and also to events with a spectator neutron ; (d), (e) and (f) show the laboratory momentum distribution of the stopping track for ranges in which the $\cos\theta_s$ distributions are nearly isotropic. The full lines represent the Hulthèn wave function predictions [Taken from reference (5)].

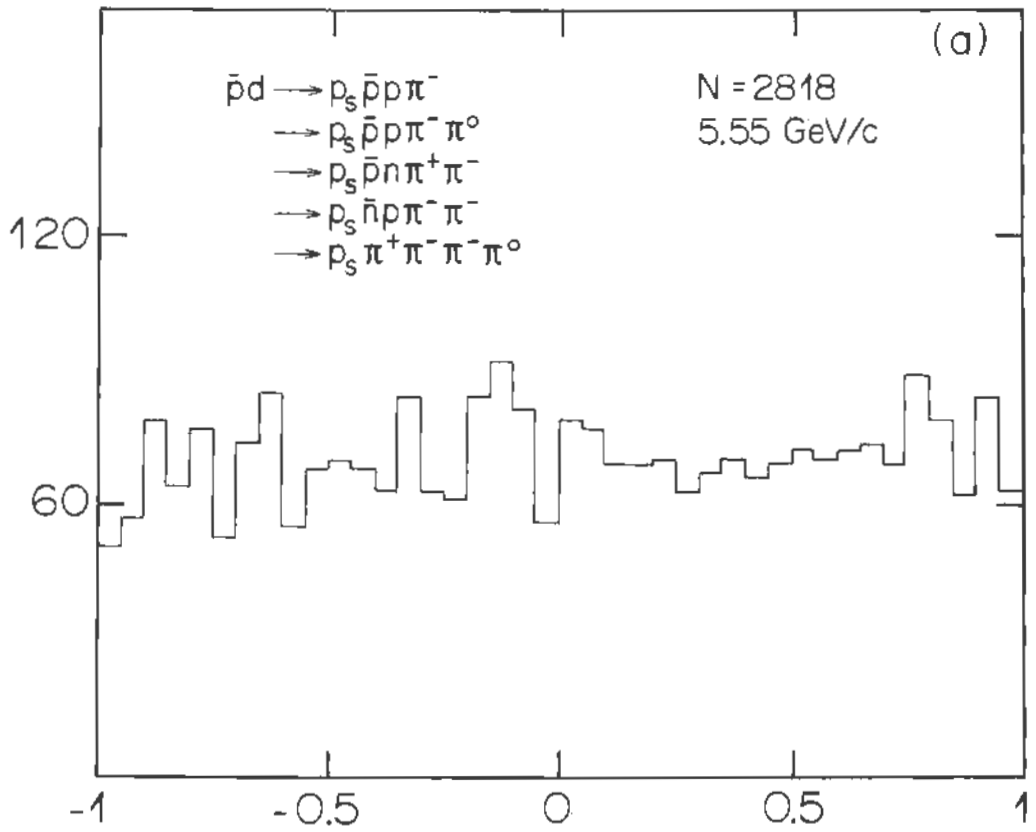

Figure 2.2b

The laboratory $\cos\theta_s$ distribution for production channels obtained at 5.55 GeV/c incident momentum [Taken from Phys. Rev., D12, 3412 (1975)].

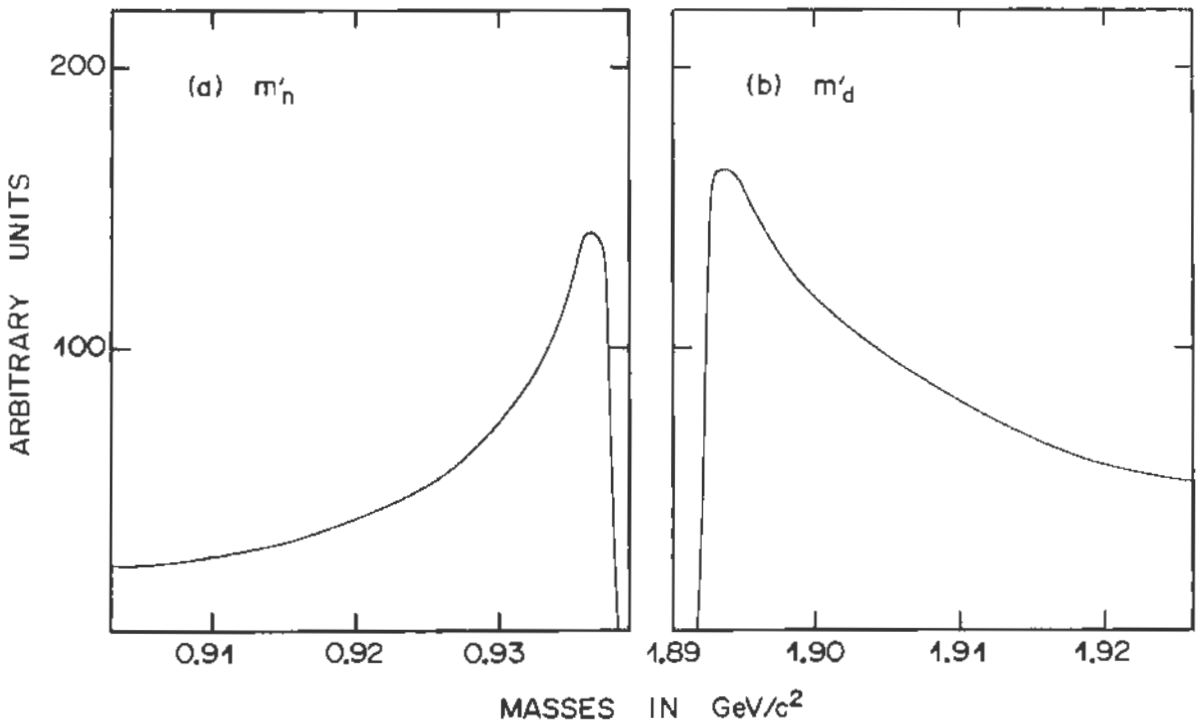

Figure 2.3

a). Distribution of the mass of the virtual neutron target assuming that the spectator proton is on its mass shell before the interactions takes place.

b). Distribution of the deuteron mass if one assumes that both nucleons i.e. the spectator nucleon and the target nucleon are real nucleons. The curves are calculater using the Hulthèn wave function [Ref.6].

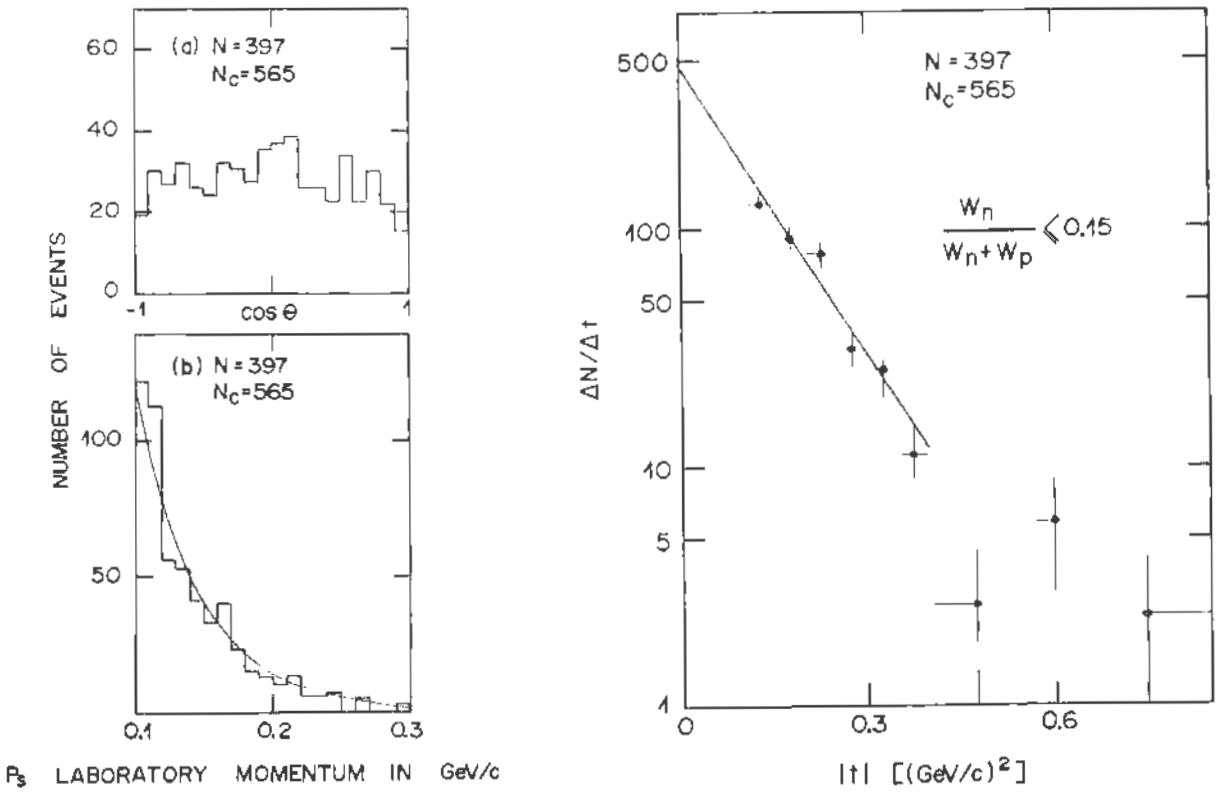

Figure 2.4

Angular and momentum distributions of the p_s for the $\bar{p}d \to p_s \bar{p}n$ reaction (left hand side) at 5.55 GeV/c selected according to the $W_n/(W_n + W_p) \leq 0.15$ condition [Ref.10]. The full curve (b) is the Hulthèn wave function prediction. Distribution of the four momentum transfer between the incident and outgoing $\bar{p}$ for the $\bar{p}n \to \bar{p}n$ events (right hand side). The curve represents on exponential fit to the data in the $0.1 \leq |t| < 0.4 (GeV/c)^2$ range [Ref. 10].

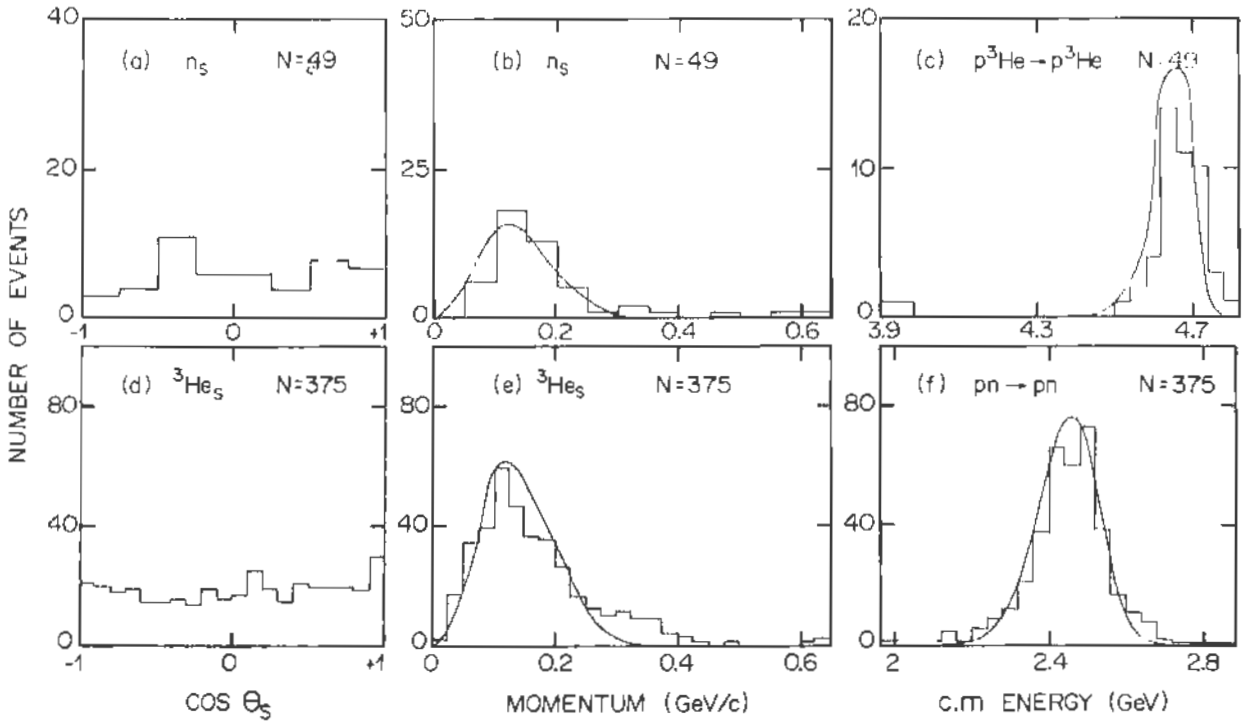

Figure 2.5

The angular [(a) and (d)] and momentum [(b) and (e)] distributions of the n_s and ^3He_s spectators in the system where the ^4He target is at rest. In (c) and (f) are represented the c.m. energy distributions due to the Fermi motion for the $p^3He \rightarrow p^3He$ and $pn \rightarrow pn$ virtual scattering The full lines are obtained using the ^4He wave function as described in reference 12.

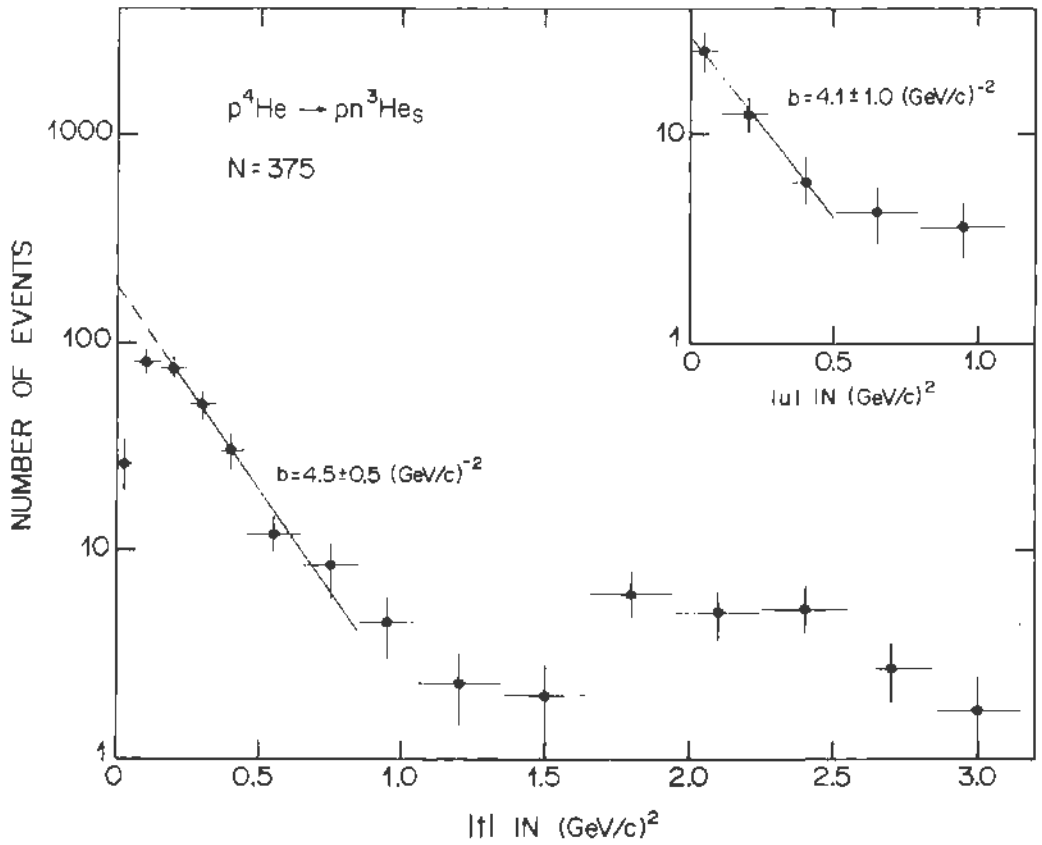

Figure 2.6

The $|t|$ and $|u|$ distributions for the virtual $pn \rightarrow pn$ scattering [Ref.12]. Here t and u are the four momentum transfer between the initial p and the final p or n, respectively. The full lines were obtained by fitting the data with e^{bt} or e^{bu} functions.

3. RESONANCES

3.1 - Introduction

The resonance hunting is certainly one of the most interesting aspects connected with the study of inelastic reactions. Generally speaking there are two different methods to search for resonances, namely in formation or production experiments. In formation experiments (see Section 3.2) the c.m. energy $\sqrt{S}$ [$\sqrt{S} \equiv M$], of the collisions is varied and bumps having Breit-Wigner shapes are searched for in total, elastic, or inelastic cross-sections. This is a situation analogous to nuclear physics whenever one tries to discover levels of the compound nucleus. For production experiments (Section 3.3) the situation is perhaps more complex as one searches for resonances among subsets of produced particles. In some respects production experiments offer more exploration possibilities. Indeed, in one experiment, a wide mass region, obtained from the various effective mass distributions of the secondaries, can be studied. Furthermore, when resonances are highly inelastic, i.e. are coupled to many particle final states, production experiments may also be of advantage.

Since we are interested in $\bar{p}N$ interactions we will also consider the reactions obtained by means of $\bar{N}N$ off-mass-shell interactions. These processes are obtained in reactiona in which the quantum numbers exchanged in the t channel are compatible with those of an $\bar{N}$. The following diagram gives some examples of such $\bar{N}N$ collisions. Resonances produced in these virtual collisions belong in fact to usual production experiments. Nevertheless, we consider this class of reactions separately (Section 3.4), primarily because of the interpretation given to these processes.

Examples of reactions allowing the study of virtual $\bar{p}p$ processes

3.2 - Formation experiments

Apart from e^+e^- interactions, $\bar{p}p$ collisions represent the only way to form mesons. These experiments benefit from a very good mass resolution (i.e. the resolution of the c.m. energy) as it depends essentially on the precision with which the beam momentum is known. Errors of ~ 10 MeV/c^2 can easily be obtained for mass ranges of 1.9...2.5 GeV/c^2 [13].

A rich meson spectrum can be reached as the initial $\bar{N}N$ system can be, in principle, in a great variety of spin (J) and parity (P) states. The parity of two initial fermions entering into collisions with an orbital momentum L is given by $P = (-1)^{L+1}$, while the charge conjugation operator is $C = (-1)^{L+S}$, S = 0,1 being the total spin of the two nucleons. Remember that only neutral states such as those formed by $\bar{p}p$ systems are eigenvectors of the charge conjugation operator with precisely the eigenvalues $C = (-1)^{L+S}$. Labelling the $\bar{p}p$ initial system by J^{PC} one obtains the various states accessible in $\bar{p}p$ collisions as indicated in the Table 3.1.

TABLE 3.1 - The various J^{PC} states which may by obtained in $\bar{p}p$ collisions

$\bar{p}p$		J^{PC}				
S = 0	L = J	0^{-+}	1^{+-}	2^{-+}	3^{++}	....
S = 1	L = J		1^{++}	2^{--}	3^{++}	....
	L = J±1	0^{++}	1^{--}	2^{++}	3^{--}	....

Similarly to the reasoning made with the quark - antiquark ($q\bar{q}$) systems assumed to build the meson spectrum, no exotic states from the second kind can occur in $\bar{p}p$ collisions. In other words this means that the serial $J^{PC} = 0^{+-}$, 1^{-+}, 2^{+-},... having natural parity and unatural charge conjugation parity cannot exist. Indeed for natural parity states, i.e. $P = (-1)^J$, one has $(-1)^J = (-1)^{L+1}$, hence J = L+1. The conservation of total spin implies then that S = 1, giving always to the charge conjugation operator $C = (-1)^{L+S}$ the same parity as for P.

Although the initial $\bar{p}p$ system may have the quantum numbers indicated in the above table, not all these J^{PC} values can be excited because of the inihibition due to the centrifugal barrier. Indeed from a semi-classical impact-parameter approach one can estimate the maximum J value to be $J_{max} = kR+1$ [13,14]. Here k is the incident c.m. momentum and R is the interaction radius usually taken as ≈ 1 fm. Figure 3.1 presents in a J versus M^2 plot some well-established meson (M is the mass of the meson) together with the $\bar{p}p$ impact parameter limit $J_{max} = kR+1$ for different values of the interaction radius (R = 1, 1.3 and 1.6 fm). Although there is an uncertainly about the value of R, Fig.3.1 shows clearly that only high mass and high spin systems can be excited in $\bar{N}N$ collisions. Generally these objects are expected to have large widths. In this respect the high precision in $M(\sqrt{S} \equiv M)$ attainable in formation experiment may not be really crucial.

A resonance in the s-channel appears in the elastic (σ_e), inelastic (σ_{in}), or total (σ_t) cross-section, studied as a function of $\sqrt{S} \equiv M$ as bumps sited on a background. These bumps are expected to present a Breit-Wigner shape, although this is strictly true when the mass resolution for M is much smaller than the resonance width and if interference phenomena are neglected. Within these approximations the bumps can be parametrized by

$$\sigma_e = F(I) \frac{4\pi}{k^2}(J + 1/2) \frac{x^2}{\varepsilon^2 + 1}$$

$$\sigma_{in} = F(I) \frac{4\pi}{k^2}(J + 1/2) \frac{x(x - 1)}{\varepsilon^2 + 1}$$

$$\sigma_t = F(I) \frac{4\pi}{k^2}(J + 1/2) \frac{x}{\varepsilon^2 + 1}$$

Here k is the incident c.m. momentum, x is the elasticity of the resonance defined by :

$$x = \frac{\Gamma_{\bar{N}N}}{\Gamma_t}$$

and

$$\varepsilon = [M_R - M] \frac{2}{\Gamma_t} .$$

The resonance mass is denoted by M_R, while $\Gamma_{\bar{N}N}$ and Γ_t are the elastic and total widths, respectively. The factor F(I) in the above expression is due to isospin ($F = \frac{1}{2}$, 1 for $\bar{p}p$ and $\bar{p}n$ interactions, respectively). From a first glance it seems

that the study of σ_t as a function of M is the most favourable case to search for resonance with small elasticity (remember that $x \leq 1$). This is, however, not really true as in σ_t distributions, bumps - if any - are usually sited on a large background. In fact, all the cross-sections σ_e, σ_{in}, σ_t, as well as those obtained from specific inelastic channels, are studied in order to discover resonances.

Let us first consider the total $\bar{p}N$ cross-section, which can be separated into its isospin I = 0 [σ_0] and I = 1 [σ_1] components, namely

$$\sigma_t(\bar{p}p) = \frac{1}{2}\sigma_0 + \frac{1}{2}\sigma_1$$

$$\sigma_t(\bar{p}n) = \sigma_1$$

The determination of σ_1 (and hence σ_0) is not simple, because one has to extract $\sigma_t(\bar{p}n)$ from measurements of total $\bar{p}d$ cross section [$\sigma_t(\bar{p}d)$]. To this end one uses the Glauber formula slightly modified[15] :

$$\sigma_t(\bar{p}d) = "\sigma_t(\bar{p}p)" + "\sigma_t(\bar{p}n)" - "\delta\sigma",$$

where $\delta\sigma$ is the cross-section defect still given by :

$$\delta\sigma = \frac{1}{4}(1 - \alpha_n\alpha_p)\langle r^{-2}\rangle\sigma_t(\bar{p}p)\sigma_t(\bar{p}n) .$$

The notation "σ_t" and "$\delta\sigma$" indicates that these quantities are smeared by the Fermi motion of the nucleons inside the deuteron. The extraction of $\sigma_t(\bar{p}n)$ from the above relation is a complicated procedure[15] and is somewhat model-dependent. Indeed one has to choose an expression for the deuteron wave function and also a value for $\langle r^{-2}\rangle$. Furthermore, to calculate "$\sigma_t(\bar{p}p)$" one has to know $\sigma_t(pp)$ in the c.m. energy range covered by $\bar{p}p$ processes where the target p would be subject to Fermi motion. The expression for "$\delta\sigma$" is even more complicated, because one has to smear by the Fermi motion double scattering terms. As the cross-section defect is small one simplifies the problem by replacing in $\delta\sigma$ the $\sigma_t(p\bar{N})$ by their smeared "$\sigma_t(\bar{p}N)$" values.

Figure 3.2 presents the behaviour of $\sigma_t(\bar{p}p)$ and $\sigma_t(\bar{p}d)$ as a function of the incident momentum (P_{inc})[15,16] in the so-called S, T, and U regions ($1.9 \leq M \leq 2.5$ GeV/c^2). A low mass bump is clearly visible in Fig.3.2 (left hand side) from which fits lead to a central value $M = 1.932 \pm 2$ MeV/c^2 and a width of

$\Gamma = 9^{+4}_{-3}$ MeV/c^2 [the S bump]. The decomposition of σ_t into its various isospin components is here further complicated as the data are not very far from threshold. Nevertheless a detailed analysis[16] leads to the result that I = 1 is favoured against I = 0. The isospin decomposition has been carried out at higher incident momenta (Fig.3.2, right hand side) and one clearly sees a bump in the σ_0 distribution and two enhancements in the σ_1 one. Table 3.2 summarizes the situation on these bumps, namely the S and T bumps and the two components (I = 0,1) of the U enhancement[17].

TABLE 3.2 - Actual parameters of the bumps in the S, T, and U regions

		S	T	U
Mass	(MeV)	1936 ± 1	2190 ± 10	2350 ± 15
Width	(MeV)	8 - 4	90 ± 20	160 ± 20
σ_t	(mb)	10.6 ± 2.4	2 to 4	~ 2
Isospin		1 (0)	1	0 and 1
σ_{el}	(mb)	7.0 ± 1.4	≥ 2.12	≥ 2.18
σ_{cex}	(mb)	<0.3 ± 0.3	<0.2	< 0.2

Moreover the discussed effects are also seen in the elastic and inelastic cross-sections as illustrated in Figs.3.3 and 3.4 (Refs. 14, 18 and 19). What is more surprising is that no clear S, T, and U signals are seen in the charge exchange $\bar{p}p \to \bar{n}n$ cross-section (σ_{cex}). This can be seen from Fig.3.3, which also presents $\sigma_{cex} \times P_{inc}$ as a function of P_{inc}, the incident laboratory momentum. The cross-section was multiplied by P_{inc} in order to remove the $1/P_{inc}$ dependence of the charge-exchange cross-section. Since the isospin decomposition [T_I] of the elastic [T_{el}] and charge-exchange [T_{cex}] amplitude are given by

$$T_{el} = \frac{1}{2}[T_0 + T_1]$$

$$T_{cex} = \frac{1}{2}[T_0 - T_1],$$

the different behaviour for the $\bar{p}p \to \bar{p}p$ and $\bar{p}p \to \bar{n}n$ channels suggests the presence of strong interference effects. One can thus already foresee that it will be difficult to determine the spin and the elasticity of the observed enhancements[17]. It is rather strange that such interferences occur for all of the S, T and U bumps. Therefore this kind of explanation may appear to be somewhat unsatisfactory. Tentatives to explain the observed bumps as resulting from threshold effects as for instance to the reactions $\bar{p}p \to \bar{p}p\pi^-$, $\bar{\Delta}p$, ρf, $\rho\rho$, etc, have failed[17]. In any case, further investigations must certainly be carried out in order to have a better understanding of the S, T, and U enhancements.

One type of inelastic reaction is particularly interesting, namely the production of two mesons in $\bar{p}p$ collisions. In some of these cases one can immediately obtain some information about quantum numbers of these two meson systems. The first remark that can be made is that the two colliding $\bar{p}$ and p have to be in a triplet state (S = 1). Indeed the parity of the initial state is $P = (-1)^{L'+1}$, while for the two-meson state one has $P = (-1)^{L}$. Here L and L' are the relative orbital momentum of the initial and final states, respectively. Because of parity conservation one has $L' + 1 = L$, hence total spin conservation requires S = 1. Table 3.3 indicates some conclusions which can be drawn about the two meson quantum numbers, using essentially the G-parity constraint. The eigenvalues of G are given here by $G = (-1)^{L+I}\eta_1\eta_2$, the $\eta_{1,2}$ being the intrinsic charge conjugation parities of the outgoing mesons.

TABLE 3.3 - The two meson quantum numbers obtained in $\bar{p}p$ collisions using the G-parity constraint.

$\bar{p}p \to$	$\pi^+\pi^-$	$\pi^o\pi^o$	$\pi^o\eta^o$	K^+K^-
$G = (-1)^{L+I}\eta_1\eta_2$	1	1	-1	no constraint
spin (J) and isospin (I)	J_{even}, I = 0 J_{odd}, I = 1	J_{even}, I = 0	J_{even}, I = 1	

Thus the two-mesons final state appears to be a rather interesting process for determining quantum numbers of resonances. Unfortunately, the cross-sections involved in these reactions are very small, of the order 1% of the annihilation cross-section. Despite these low cross-sections the two meson annihilation reactions have been studied extensively during recent years[18,20]. In fact, experiments have also been carried out using polarized targets in order to facilitate phase-shift analyses[21]. It has been found that in the range $1 \leq M \leq 2.5\ GeV/c^2$ resonances as given in the Table 3.4 are required to fit the $\bar{p}p \to \pi^+\pi^-$ data. These values suggest tentatively assigning these resonances as being due to the T and U bumps[14,21].

TABLE 3.4 - Parameters of the resonances needed to fit the actual $\bar{p}p \to \pi^+\pi^-$ data in the T and U regions

J	I	Mass (MeV/c^2)	Width (MeV/c^2)
3	1	2150	200
4	0	2310	210
5	1	2480	280

The S bump is a good candidate for a baryonium state, i.e. a state formed by four quarks. Such systems are expected from considerations based on duality arguments. Figure 3.5 presents the dual diagrams contributing to pp and $\bar{p}p$ elastic scattering. While in pp scattering there exists only one graph corresponding to Pomeron exchange in the t-channel, three dual diagrams exist for $\bar{p}p$ scattering. Looking in the t-channel these graphs correspond to Pomeron, mesons, and four quarks ($qq\bar{q}\bar{q}$) exchanges. If $qq\bar{q}\bar{q}$ systems really exist, they cannot decay into mesons assuming that only planar graphs are contributing to the decay process (no crossing or disconnected quark lines). Thus the $qq\bar{q}\bar{q}$ object, the baryonium is mainly coupled to systems containing a $B\bar{B}$ in the final state (see Fig.3.5). One expects therefore that baryonium should have a high elasticity and should be suppressed in $\bar{p}p \to n\pi$ decays. This is what happens with the S enhancement. It appears in the elastic $\bar{p}p \to \bar{p}p$ scattering with a cross-section of about 7 mb, while

the signal is suppressed for inelastic reactions (see Fig.3.4). There exists also other approaches based on a quark gluon model yielding two types of baryonium the T and M states (Chang Hong-Mo and Hogaasen). In any case, the fact that exotic states which are not built by the usual $\bar{q}q$ or qqq structures may exist is of course an important question. Further experiments will show if a new field in spectroscopy will open up.

3.3 - Production experiments

Production experiments are in fact the most usual experiments allowing the search for resonances and the study of their decay properties. Much effort has been devoted to these problem. We will here simply discuss the difficulties existing in the discovery of resonances by means of some simple examples. As already stated above, production experiments offer important exploration possibilities by investigating the various effective mass distributions obtained from the secondaries. In principle, resonances manifest themselves as enhancements observed in some effective mass distributions. Of course, not all the observed enhancements are due to resonances. Much care is needed to identify resonances with the various bumps observed in histograms of effective mass. As is well known, reflections, kinematical and threshold effects may produce bumps. The fact that these types of enhancement do not follow a Breit - Wigner behaviour is not a crucial test for identifying them. This is because one may also have difficulties in describing real resonances by using Breit - Wigner functions. Indeed for real resonances the observed enhancements are generally sited on a background. Then in order to determine the mass parameters (central value and width) of the resonance one fits the mass spectrum by using an incoherent mixture of a Breit - Wigner function and a background taken often as phase space. The fact that one does not obtain always a good description of the data is generally accounted for by the crude way (no interference) used for combining background and resonance. Furthermore, the experimental errors on the determination of the effective mass also influence the behaviour of the mass spectra.

For final states, where sets of identical particles are produced, the search for resonances is further complicated by the introduction of combinational background. As an example, let us consider the $\bar{p}p \to 3\pi^+ 3\pi^- \pi^o$ reaction at 5.7 GeV/c[22]. It is clear that resonances in the $\pi^+\pi^-$ system will be hard to detect, because such resonances will be situated on a large background owing to at least the nine different $\pi^+\pi^-$ mass combinations. Although the combinational background

is an incoherent one, one can conceive that small resonance production rates or resonances with large width will not be easy to detect. In order to illustrate these difficulties we present in Fig.3.6 the $\pi^+\pi^-$ effective mass distribution obtained from the $\bar{p}p \to 3\pi^+3\pi^-\pi^o$ reaction. Despite the important background one notices that ρ^o and f^o are present in the final state. The situation becomes more complicated if, using the same data, one is interested to know if there exist also resonances decaying into $\rho\rho$. Figure 3.7 presents the $2\pi^+2\pi^-$ effective mass combination in which two distinct $\pi^+\pi^-$ mass combinations are in the ρ mass band[22]. The enhancement observed in this figure at ~1.7 GeV/c^2 is seen better if one selects $\pi^+\pi^-$ effective mass combinations in a smaller ρ mass band. The question that one has to answer now is: is this enhancement a real resonance and if so, can one determine some of its parameters ? First of all, it can be shown that the real width of the observed enhancement cannot be estimated from these data[22]. This is because the width of the 1.7 GeV/c^2 signal reflects in the mentioned example essentially the mass cuts defining the ρ band. The resonance interpretation is however favoured because no signal is observed in the $\rho\rho'$[22] and $\rho'\rho'$ (Fig.3.7) effective mass distribution. Here ρ' is defined as a $\pi^+\pi^-$ mass band in the region around the ρ mass, as indicated in Fig.3.7. One sees thus that additional tests are of great help in order to identify with some confidence an enhancement with a real resonance.

Let us now discuss some other problems for which $\bar{p}N$ annihilation channels are particularly suitable. Much work has been done in order to understand the A_1 bump. Mechanisms as the Deck effect[23] were proposed to explain this bump (or at least a part of it) appearing in hadron - hadron production processes. The $\bar{p}N$ annihilation channels are particularly suitable for studying the A_1 as no Deck mechanism is present there. Figure 3.8 presents the $\rho^o\pi^+$ effective mass distribution obtained in the $\bar{p}n \to 2\pi^+3\pi^-\pi^o$ channel at 5.55 GeV/c[24]. By fitting these data with incoherent mixtures of phase space and Breit-Wigner functions one clearly see the presence of the A_1 and A_2 bumps. Although the fit is not too good the discussed result support the idea that the A_1 is a real resonance.

Finally let us say some words on narrow resonances which are under intense investigation. Here also we would like to illustrate the difficulties rather than to make a review of narrow signals which are candidates for resonances. Let us for instance consider the 5.1 standard deviation effect has which been seen in the X mass (2.85 GeV/c^2), obtained from the reaction $\bar{p}n \to \pi^-X$ at

5.55 GeV/c[25] (Fig.3.9). Here X means a system made by $\bar{p}p$, $\bar{p}p\pi^o$, $\bar{p}n\pi^+$, or $\bar{n}p\pi^-$. The enhancement is seen better if events in which $\Delta(1236)$, $\bar{\Delta}(1236)$, or $\bar{\Delta}(1900)$ appear in the final state are removed, as explained in Fig.3.9. In the same conditions Fig.3.10 displays the X mass for the three-body $X \to \bar{N}N\pi$. If the 2.85 GeV/c^2 signal is a resonance decaying strongly, the branching ratio $\alpha = (X \to \bar{p}n\pi^+)/(X \to \bar{n}p\pi^-)$ should be one. Although the errors are important, it is shown in Fig.3.10 that α tends to unity whenever the X mass reach 2.85 GeV/c^2. In Fig.3.11 results on angular distributions are presented in the form of backward to forward ratio as a function of the X mass. One sees that at least in Fig.3.11a there is a structure at 2.85 GeV/c^2. All these facts favour a resonance interpretation of the observed enhancement which is found to have a central value of $M = 2.850 \pm 0.005$ GeV/c and a width of $\Gamma \leq 0.039$ GeV/c^2. Let us note that one also observes in the X mass distribution a spike at 3.05 GeV/c with a statistical significance of ~ 3.1 standard deviations. In experimental physics, however, such a significance is not considered as very strong evidence.

We also would like to point out that by using big bubble chambers (with BEBC for instance) it become possible to search for narrow resonances produced at high energies and decaying into many particles. Thus in a recent work[26] a 5.55 standard deviation effect has been observed in the $K^o\pi^\pm\pi^+\pi^-$ system at a mass of 2.60 ± 0.01 GeV/c^2 with a width of $\Gamma \leq 0.018$ GeV/c^2. To conclude this subject one can say that search for narrow resonances is a field to which intense effort is devoted. It is, of course, evident that these jobs are difficult as one needs experimental devices allowing a measurement of effective mass with very good accuracies.

3.4 - Off-mass-shell $\bar{N}N$ interactions

Work has been carried out in studying $\bar{N}N$ interactions by means of virtual processes. The most obvious example is the study of $\bar{p}n$ collisions by means of $\bar{p}d$ interactions. Other kinds of processes have also been considered, such as those in which the system exchanged in the t - channel has the quantum numbers of an $\bar{N}$. Thus the reactions $K^-p \to \Lambda X$ has been studied at 4.2 GeV/c in the optics of studying virtual "$\bar{p}$"p and "K^+"K reactions[27]. Here the symbols "$\bar{p}$" and "K^+" mean that we are dealing with virtual particles. By selecting events with small $|u| = |(\bar{p}_K - \bar{p}_\Lambda)^2|$ or small $|t| = |(\bar{p}_\Lambda - \bar{p}_p)^2|$ one will obtain production processes primarily described by the following graphs.

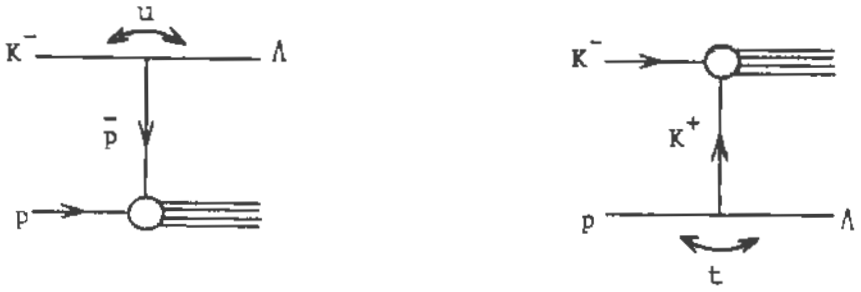

Here $\bar{p}_j$ is the energy - momentum four vector associated with particle j. As the quantum numbers exchanged in the t - channel are those of an $\bar{p}$ or a K one may hope to study $\bar{p}p \to X$ and $K^+K^- \to X$ interactions. In order to obtain samples in which graph (a) [graph (b)] should predominate, events with $|u| \leq 1 (GeV/c)^2$ [$|t| \leq 1 (GeV/c)^2$] were selected[27]. At 4.2 GeV/c this choice has the advantage that there is no overlap between the two regions as shown by Fig.3.12. By using the relation

$$s + t + u = m_K^2 + m_\Lambda^2 + m_p^2 + M_X^2$$

(m_j being the mass of particle j and M_X the mass of the X system), one sees that constant M_X corresponds to lines defined by t + u = constant in the t, u scatter plot (Fig.3.12). Because of the small c.m. energy ($\sqrt{s}$) involved, the maximum value $M_X \sim \sqrt{1.9}$ GeV/c^2 is always under the $\bar{N}N$ threshold. Note that the situation is different for the virtual "K^+"K^- collision. For both cases, Fig.3.13 presents the M_X distributions in which resonance production is clearly visible. The average charged multiplicity [<n>] associated with the X system for "$\bar{p}$"p interactions is shown in Fig.3.14. One sees that these <n> values are not too far from a rough extrapolation of real $\bar{p}p$ data, excluding the $\bar{p}p$ data point at rest. This indicates that one can have some confidence in the method of using virtual collisions for studying $\bar{N}N$ interactions. Indeed one knows that for real collisions <n> depends primarily on the c.m. energy (here M_X) of the collisions (see Section 6). It is then not surprising that the "$\bar{p}$"p collisions lie on a curve extrapolating the real $\bar{p}p$ data.

The off-mass shell $\bar{N}N$ interaction approach is perhaps more interesting when M_X is above the $\bar{N}N$ threshold. Such a study has been made with the CERN Ω device using the reactions $\pi^- p \to p_f \bar{p} p \pi^-$ at 9 and 12 GeV/c incident momentum[28]. Here p_f denotes a fast outgoing proton having a laboratory momentum greater than half of the incident momentum and which is emitted forward in the laboratory system (i.e. within an angle smaller than 150 mrad, defined with respect to the momentum of the incident particle). This trigger condition allows one to have events in which baryon exchange is predominent. Enhancements in the $\bar{p}p$ mass are seen at both momenta (Fig.3.15). As far as concerns these enhancements the situation is similar to any other $\pi^- p$ production experiment. However as stated above, the special configuration of the events may allow one to interpret the observed bumps as resulting from the virtual "$\bar{p}$"$p \to \bar{p}p$ scattering.

Figure 3.15 presents also the $\bar{p}p$ effective mass distribution for events in which the $p_f \pi^-$ is in the $\Delta^0(1236)$ and $N^*(1520)$ mass bands. One notices the important enhancement observed when $\Delta^0(1236)$ are selected, while the second bump disappears when the $p\pi^-$ is in the $N^*(1520)$ mass band. This is rather surprising as apparently no selection rule is supposed to suppress one of the $\bar{p}p$ bumps when the $N^*(1520)$ is present. Table 3.5 summarizes the values found for these enhancements as well as the corresponding cross-sections.

TABLE 3.5 - Parameters of the two enhancements found in $\pi^- p \to p_f \bar{p} p \pi^-$ reactions at 9 and 12 GeV/c

Central values ($M_{1,2}$) and widths ($\Gamma_{1,2}$) (MeV/c^2)	Incident momentum (GeV/c)	Cross-section for $\pi^- p \to \Delta(1236) X(\bar{p}p)$ (nb)	Cross-section for $\pi^- p \to N^*(1520) X(\bar{p}p)$ (nb)
$M_1 = 2020 \pm 3$	9	18 ± 5	30 ± 12
$\Gamma_1 = 24 \pm 12$	12	10 ± 4	26 ± 8
$M_2 = 2204 \pm 5$	9	17 ± 5	
$\Gamma_2 = 16 \,^{+20}_{-16}$	12	21 ± 5	

For the two runs the statistical significance for the 2020 and 2204 signals are 7.6 and 6.5 standard deviations, respectively, whenever $\Delta(1236) \rightarrow p_f\pi^-$ are selected in the final state. Nevertheless, some questions remain open about these enhancements. In particular, one can wonder why these enhancements are produced in the $\pi^- p \rightarrow \bar{p}p\Delta$ subchannel, while only one bump is seen (2020 GeV/c^2) when the $\bar{p}p$ is produced in conjunction with an $N^*(1520)$. Is it possible to interpret the observed bumps as resulting from the "$\bar{p}$"$p \rightarrow \bar{p}p$ processes ? If this should be the case, are the small observed cross-sections of the bumps due to the elastic resonant "$\bar{p}$"$p \rightarrow \bar{p}p$ scattering, or to the baryon exchange mechanism in the $\pi^- p \rightarrow p_f\bar{p}p\pi^-$ reaction? In any case, the available data on $\bar{p}p$ elastic and total cross-sections shown in Fig.3.16 do not present any signal around the 2020 and 2200 GeV/c^2 mass values[15,18]. Note that because of technical difficulties the elastic cross-section is only integrated in the c.m. angular scattering angle range of $-0.95 < \cos\theta^* < 0.95$. This is not really disturbing as one eliminates in this way mainly the contribution of the diffraction peak in the elastic scattering. The fact that one does not see any effect in free $\bar{p}p$ reactions needs of course further investigation. In any case, the study of virtual collisions is certainly a very promising approach for studying baryon-antibaryon reactions whenever the construction of antibaryon beams is not feasible.

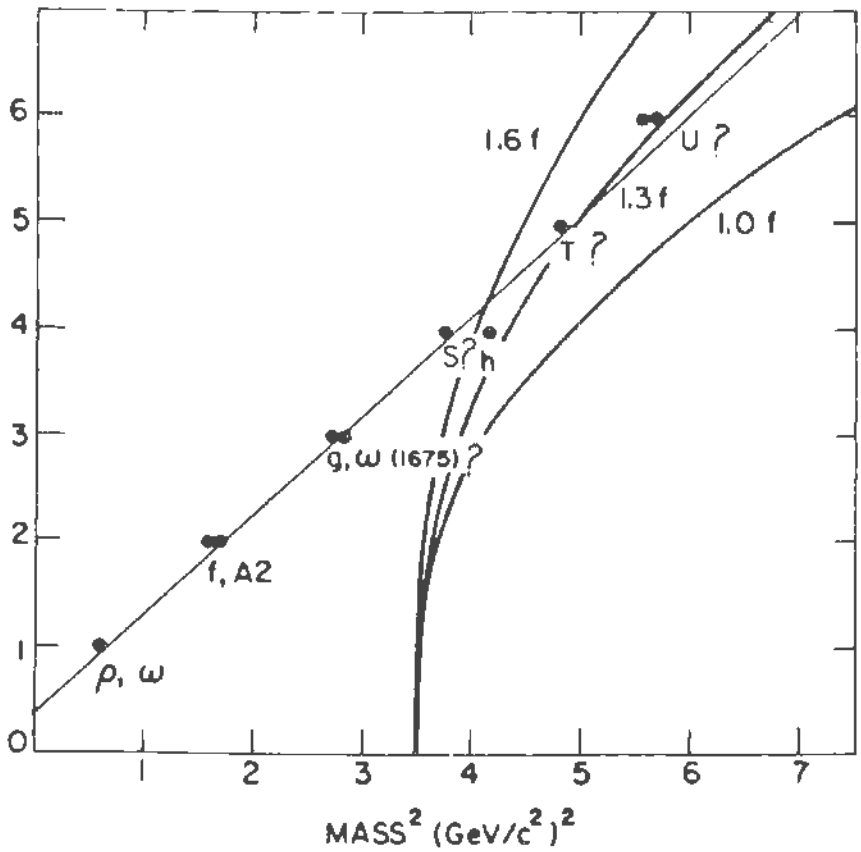

Figure 3.1

The J versus M^2 plot of some well established and conjectured meson states [Ref. (14)]. The curves indicate the $\bar{p}p$ impact parameter limit for various values for the interaction radius (R = 1.0 , 1.3 , 1.6 fm).

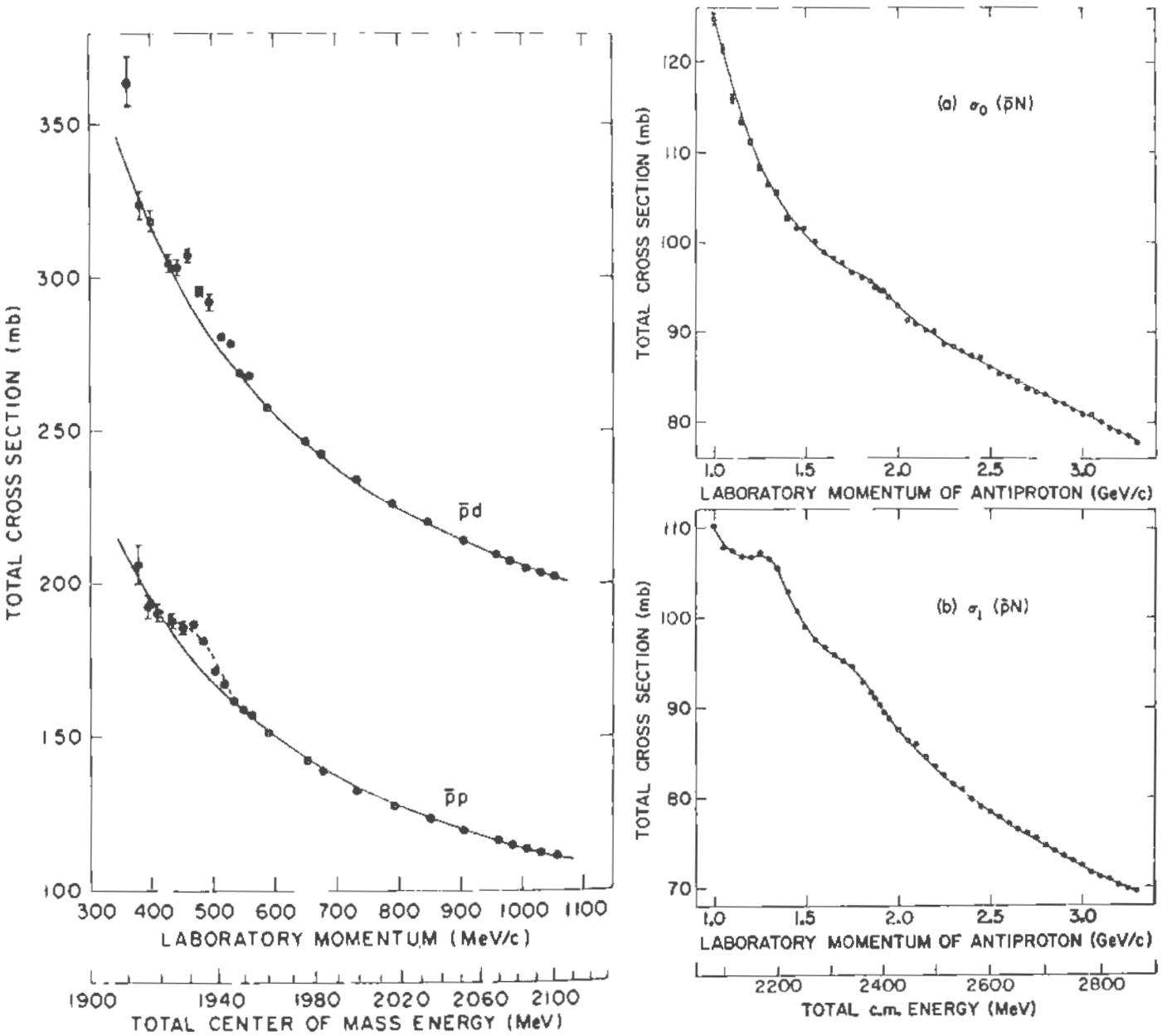

Figure 3.2

The $\bar{p}p$ and $\bar{p}d$ total cross sections (left hand side) in the $\bar{p}$ incident momentum range 0.4 – 1.05 GeV/c [Ref.16]. The isospin decomposition of the total cross section (right hand side) into the isospin I = 0 (σ_0) and I = 1 (σ_1), taken from Ref.15.

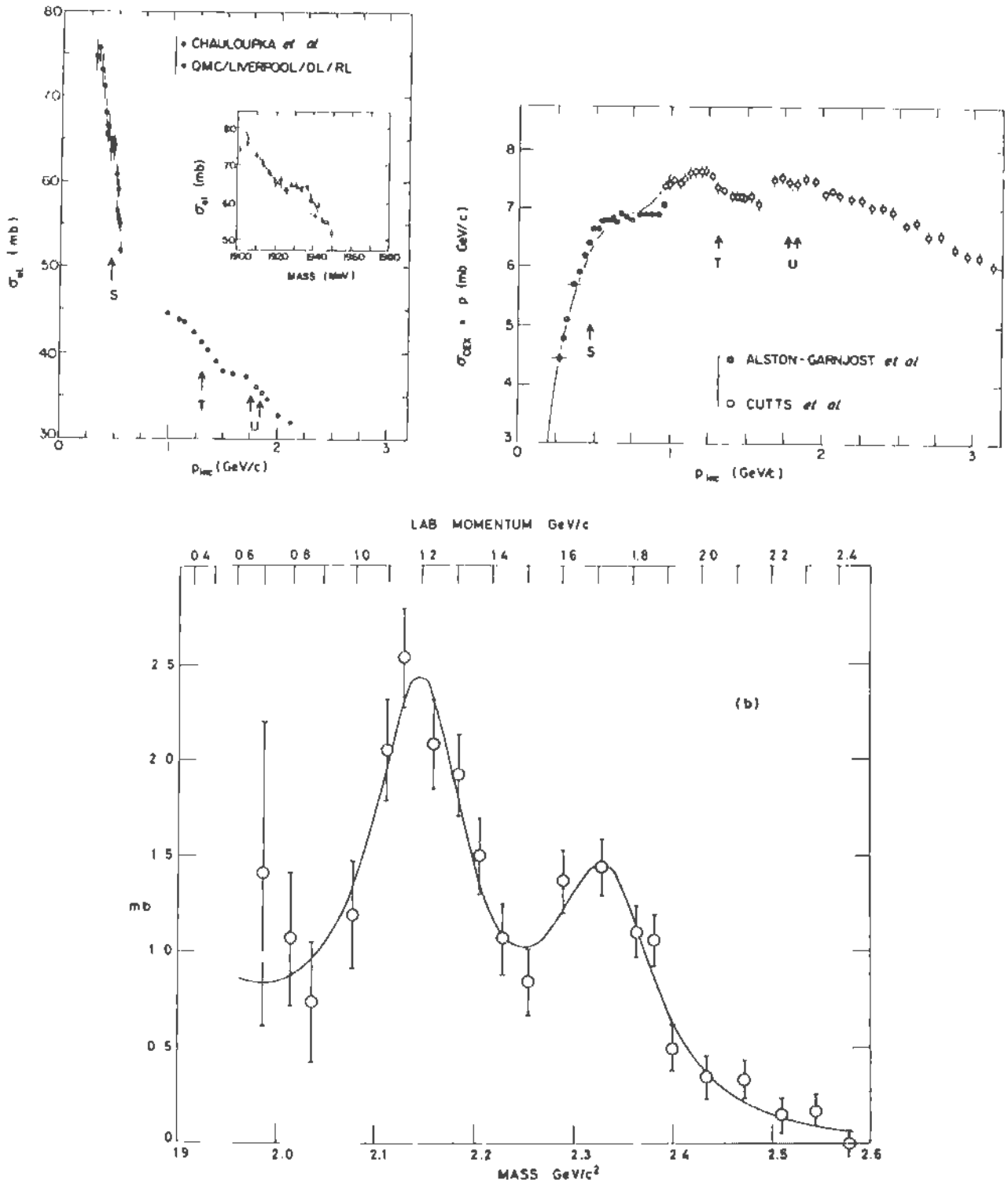

Figure 3.3

The elastic (left hand side top) and charge exchange (right hand side top) cross section as a function of the incident laboratory momentum, taken from ref.14. The partial elastic cross section (bottom) after background substraction in the U region. The curve represents a fit to the data as done in ref.18.

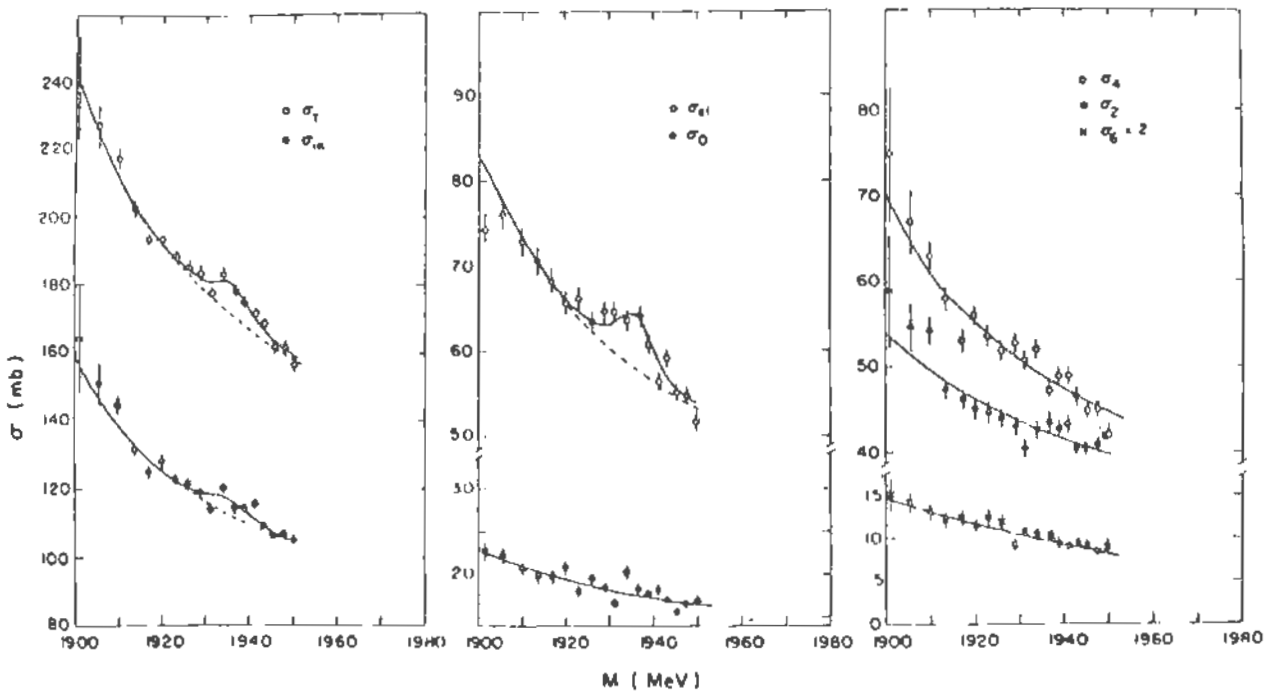

Figure 3.4

Some $\bar{p}p$ channel cross sections in the S region, from ref. 19.

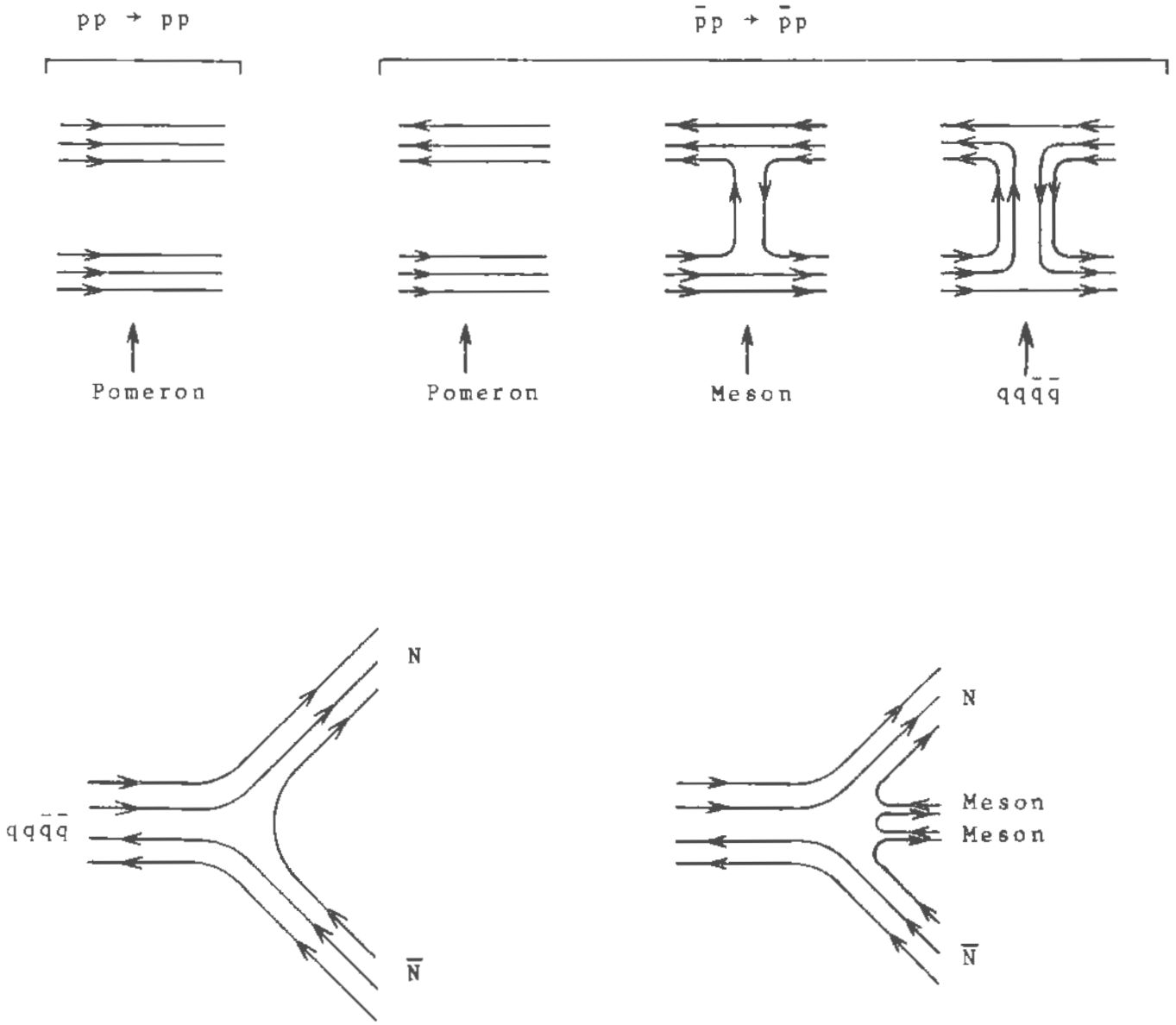

Figure 3.5

Dual diagrams (top) contributing to the elastic pp and $\bar{p}p$ scattering with the corresponding t - channel exchanges. Examples of decays of the exotic $qqq\bar{q}\bar{q}$ state (bottom) into the systems $\bar{N}N$ and $\bar{N}\bar{N}$ with two mesons

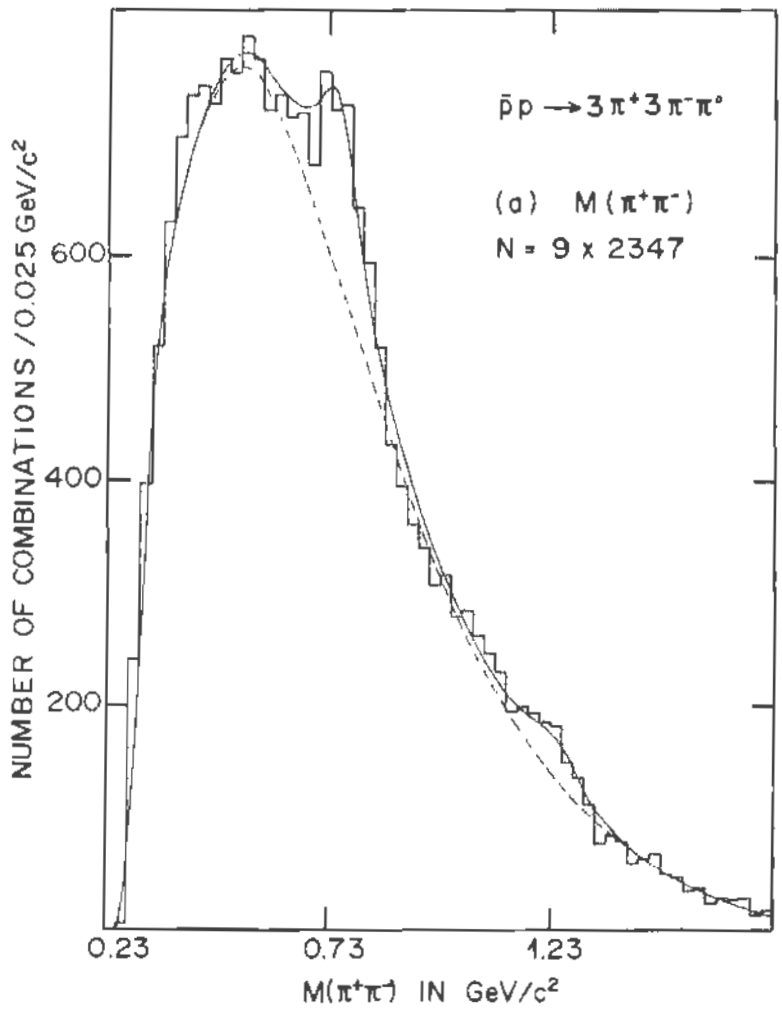

Figure 3.6

Example of the $\pi^+\pi^-$ effective mass distribution obtained in the $\bar{p}p \rightarrow 3\pi^+3\pi^-\pi^o$ reaction at 5.7 GeV/c. The full curve is obtained by fitting the data with an incoherent mixture of a multiregge peripheral background and two Breit - Wigner functions due to ρ and f resonances (ref.22). Note the important background under the ρ peak due in particular to the high combinational background.

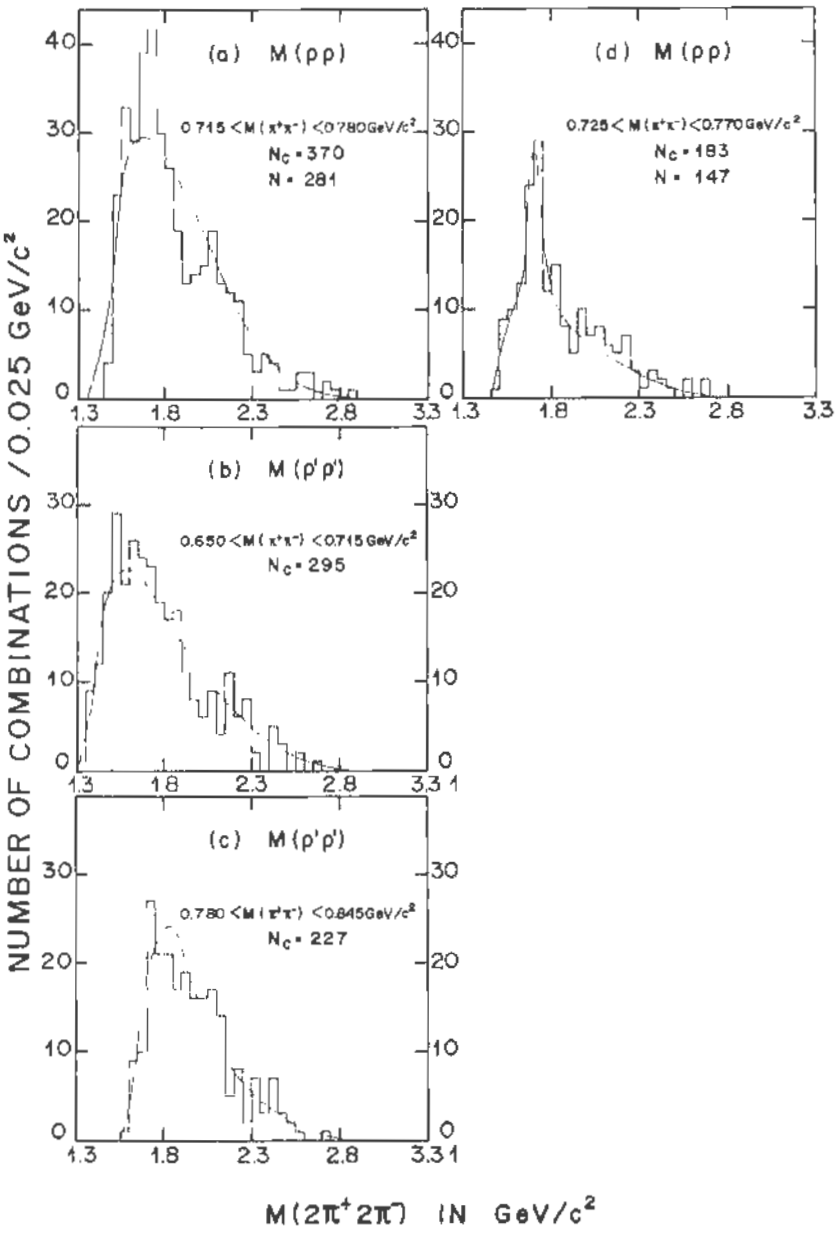

Figure 3.7

The $2\pi^+2\pi^-$ [$M(2\pi^+2\pi^-)$] effective mass distributions having two distinct $\pi^+\pi^-$ [ρ or ρ'] mass combination in various $M(\pi^+\pi^-)$ mass intervals. In (a), (b) and (c) the curves represent the phase space predictions. In (d) the data are fitted with an incoherent mixture of phase space and a Breit - Wigner function. The width observed of the enhancement reflects merely the cuts made to define the $\pi^+\pi^-$ mass intervals. Note that the enhancements are only seen when $\rho\rho$ events are selected [Ref.22].

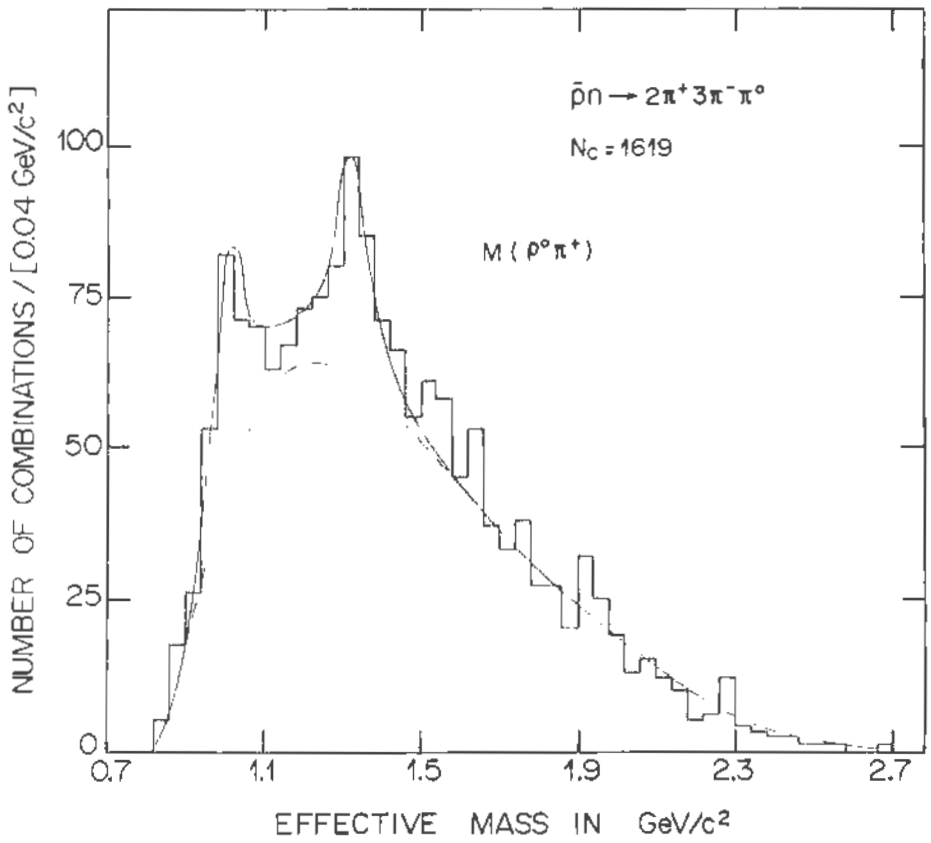

Figure 3.8

The $\rho^o\pi^+$ effective mass distribution obtained in the $\bar{p}n \rightarrow 2\pi^+3\pi^-\pi^o$ reaction at 5.55 GeV/c incident momentum [Ref.24].

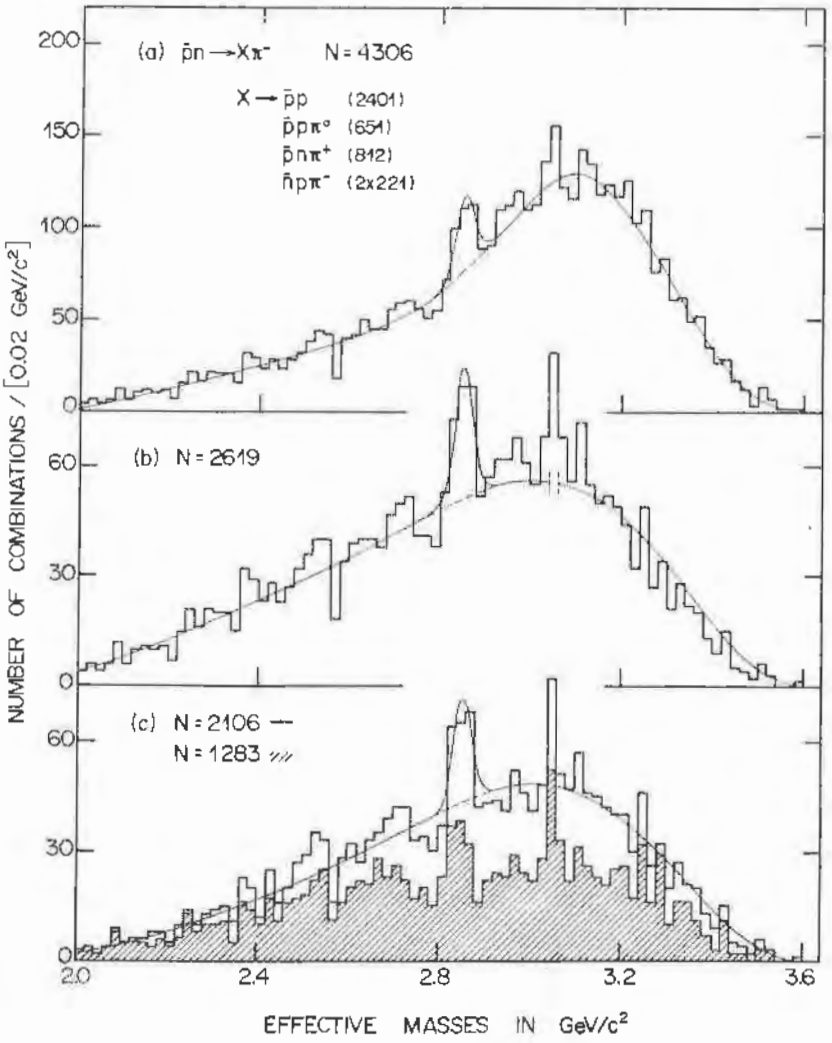

Figure 3.9

The distributions of the effective mass of X for the $\bar{p}n \to \pi^- X$ reaction at 5.55 GeV/c obtained from the channels $\bar{p}n \to \bar{p}p\pi^-$ (1), $\bar{p}n \to \bar{p}p\pi^-\pi^o$ (2), $\bar{p}n \to \bar{p}n\pi^+\pi^-$ (3) and $\bar{p}n \to \bar{n}p\pi^-\pi^-$ (4).

(a) all the events, (b) the sample obtained by excluding $\bar{\Delta}^{--}(1236)$ from channels (1), (2) and (3) and the $\Delta^-(1236)$ from channels (3) [In channel (3) $\bar{\Delta}^{--}$ and Δ^- are produced in equal amounts], (c) the sample obtained by excluding in addition from channel (1) the $\bar{\Delta}(1900)$ and the events having $1.52 < M_{p\pi^-} < 1.74$ GeV/c. The shaded area is obtained from channel (1) and (2) using the same cuts as in (2). The full curves represent the fit of the data using a polynomial background and a Breit-Wigner function [Ref. 25].

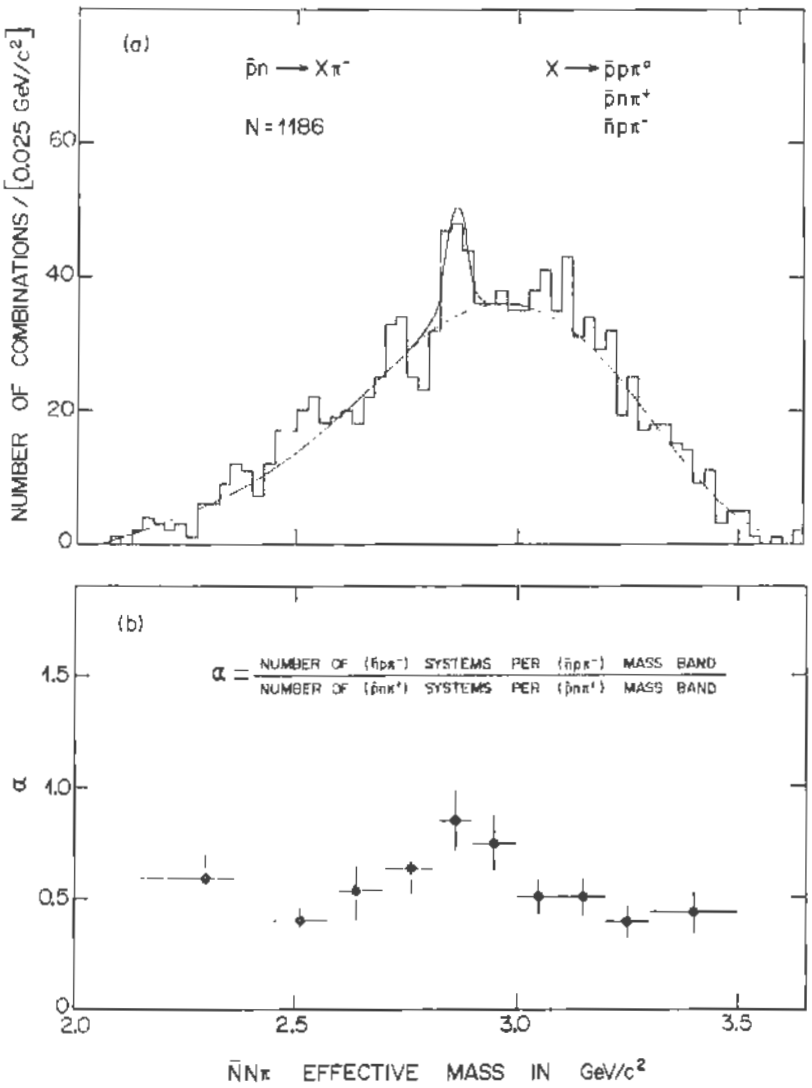

Figure 3.10

(a) The distribution of the X mass obtained from the various $\bar{p}n \rightarrow \bar{N}N\pi\pi$ reactions, the events with $\bar{\Delta}^{--}$ being excluded as well as that with Δ^- in the $\bar{p}n \rightarrow \bar{p}n\pi^+\pi^-$ reaction . The full curve is a fit to the data using a polynomial background and a gaussian function for describing the enhancement.

(b) The ratio α of the number of $\bar{n}p\pi^-$ systems to the $\bar{p}n\pi^+$ ones obtained from the $\bar{p}n \rightarrow \bar{n}p\pi^-\pi^-$ and $\bar{p}n \rightarrow \bar{p}n\pi^+\pi^-$ channels, respectively, as a function of the $\bar{N}N\pi$ mass. Note that for a real resonance decaying strongly one has $\alpha = 1$. The data shows that α tends to unity at the mass of the 2.85 GeV/c enhancement

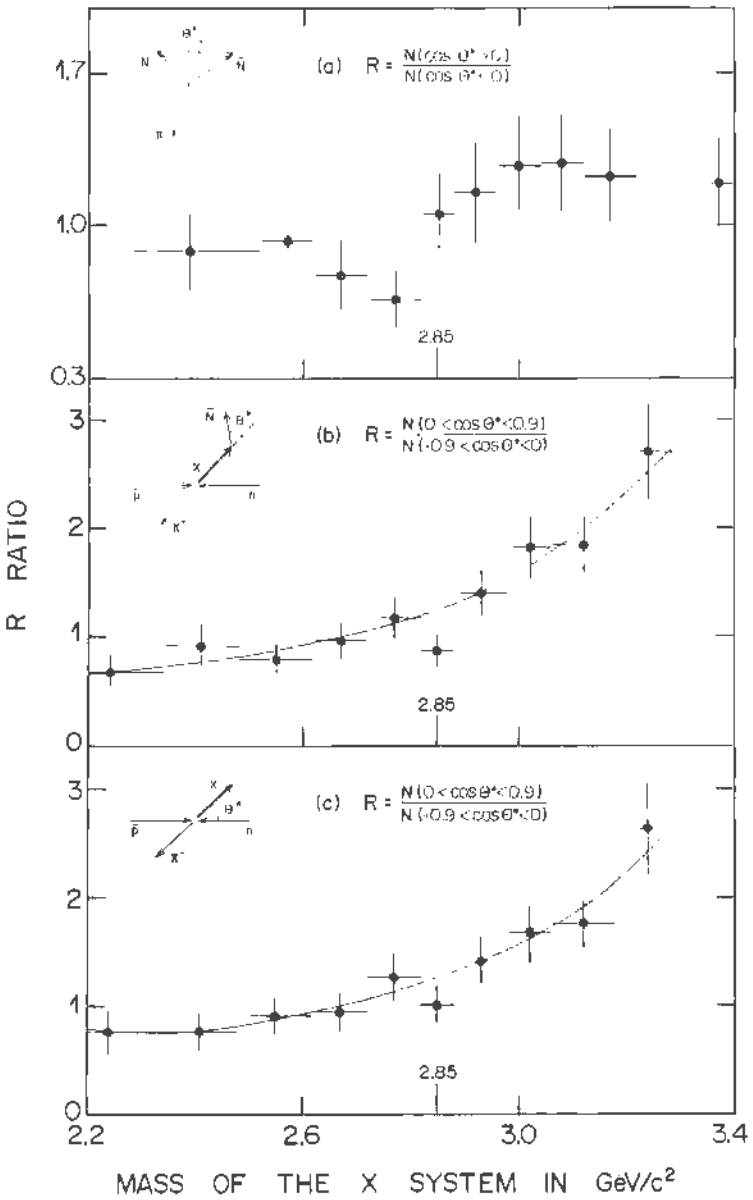

Figure 3.11

Distribution of the R ratio calculated from several angular distributions, the angles θ^* being defined in the figure.
(a) The $\bar{p}n \to X(\bar{N}N\pi)\pi^-$ reactions (same sample as in the previous figure), θ^* being now defined in the X rest frame.
(b) and (c). All the channels selected as in Fig.3c. The curves are polynomial fits to the data. Note that some structure is visible at the X mass of 2.85 GeV/c^2

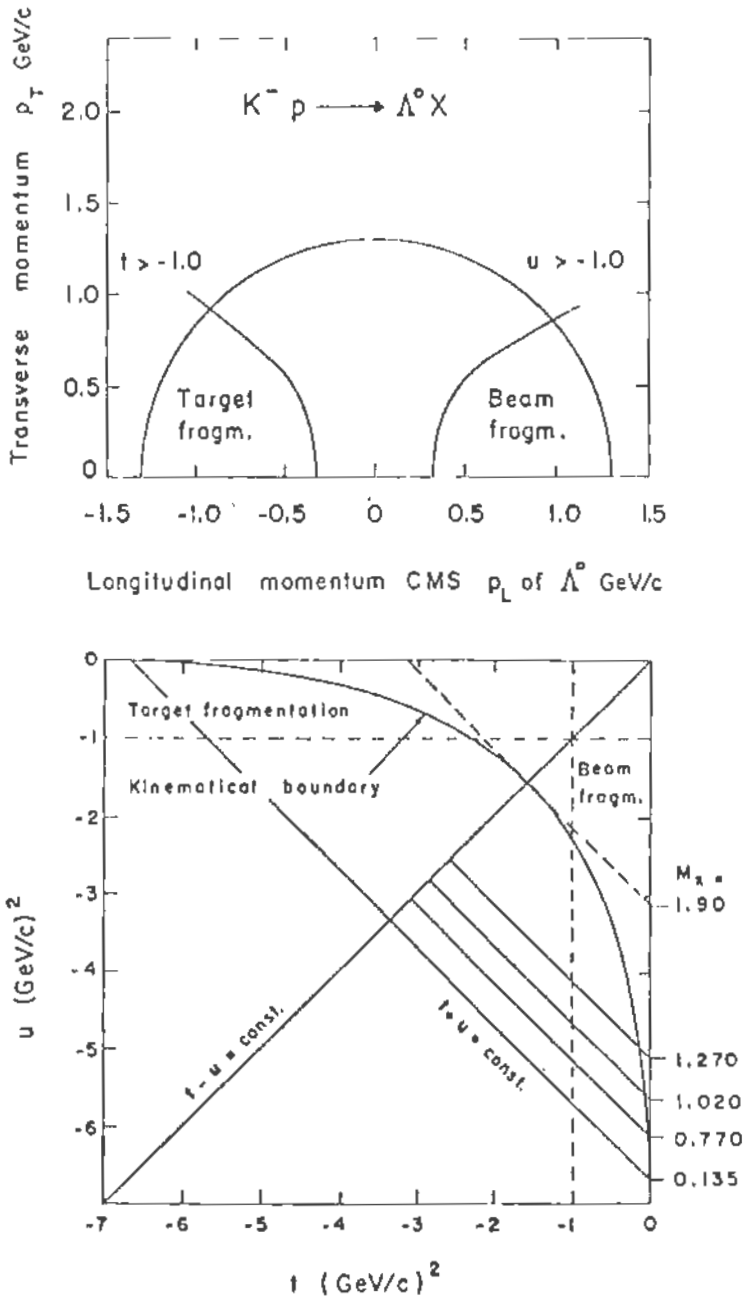

Figure 3.12

Target and fragmentation boundaries in the transverse and c.m. longitudinal plane (top). The same boundaries in the u, t plane (bottom). Note that lines of t + u = constant correspond to constant X mass (Ref.27).

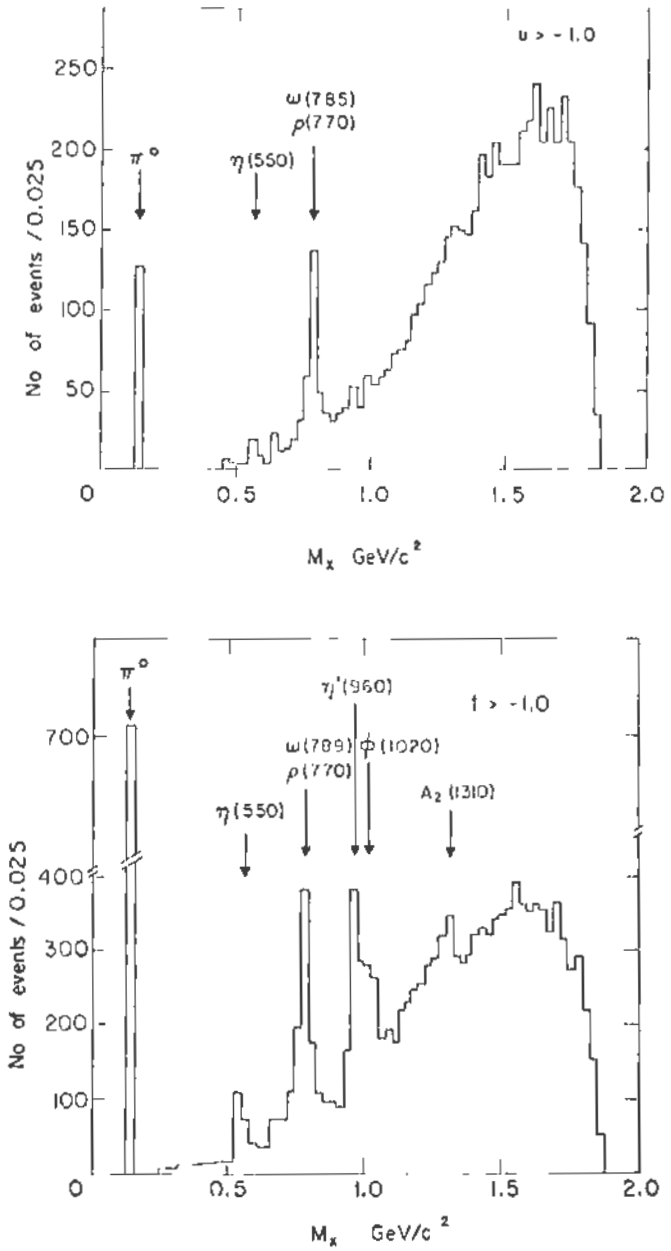

Figure 3.13

The distribution of the X mass in the virtual $"K^-"K^+ \to X$ (top) and $"\bar{p}"p \to X$ (bottom) processes

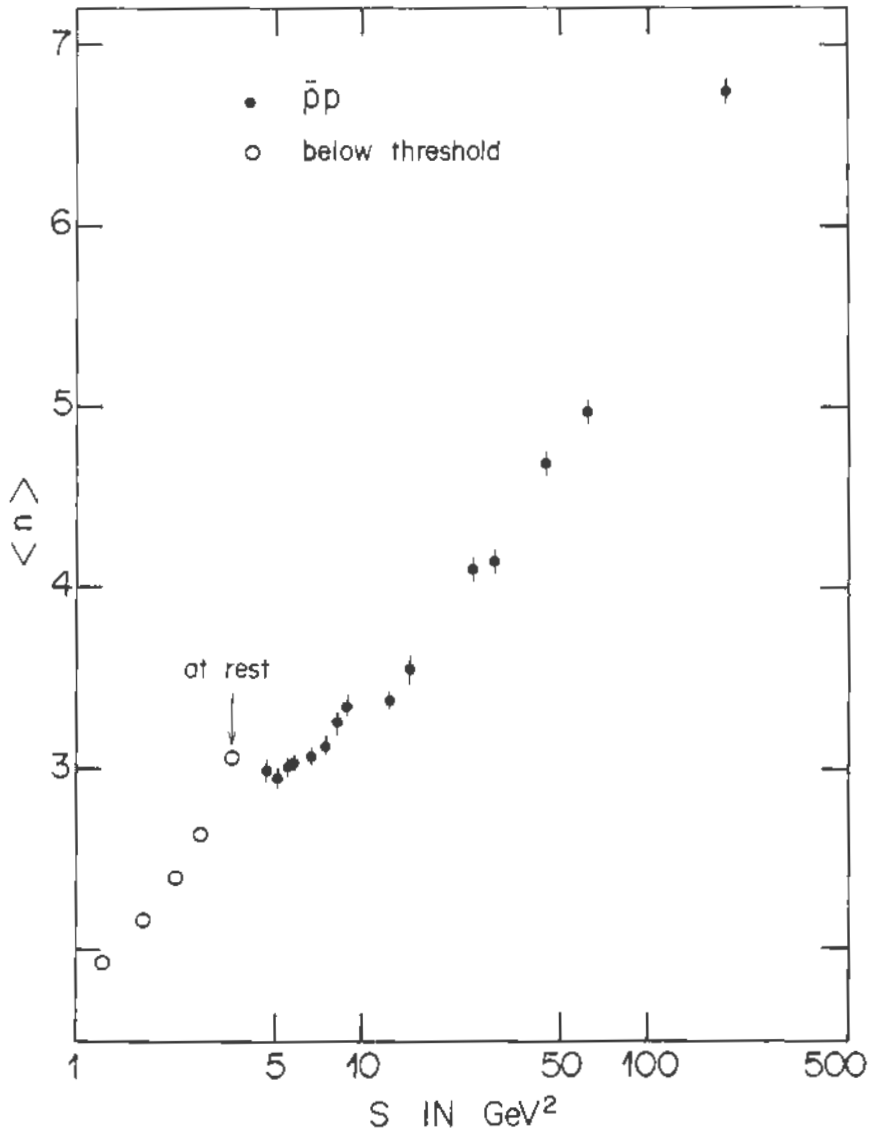

Figure 3.14

The average number of charged particles in $\bar{p}p$ collisions below (Ref.27) and above (Ref.54) threshold as a function of the square of the c.m. energy

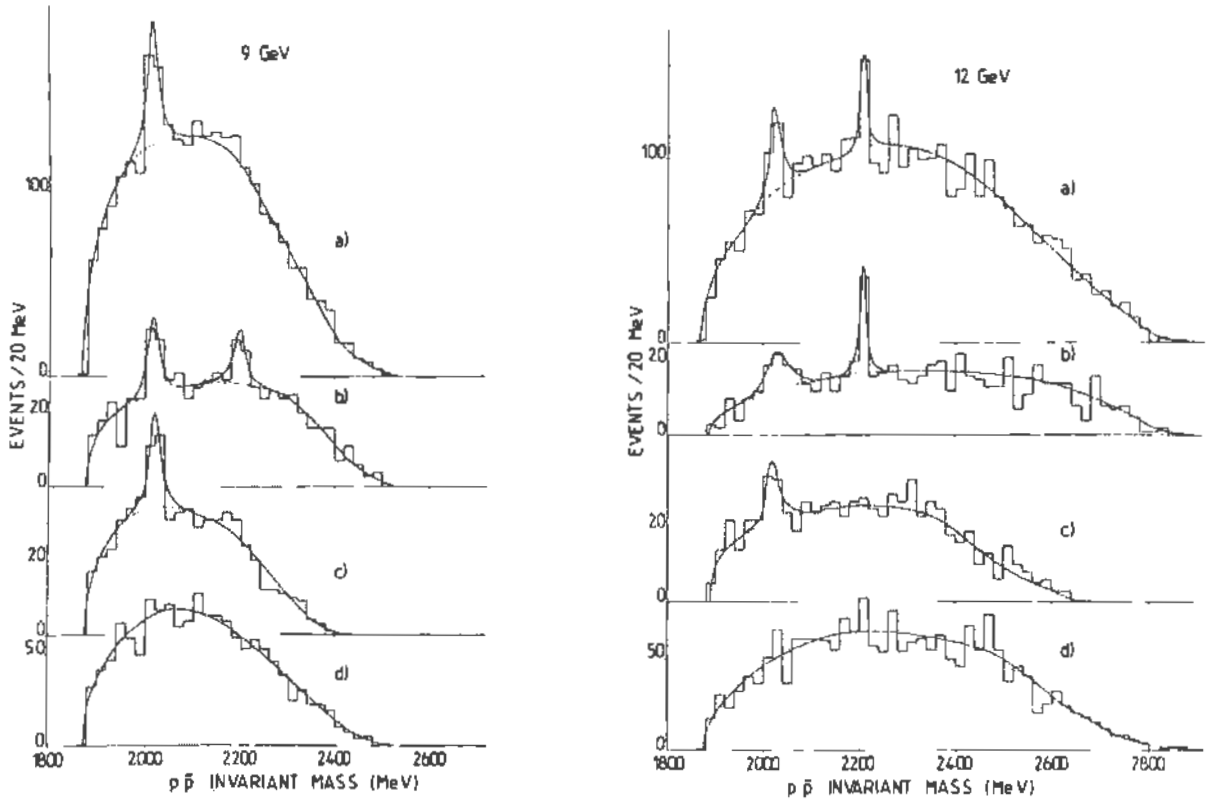

Figure 3.15

The $\bar{p}p$ effective mass distributions obtained in the $\pi^- p \to p_f \bar{p} p \pi^-$ reaction at 9 and 12 GeV/c incident momentum: (a) all the events; (b) events with $p_{f\pi^-}$ in the $\Delta^0(1236)$ region defined as $1.175 < M(p_{f\pi^-}) < 1.3$ GeV/c^2; (c) events with invariant $p_{f\pi^-}$ in the $N^*(1520)$ region, $1.45 < M_{p_f\pi^-} < 1.6$ GeV/c^2; (d) events with invariant $p_{f\pi^-}$ mass outside (b) and (c). The full curve represent the fit of the data with a smooth background with or without Breit-Wigner functions (Ref.28)

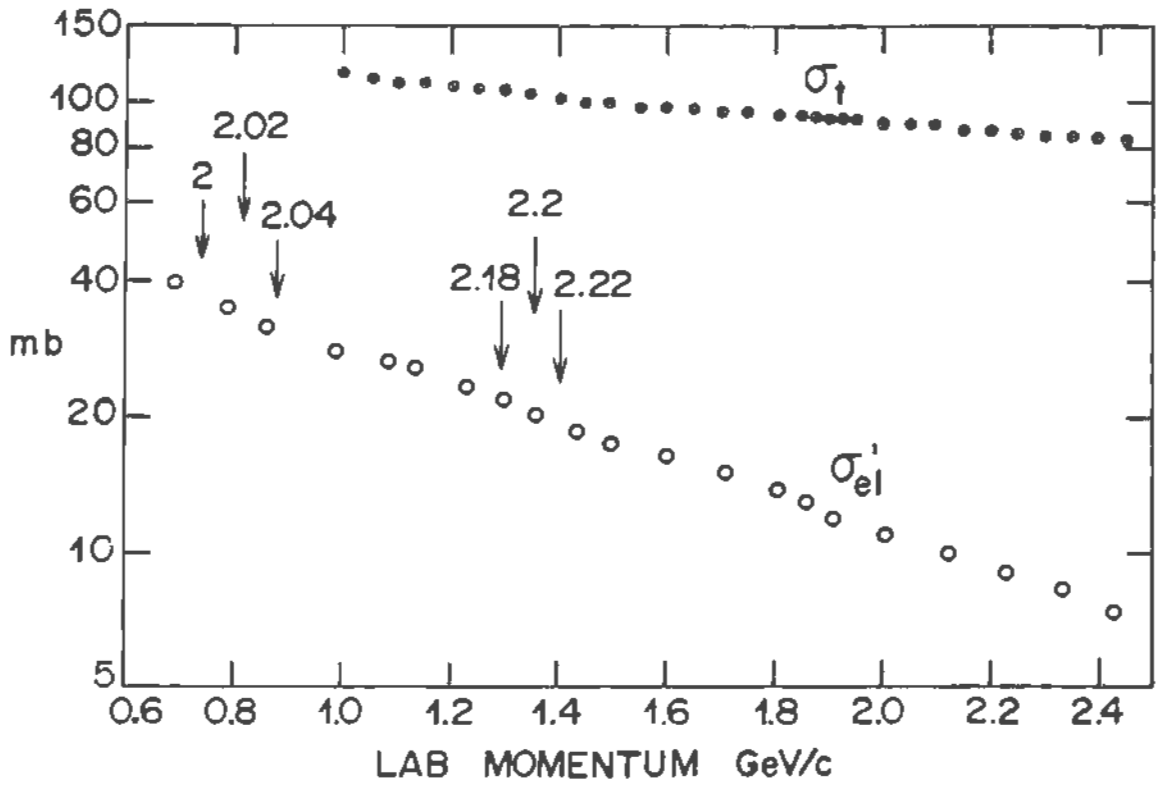

Figure 3.16

The $\bar{p}p$ total (σ_t) and elastic (σ'_e) cross-sections as a function of the incident momentum. Note that because of technical difficulties the elastic cross-section is only integrated in the c.m. angular scattering angle range of $-0.95 < \cos\theta^* < 0.95$ [Ref.15, 18].

4. PRODUCTION FEATURES

4.1 - Introduction

An impressive amount of data has been accumulated on non-annihilation channels. Production mechanism, resonance production, and correlation features have been extensively studied. In some respects, however, these investigations may be considered as somewhat disappointing. Indeed, in the present status of strong interactions physics, it is not easy to synthesize the present experimental knowledge. Nevertheless, the accumulation of data was certainly useful, as many phenomena which were discovered (or simply observed) led to a better understanding of strong interaction processes. Let us only remember that experimental evidence such as, for instance, limited transverse momentum of the secondaries, behaviour of cross-sections, Regge or multi-Regge features of the data, multiplicity information, and resonance production are all facts which have to be known if we hope to have some time a theory able to explain multiparticle production phenomena.

It is, of course, beyond the scope of the present note to make a review of the important experimental efforts devoted to multiparticle production processes. However, even if the final state is as simple as a two-body final state, many problems remain unsolved. Therefore as a example of inelastic reactions we choose to discuss here two kind or reactions dealing with the two-body final state, namely the $\bar{p}p \to \bar{\Sigma}\Sigma$ and the $\bar{p}n \to \bar{\Delta}^{--}p$ reactions.

4.2 - The $\bar{p}p \to \bar{\Sigma}\Sigma$ reaction

The $\bar{p}p \to \bar{\Sigma}\Sigma$ is an interesting reaction as the $\bar{p}p \to \bar{\Sigma}^{-}\Sigma^{-}$ channel is produced via exotic exchange in the t - channel (Fig.4.1). Search for exotic states, i.e. those which are not built by the usual quark structure $\bar{q}q$ or qqq, was intensively carried out. Another way to search for such states is to see whether they appear as exchanges in the t - channel. Of course, care is needed to determine if exotic exchange is not simulated by a two particle exchange.

Some years ago it was claimed that exotic exchanges have been observed in the $pn \to \Delta^{-}\Delta^{++}$ reaction at 7 GeV/c[29]. In fact all the experimental distributions obtained in this channel could also be obtained from the reaction $pn \to \Delta^{-}\pi^{+}p$, $\Delta^{++}\pi^{-}n$ (the two final states being charge symmetric), which simulates an apparent exotic exchange[30]. In this respect the $\bar{p}p \to \bar{\Sigma}^{-}\Sigma^{-}$ is a cleaner reaction,

the interpretation of which is much easier. The $\bar{p}p \to \bar{\Sigma}\Sigma$ reaction has been studied in bubble-chamber experiments at several incident momenta and in particular at 3.6 GeV/c, which is the experiment which will be discussed below[31].

There is also some inconvenience in using $\bar{p}p \to \bar{\Sigma}\Sigma$ reactions, as the $\bar{p}p \to \bar{\Sigma}^{+}\Sigma^{+}$ which proceeds without exotic exchange has the same topology (and appearance in the bubble chamber) as the $\bar{p}p \to \bar{\Sigma}^{-}\Sigma^{-}$ channel. From Table 4.1 one sees that $\bar{p}p \to \bar{\Sigma}^{+}\Sigma^{+}$ can appear in four different final states (including the decay particles), whereas the $\bar{p}p \to \bar{\Sigma}^{-}\Sigma^{-}$ has only one final configuration.

TABLE 4.1 - The final state particles (including the decay ones) obtained in $\bar{p}p \to \bar{\Sigma}\Sigma$ reactions

Reactions	$\bar{p}p \to \bar{\Sigma}^{+}\Sigma^{+}$	$\bar{p}p \to \bar{\Sigma}^{-}\Sigma^{-}$
Final state including the decay particles	$\bar{\Sigma}^{+}(\bar{n}\pi^{-})\Sigma^{+}(n\pi^{+})$ $\bar{\Sigma}^{+}(\bar{p}\pi^{0})\Sigma^{+}(n\pi^{+})$ $\bar{\Sigma}^{+}(\bar{n}\pi^{-})\Sigma^{+}(p\pi^{0})$ $\bar{\Sigma}^{+}(\bar{p}\pi^{0})\Sigma^{+}(p\pi^{0})$	$\bar{\Sigma}^{-}(\bar{n}\pi^{+})\Sigma^{-}(n\pi^{-})$

If one admits that the decay $\bar{p}$'s and p's can be recognized in the bubble chamber because of the low c.m. energy involved one remains with an ambiguity between the $\bar{\Sigma}^{+}(\bar{n}\pi^{-})\Sigma^{+}(n\pi^{+})$ and $\bar{\Sigma}^{-}(\bar{n}\pi^{+})\Sigma^{-}(n\pi^{-})$ final states (remember that the n and $\bar{n}$ are not detected in the bubble chamber). The separation between these states can easily be made on the basis of the c.m. angular distributions of the hyperons. Figure 4.2a gives the c.m. angular distribution of the identified $\bar{\Sigma}^{+}$, while in Fig.4.2b is given the distribution of the negative unidentified ($\bar{\Sigma}^{+}$ or Σ^{-}) negatively charged hyperon. The particles emitted backward (Fig.4.2b) are certainly Σ^{-}, as suggested by peripheral arguments (exotic charge Q = 2 exchanges are expected to be more likely than B = 2 exchanges). A better identification test can also be made by measuring the lifetime of the backward and forward particles in Fig.4.2b. Remember that the lifetime of the Σ^{-} and Σ^{+} (hence $\bar{\Sigma}^{+}$) are different.

As indicated in Fig.4.2, one indeed obtains different lifetimes for the backward and forward-emitted particles, allowing an unambiguous identification of the hyperons. Thus the identification of the $\bar{\Sigma}^{+}\Sigma^{+}$ and $\bar{\Sigma}^{-}\Sigma^{-}$ final states allowed the determination of the ratio of the cross-section with to that without exotic exchanges, namely[31]

$$\frac{\sigma(\bar{p}p \to \bar{\Sigma}^{-}\Sigma^{-})}{\sigma(\bar{p}p \to \bar{\Sigma}^{+}\Sigma^{+})} = 0.09 \pm 0.02$$

It appears that within the present available statistics all the two-body reactions with exotic exchanges represented in Fig.4.1, having all the same set of quantum numbers exchanged in the t - channel, have approximatively the same S^{-n} dependence ($n = 5 \pm 1$). This may suggest that the same type of mechanism governs theses processes. It is worth while to note that the similarity between processes in which the same quantum numbers, including an exotic $Q = 2$, are exchanged has been stressed in the study of the coherent inclusive $\bar{p}d \to \pi^{+}X$ reaction at 5.55 GeV/c[32]. By coherent inclusive reactions one means here that X has to contain at least a deuteron. The reaction $\bar{p}d \to \pi^{+}X$ was compared with $\pi^{-}p \to \pi^{-}X$ at 28 GeV/c in regions of the Feynman variable (x) associated with the outgoing π such that the same quantum numbers were exchanged in the t channel (see Fig.4.3). Then apart from a normalization factor, one sees from Fig.4.3 that the $|x|$ distribution has the same behaviour for both $\bar{p}d \to \pi^{+}X$ and $\pi^{-}p \to \pi^{-}X$ inclusive reactions.

Let us come back to the $\bar{p}p \to \bar{\Sigma}^{-}\Sigma^{-}$ channel. In order to explain the production of this reaction, essentially three phenomena can be considered[31] :

- s-channel resonance
- Two-particle exchange
- Exotic exchange

The s - channel resonance hypothesis will also predict that decays with the same abundance will occur via the $\bar{p}p \to \bar{\Sigma}^{+}\Sigma^{+}$ mode. Furthermore, the angular distribution of these decay $\bar{\Sigma}^{\mp}$ have to be symmetric in the c.m. if interference phenomena are negligible. As these facts are not verified by the data, the s-channel resonance hypothesis is not very likely. In order to choose between the two other hypotheses, one has to study the energy dependence of the $\bar{p}p \to \bar{\Sigma}^{-}\Sigma^{-}$ cross-section. The two-particle exchange which is equivalent to a cut in the

Regge pole terminology will lead to an S dependence of the cross-section containing terms in $\ell n S$. In contrast, one-particle exchange yields an $S^{\alpha}/\ell n S$ dependence. The cross-sections available as yet are not precise enough to choose between these hypotheses. One sees thus that precise data are still useful to study a production mechanism as simple as the discussed two-body final states. In fact, an increasing interest has been consecrated to exotic exchanges during recent years, because of problems connected with the existence of baryonium state.

4.3 - The $\bar{p}n \to \bar{\Delta}^{--}p$ reaction

Results on the $\bar{p}n \to \bar{p}p\pi^-$ reaction exist now in the 3...15 GeV/c incident $\bar{p}$ momentum region[33]. This reaction is dominated by a strong $\bar{\Delta}^{--}$ production. Figure 4.4 presents the cross-sections of the $\bar{p}n \to \bar{p}p\pi^-$ and $\bar{p}n \to \bar{\Delta}^{--}p$ reactions as a function of the incident laboratory momentum (P_{inc}). One notices the power law decrease of the cross-sections, namely

$$\sigma(\bar{p}n \to \bar{p}p\pi^-) \approx P_{inc}^{-(1.04 \pm 0.06)}$$

and

$$\sigma(\bar{p}n \to \bar{\Delta}^{--}p) \approx P_{inc}^{-(2.1 \pm 0.1)}$$

The immediate idea that one can have is to compare the $\bar{p}n \to \bar{p}p\pi^-$ and $\bar{p}n \to \bar{\Delta}^{--}p$ with their line-reversed reactions, i.e. $pp \to pn\pi^+$ and $pp \to \Delta^{++}n$, respectively. These line-reversed reactions have the same P_{inc} dependence as the original reactions[33,34], so that one has (within the present statistics)

$$\frac{\sigma(pp \to pn\pi^+)}{\sigma(\bar{p}n \to \bar{p}p\pi^-)} = 4.0 \pm 0.7$$

and

$$\frac{\sigma(pp \to \Delta^{++}n)}{\sigma(\bar{p}n \to \bar{\Delta}^{--}p)} = 2.7 \pm 0.7$$

The first ratio is difficult to interpret since we are dealing with three particles on the final state. The second ratio is even greater than 2.7 if individual points at the same P_{inc} are compared. Furthermore, it is rather surprising that in the 3...15 GeV/c range the distribution of the four-momentum transfer t is more steeper for the $pp \to \Delta^{++}n$ than for the $\bar{p}n \to \bar{\Delta}^{--}p$ reaction. Here t is the four momentum transfer between the incident p ($\bar{p}$) and the outgoing Δ^{++} ($\bar{\Delta}^{--}$). By fitting the differential cross section with exponential e^{bt}

functions one finds that in the 3...15 GeV/c range the slopes b are of the order of 10 and 5 $(GeV/c)^{-2}$ for the $pp \to \Delta^{++}$ and $\bar{p}p \to \bar{\Delta}^{--}p$ reactions, respectively.

It is clear that a simple Regge pole model with exchange degeneracy cannot account for these facts if one assumes that the A_2 and ρ trajectories are the dominating contributions to the production processes[33-35]. Indeed by going from a reaction to its crossed one the original production amplitude is transformed by changing the sign of the contribution with odd signature trajectories[36]. Let us parametrize the Regge amplitude for the $pp \to \Delta^{++}n$ reaction by [35]

$$T = \beta_\rho(S,t)[1 - e^{i\pi\alpha_\rho(t)}] + \beta_A(S,t)[1 + e^{i\pi\alpha_A(t)}],$$

where $\alpha_\rho(t)$ and $\alpha_A(t)$ are the ρ and A_2 trajectories. Here $\beta_{\rho,A}(S,t)$ contains the S dependence of the amplitude and expressions in t depending on the residue functions. By assuming exchange degeneracy or even its weak form, stating only that $\alpha_\rho(t) = \alpha_A(t)$ $[\beta_\rho(S,t) \neq \beta_{A_2}(S,t)]$, the ρ and A_2 trajectories have a relative phase of $\pi/2$. This means that by squaring the amplitude there is no interference term. Therefore the crossed amplitude for the $\bar{p}n \to \bar{\Delta}^{--}p$ reaction leads to the same t dependence as for the $pp \to \Delta^{++}n$ reactions. The fact that this is not so cannot be explained easily even by assuming that absorption corrections are important, these being roughly proportional to the total cross section of the colliding particle. It is indeed hard to believe that these corrections will be responsible in the 3...15 GeV/c incident momentum range for

- the constant slopes $b \simeq 10,\ 5\ (GeV/c)^{-2}$ for the $pp \to \Delta^{++}n$ and $\bar{p}n \to \bar{\Delta}^{--}p$ reactions, respectively,
- P_{inc} independency of the cross section ratio $\sigma(pp \to \Delta^{++}n)/\sigma(\bar{p}n \to \bar{\Delta}^{--}p)$.

The examples discussed above show that even in the most simple production cases, many facts remain as yet not understood. The simple models generally used for describing the data give only a partial view of the experimental situation. It is therefore easy to conceive that further efforts will certainly be necessary for the description of more complicated reactions such as multiparticle production.

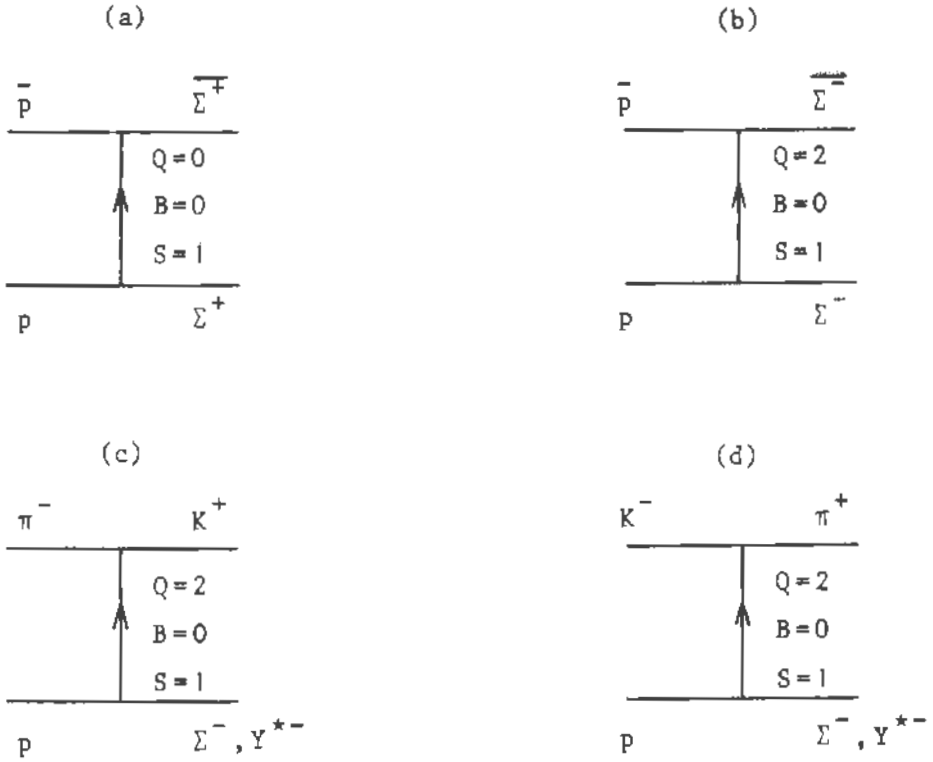

Figure 4.1

Diagrams which may contribute to the production of the reactions $\bar{p}p \to \overline{\Sigma^+}\Sigma^+$ via meson exchange (a) and $\bar{p}p \to \overline{\Sigma^-}\Sigma^-$ via exotic exchange (b). The other production diagrams [(c) and (d)] have as in (b) the same set of quantum number which being exchanged in the t - channel.

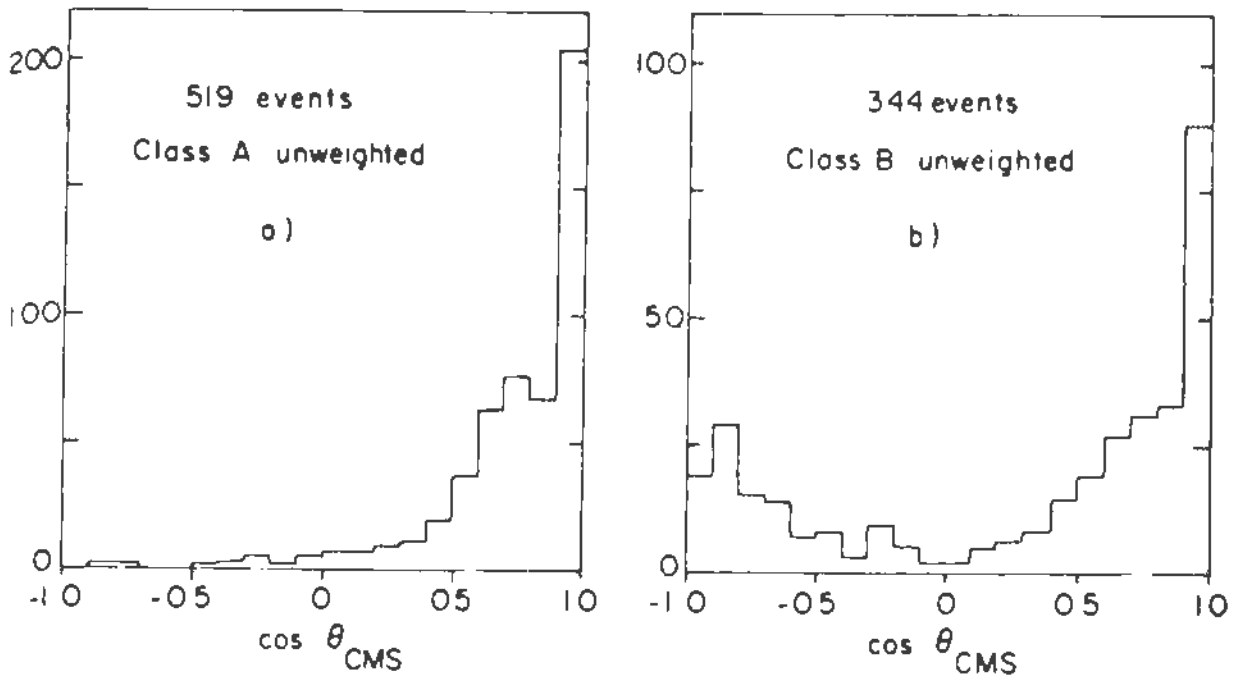

Figure 4.2

Cosine of the c.m. production angle between the incoming $\bar{p}$ and the negatively charged $\overline{\Sigma^+}$ (a) and for the events which are ambiguous between the $\overline{\Sigma^+}(n\pi^-)\Sigma^+(n\pi^+)$ and the $\overline{\Sigma^-}(\bar{n}\pi^-)\Sigma^-(n\pi^-)$ final state (b) [Ref. 31]. In (b) the backward events ($\cos\theta_{CMS} < 0$) are Σ^- as verified from the lifetime measurement $\tau_B = 1.45 \pm 0.12\ 10^{-10}$S (to be compared with the tabulated value $\tau_{\Sigma^-} = 1.48\ 10^{-10}$S) while the forward ones gives $\tau_F = 0.82 \pm 0.04\ 10^{-10}$S (tabulated values of Σ^+ is $\tau_{\Sigma^+} = 0.80 \pm 10^{-10}$S)

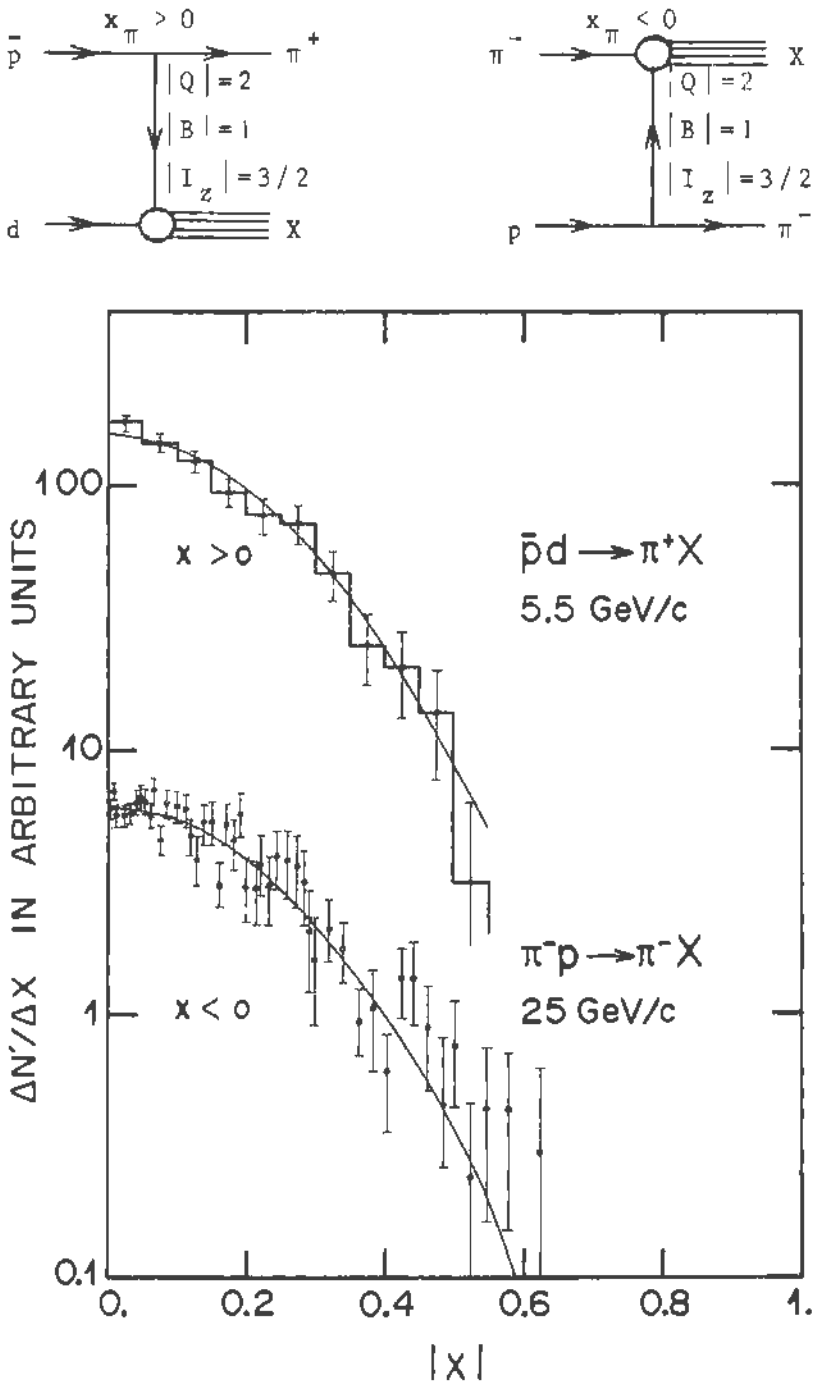

Figure 4.3

The distribution of the absolute value of the Feynmann variable of the π for the 5.55 GeV/c $\bar{p}d \rightarrow \pi^+ X$ (Ref. 32) and for the 25 GeV/c $\pi^- p \rightarrow \pi^- X$ processes [Phys. Rev. Lett., 26, 280 (1970)] obtained in the regions of $x > 0$ and $x < 0$, respectively. These regions correspond to possible diagrams (top figures) in which the same set of quantum numbers are exchanged in the t-channel. The lower curve is obtained by fitting the $\pi^- p$ data using a polynomial expression and was then normalized to the $\bar{p}d$ data.

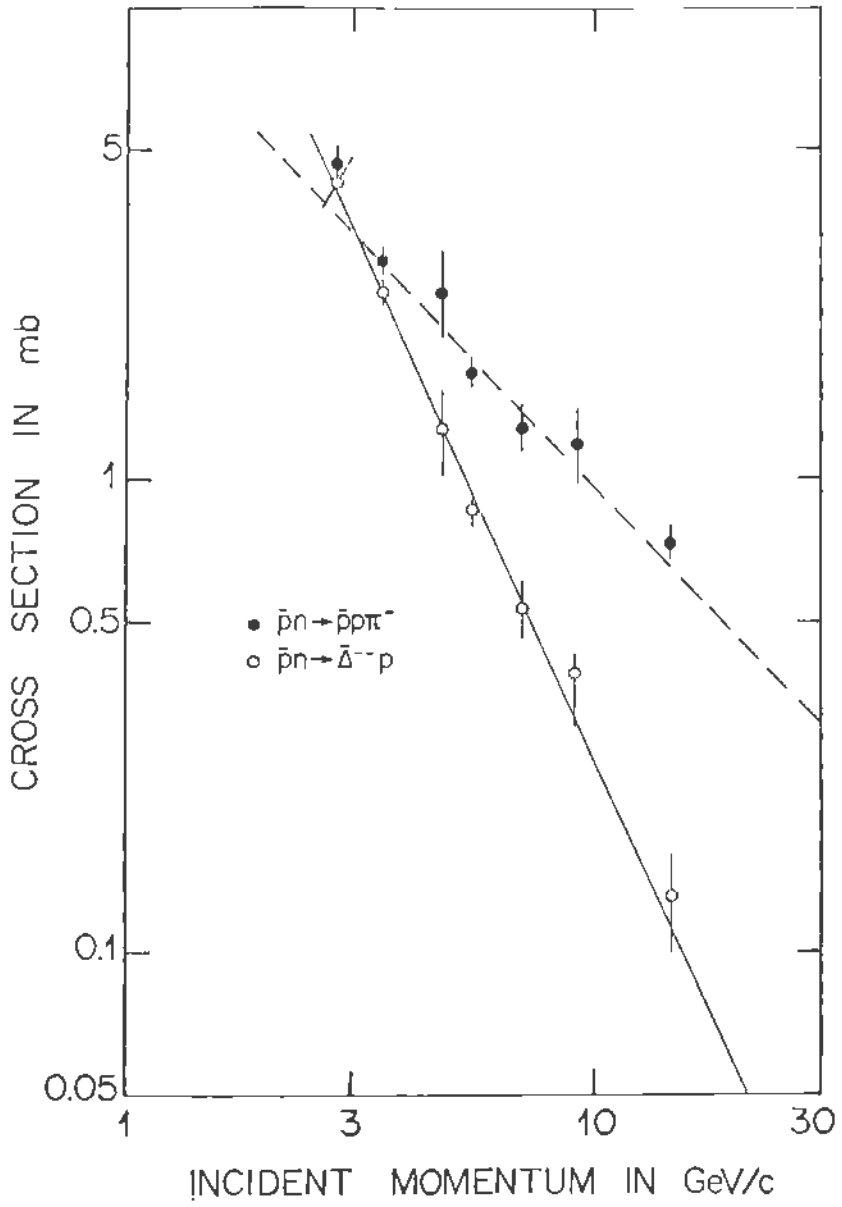

Figure 4.4

Variation of the $\bar{p}n \to \bar{p}p\pi^-$ and $\bar{p}n \to \bar{\Delta}^{--}p$ cross sections as a function of the incident momentum [Ref.33].

5. TOTAL AND ANNIHILATION CROSS-SECTIONS

5.1 - Total cross-sections

The study of total cross sections is certainly one of the most simple ways to investigate multiparticle production phenomena. This is all the more true when the c.m. energy increases, as then elastic scattering and low multiplicity give only a small contribution to the total cross section. Figure 5.1 to 5.3 present a compilation of the total $\bar{p}p$ [$\sigma_t(\bar{p}p)$], $\bar{p}d$ [$\sigma_t(\bar{p}d)$] and $\bar{p}n$ [$\sigma_t(\bar{p}n)$] cross-sections as a function of the incident laboratory momentum[37,38]. Note that the maximum $\bar{p}$ incident momentum available as yet is 200 GeV/c. The errors on $\sigma_t(\bar{p}n)$ are of course larger than for $\sigma_t(\bar{p}p)$ because of the uncertainties introduced by extracting $\sigma_t(\bar{p}n)$ from $\bar{p}d$ data. For $P_{inc} \geq 10$ GeV/c the $\bar{p}$ data are also compared with other hadron - hadron cross-sections, showing how much $\bar{p}$ induced cross-sections are larger than the other ones.

From these data one sees that the following cross-section differences

$$\sigma_t(\bar{p}d) - \sigma_t(pd)$$

$$\sigma_t(\bar{p}p) - \sigma_t(pp)$$

$$\sigma_t(\bar{p}n) - \sigma_t(pn)$$

have nearly the same S dependence[38,39], namely $S^{-(0.61 \pm 0.04)}$. As the $\sigma_t(pd)$ and $\sigma_t(pp)$ are increasing with $\sqrt{S}$ (see Fig.5.1 and 5.2) while the above differences decrease, it is likely that $\sigma_t(\bar{p}d)$ and $\sigma_t(\bar{p}p)$ will also increase above $P_{inc} \gtrsim 200$ GeV/c.

In the framework of the Regge pole model, and using the optical theorem, let us express $\sigma_t(\bar{p}N)$ by means of the leading t - channel singularities :

$$\sigma_t(\bar{p}p) = \text{Im}\,[P + P' + \omega + \rho + A_2]$$

$$\sigma_t(pp) = \text{Im}\,[P + P' - \omega - \rho + A_2]$$

$$\sigma_t(\bar{p}n) = \text{Im}\,[P + P' + \omega - \rho - A_2]$$

$$\sigma_t(pn) = \text{Im}\,[P + P' - \omega + \rho - A_2]$$

The symbols P, P', ω, ρ and A_2 represent the elastic scattering amplitudes at zero four-momentum transfer corresponding to the exchanges of the P, P', ω, ρ and A_2 Regge trajectories. The signs in front of the various contributions can be found in the following way[36]. By definition let us take all the amplitudes

with a positive sign for the total $\bar{p}p$ cross-section. Then $\sigma_t(pp)$ is obtained by changing the sign of the contribution due to the odd signature trajectories in $\sigma_t(\bar{p}p)$. This is a general Regge pole prescription relating a two-body channel to its line-reversed reaction. The expression for $\sigma_t(\bar{p}n)$ is also deduced from $\sigma_t(\bar{p}p)$. This time the isovector contributions change their signs because of the Clebsch - Gordan coefficients entering into the coupling of the isovector with a proton or a neutron. Finally $\sigma_t(pn)$ is obtained by the same procedures using the expression of $\sigma_t(pp)$ or that of $\sigma_t(\bar{p}n)$.

By forming differences between antiparticle and particle cross-sections, one can estimate the relative importance of the various exchanges. One has thus

$$\sigma_t(\bar{p}p) - \sigma_t(pp) = 2 \text{ Im } (\omega + \rho)$$

$$\sigma_t(\bar{p}n) - \sigma_t(pn) = 2 \text{ Im } (\omega - \rho)$$

The existing data show that these differences are nearly equal[38,39], i.e.

$$\sigma_t(\bar{p}p) - \sigma_t(pp) = 69.5 \; S^{-0.55}$$

$$\sigma_t(\bar{p}n) - \sigma_t(pn) = 61.2 \; S^{-0.55},$$

with σ_t in mb and S in GeV^2. This indicates that only one of the ω or ρ trajectories gives an important contribution to the $\sigma_t(\bar{p}N)$ and $\sigma_t(pN)$ cross-sections. One the other hand, since the differences

$$\sigma_t(\bar{p}p) - \sigma_t(\bar{p}n) = 2\text{Im}(\rho + A_2)$$

and

$$\sigma_t(pp) - \sigma_t(pn) = 2\text{Im}(\rho - A_2)$$

are very small, one concludes that ρ exchange (as well as A_2 exchange) is small, hence :

$$\sigma_t(\bar{p}N) - \sigma_t(pN) \approx 2 \text{ Im } \omega.$$

In the above approach Regge cuts generated by poles are neglected. However, by taking the difference between cross-sections some contributions due to cuts vanish such as, in particular, the vacuum cuts. The usual question that we can now ask ourselves is: are the $\sigma_t(\bar{p}N) - \sigma_t(pN)$ differences equal to the annihilation cross-sections? In other words are annihilations built via unitarity by the ω trajectory? This is the problem which will be discussed in the next section.

5.2 - Annihilation cross-section

It is rather clear that for low c.m. energies ($\sqrt{s} \sim 3.5$ GeV) the annihilation cross-section is certainly not equal to the difference between antiparticle and particle total cross sections. First of all the elastic $\bar{p}N$ and pN cross-sections are different at this c.m. energy, contributing thus to $\sigma_t(\bar{p}N) - \sigma_t(pN)$. Furthermore, this difference contains also a terms due to zero pronged events ($\bar{p}p \to$ neutrals) whenever the $\sigma_t(\bar{p}p) - \sigma_t(pp)$ difference is considered. At higher energy the influence of individual channels in the total cross-section becomes negligible. One can then investigate whether or not the annihilation processes are built by the ω trajectory. Figure 5.4 presents the total annihilation $\bar{p}p$ cross-sections $[\sigma_a(\bar{p}p)]$ for $P_{inc} \leq 12$ GeV/c together with the $\sigma_t(\bar{p}p) - \sigma_t(pp)$ above $P_{inc} > 12$ GeV/c, where no annihilation data exist yet[40,41]. The data points tend to be distributed on the same curve. One may thus conjecture that at high energy σ_a may be obtained from the $\sigma_t(\bar{p}p) - \sigma_t(pp)$ expression.

Another approach based on duality arguments has been proposed recently[42]. It was claimed that $\bar{N}N$ annihilations into mesons contribute mainly via unitarity to the Pomeron term in the total $\bar{N}N$ cross-section. A simple example can be given, supporting this idea[42]. Let us consider $\bar{\Delta}^{++}\Delta^{++}$ interactions which certainly contain an annihilation component. In the dual approach the elastic $\bar{\Delta}^{++}\Delta^{++}$ scattering processes is represented by three diagrams similar to $\bar{p}p$ scattering as shown in Fig.3.5. If one now considers $\bar{\Delta}^{=}\Delta^{++}$ interactions one is faced with a situation in which one particle is made by $\bar{d}$ quarks and the other by u quarks. As a u quark cannot annihilate a $\bar{d}$ quark the elastic $\bar{\Delta}\Delta^{++}$ scattering will only be represented by one dual diagram with Pomeron exchange. If $\bar{\Delta}^{++}\Delta^{--}$ interactions have an annihilation component it is hard to believe that such a component will not occur in $\bar{\Delta}^{=}\Delta^{++}$ interactions, both types of processes being related by isospin considerations. Thus if $\bar{\Delta}^{=}\Delta^{++}$ annihilations exist they must be related via unitarity to Pomeron exchange. The example mentioned simply shows that in some cases it is obvious that annihilations are related to Pomeron and not to ω exchange.

Figure 5.5 presents the dual diagrams leading to annihilation into mesons. These diagrams differ from one another in the sense that zero, one, or two quark lines are exchanged between the colliding $\bar{p}$ and p particles. By squaring the amplitude corresponding to each graph and summing over n, the total number of produced mesons, one can identify each production graph with one of the three dual diagrams contributing to the $\bar{p}p \to \bar{p}p$ scattering[42] (see Fig.5.5). In Fig.5.5

is also indicated the number of different diagrams obtained by permutation of quark lines in each dual diagram corresponding to an n-meson final state. One sees that when the c.m. energy increases, the number of dual diagrams identified with Pomeron exchange becomes dominant, simply as a result of the fact that on the average n is also increasing. This means that the annihilations will tend to be built mainly by Pomeron exchange. This has an interesting consequence if one tries to evaluate other type of annihilation cross-sections such as for instance antihyperon - proton $[\sigma_a(\bar{Y}p)]$[43] and to compare them with $\sigma_a(\bar{p}p)$.

The $\bar{Y}p$ annihilation cross-section (as well as the $\bar{N}N$ ones) can be written for an n-particle final state as

$$\sigma_a^n(\bar{Y}p) = N_X\,\sigma_X + N_M\,\sigma_M + N_P\,\sigma_P,$$

neglecting any interference phenomena[43]. Here N_X, N_M, and N_P are the numbers of dual diagrams contributing via unitarity to exotic, meson and Pomeron exchange with the individual cross-section σ_X, σ_M and σ_P. In order to compare $\sigma_a(\bar{Y}p)$ with $\sigma_a(\bar{p}N)$, additional hypotheses have to be made. One can first assume that the individual cross-sections are equal, $\sigma_{X,M,P} = \bar{\sigma}$. Then an estimate should be made for $\bar{\sigma}$ by using $\bar{p}p$ annihilation data[43]. With the same assumptions, the $\bar{p}p$ n-meson annihilation cross-section will be given by $\sigma_a^n(\bar{p}p) = 3^n\,\bar{\sigma}$. Using then instead of n the total average multiplicity $\langle n\rangle = \langle n_{charged}\rangle 3/2$ and $\sigma_a^{\langle n\rangle}(\bar{p}p)$ one may obtain an estimate for $\bar{\sigma}$. Assuming in addition that $\langle n\rangle$ is nearly equal for $\bar{Y}p$ and $\bar{p}p$ annihilations, one obtains the distribution $\sigma_a(\bar{Y}p)$ as a function of P_{inc}[43] shown in Fig.5.6. Although there are some uncertainties in the absolute scale, the figure shows that all the annihilation cross-sections tend to be equal beyond $P_{inc} > 15$ GeV/c. A totally different behaviour is obtained if one assumes that $\bar{Y}p$ annihilations are obtained from the difference $\sigma_t(\bar{Y}p) - \sigma_t(Yp)$. This is shown in Fig.5.7, in which these differences have been evaluated as a function of P_{inc} using the additive quark model.

Thus, the measurement of $\bar{Y}p$ annihilations will certainly bring some new insight into hadron - hadron interactions. In any case $\bar{Y}p$ reactions if they can be studied once will open a new field of physics, which may lead to a better understanding of annihilation phenomena.

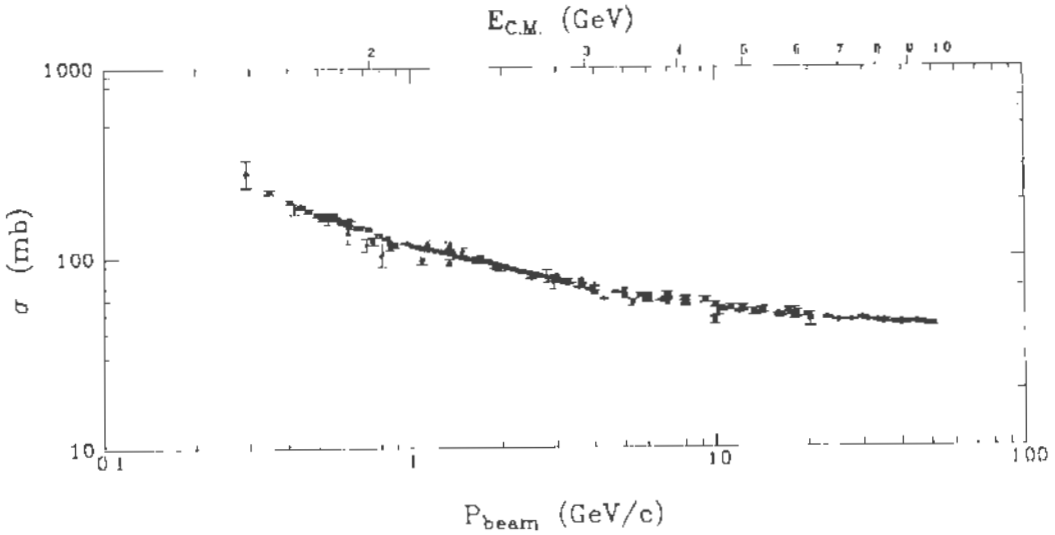

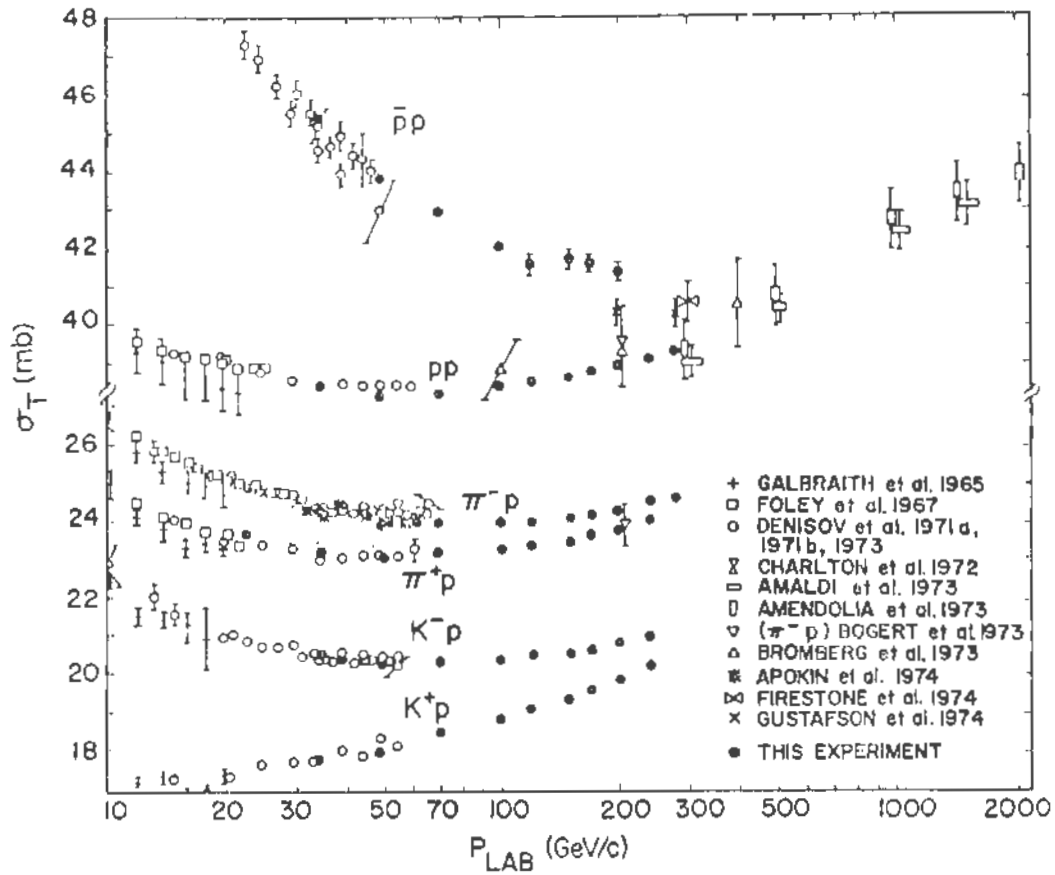

Figure 5.1

Total cross section on protons as a function of the incident laboratory momentum [Ref. (37) and (38)].

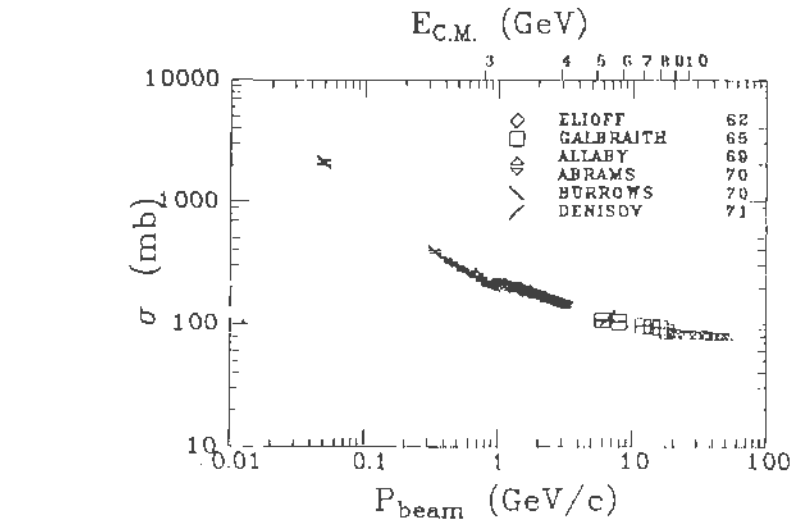

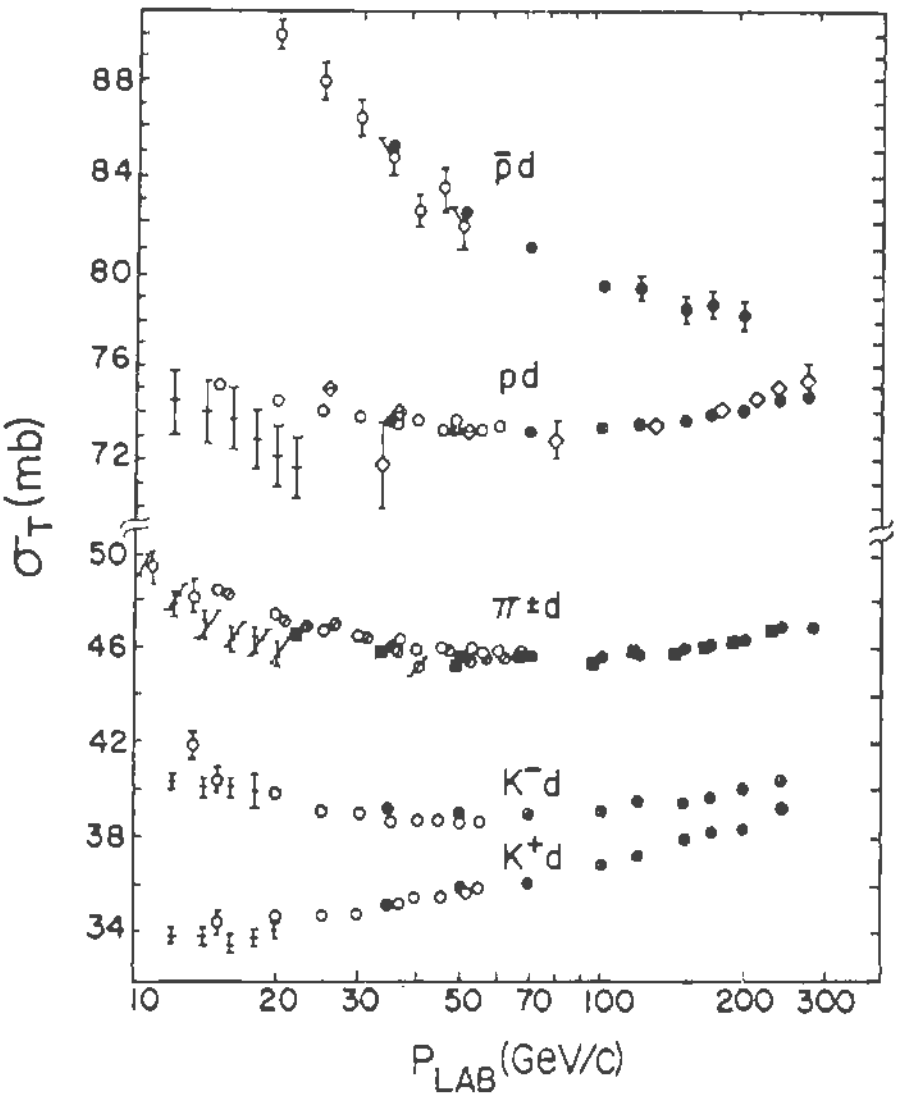

Figure 5.2

Total cross sections on deuterons as a function of the incident laboratory momentum [Ref. (37) and (38)].

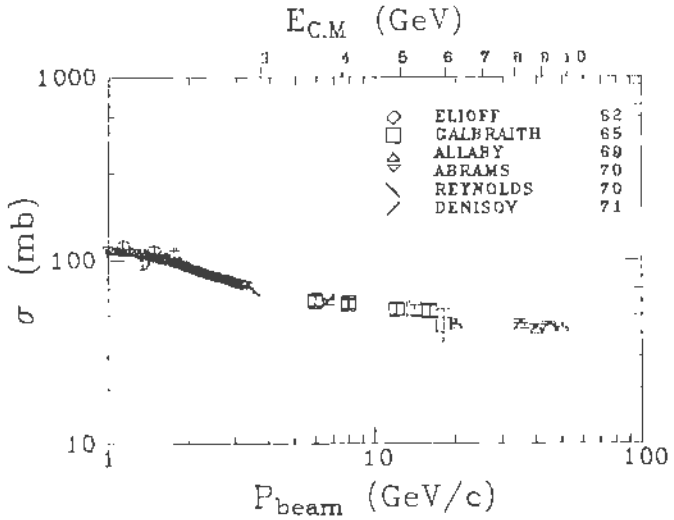

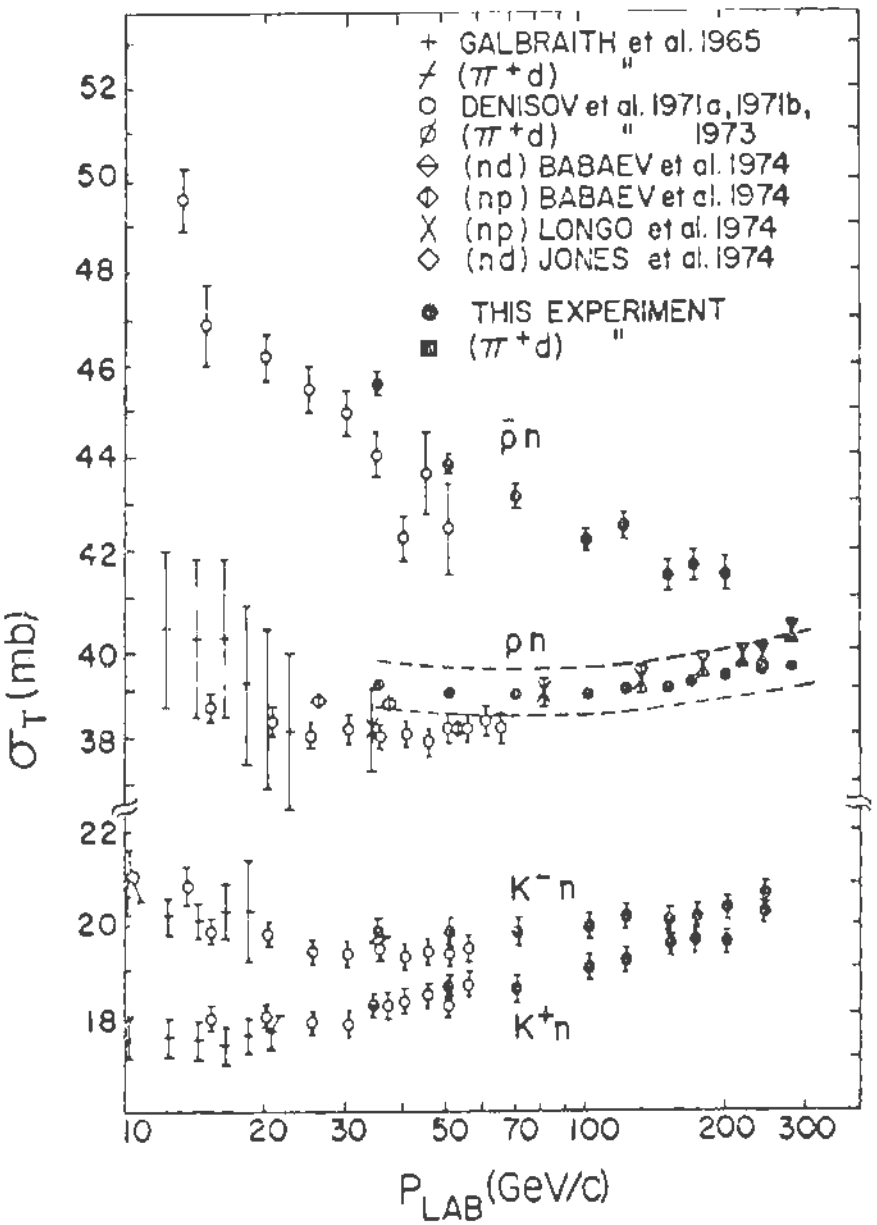

Figure 5.3

Total cross sections on proton as a function of the incident laboratory momentum (P_{lab} or P_{beam}) taken from reference (37) and (38).

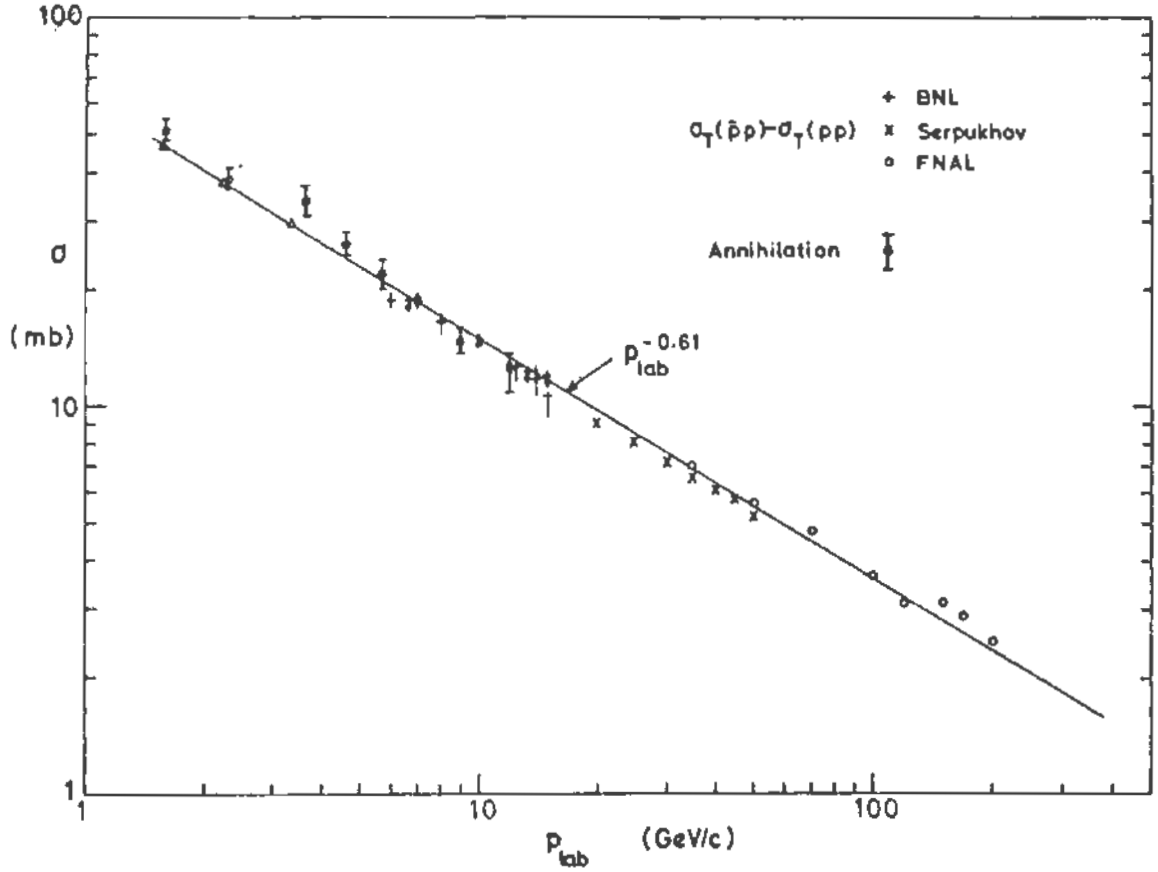

Figure 5.4

Distribution of the $\bar{p}p$ annihilation cross sections; together with the total cross section difference for $\bar{p}p$ and pp interactions as a function of the incident laboratory momentum.

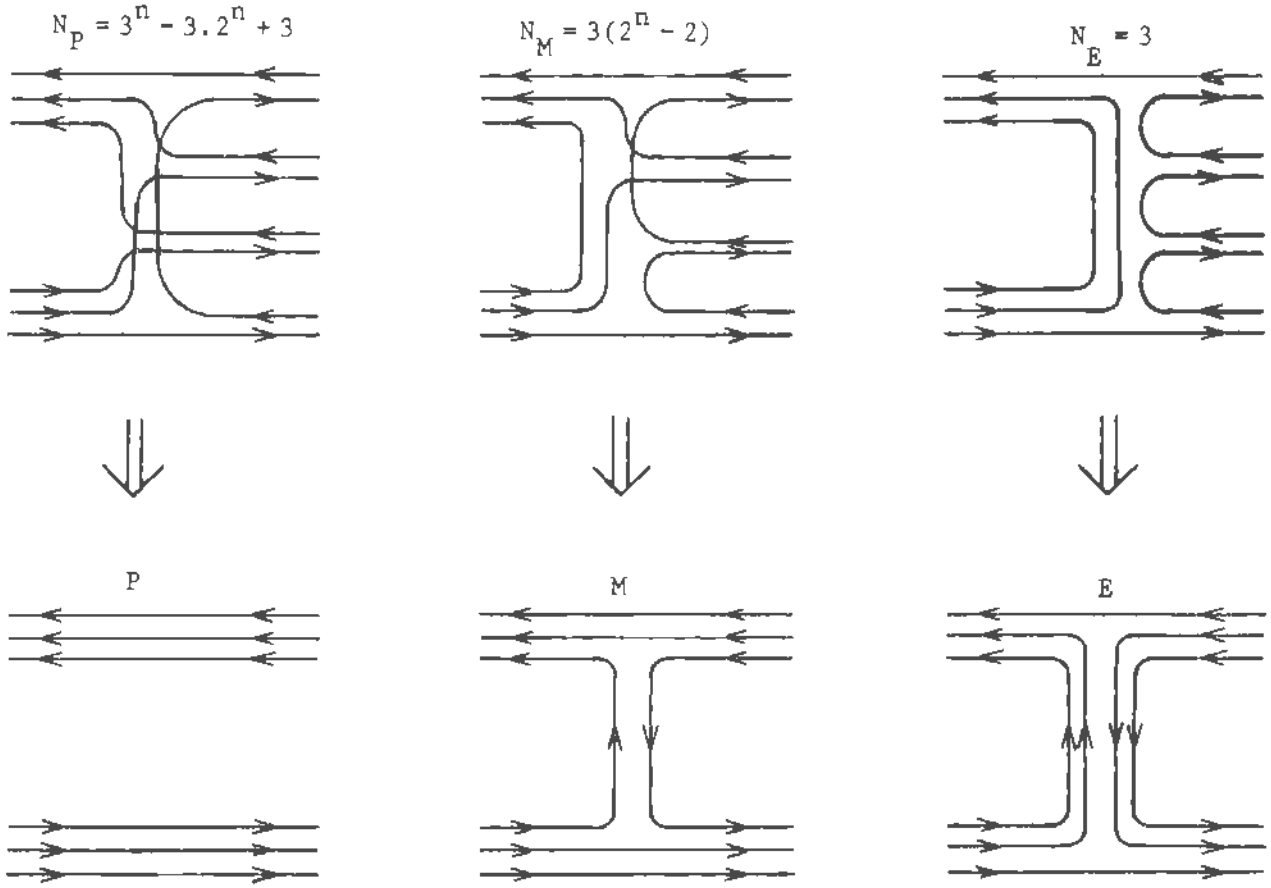

Figure 5.5

Examples of $\bar{p}p$ annihilation dual diagrams (top) leading to four mesons ($n = 4$) in the final state with their corresponding contributions to the $\bar{p}p \to \bar{p}p$ scattering. Here N_P, N_M and N_E are the number of dual diagrams contributing via unitarity to Pomeron (P), meson (M) and exotic (E) exchange in the $\bar{p}p \to \bar{p}p$ elastic scattering (Ref.42).

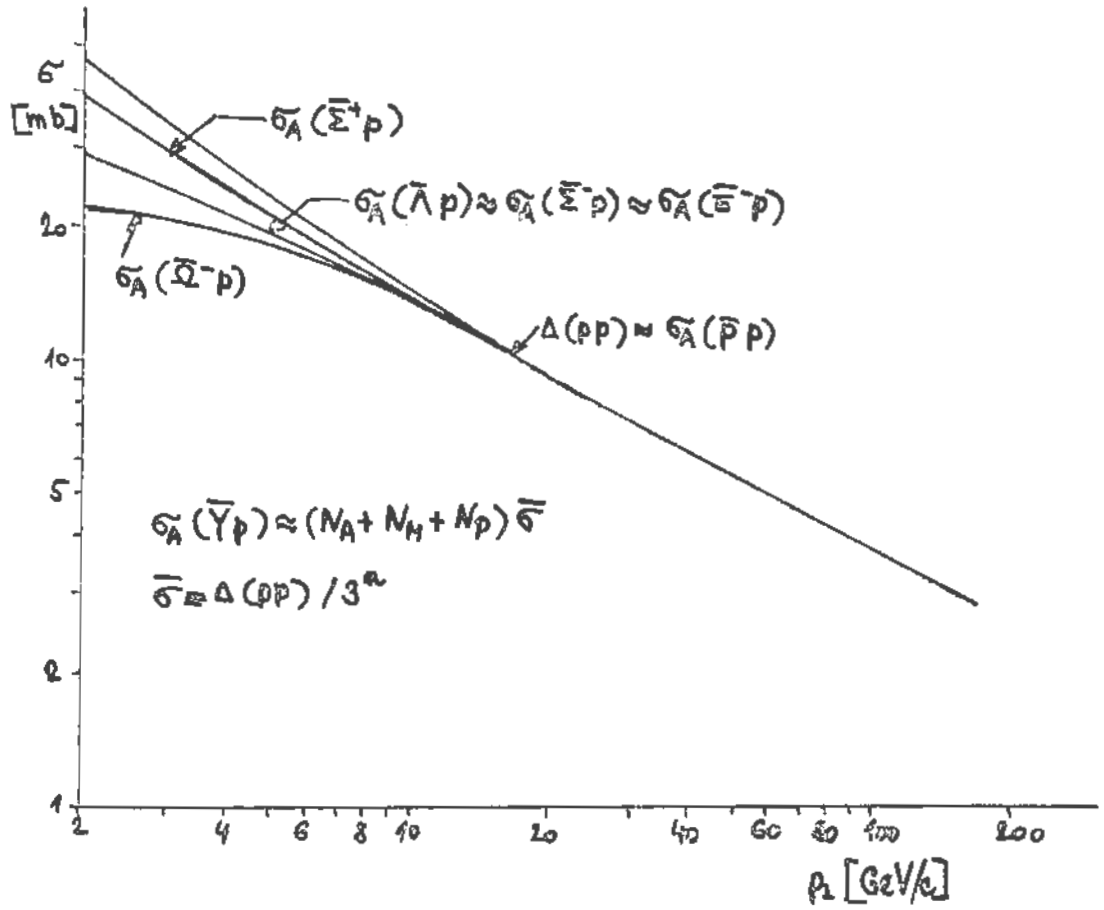

Figure 5.6

Distribution of the $\bar{Y}$-p annihilation total cross section as a function of the incident momentum according to the dual model mentioned in the text (from Reference 43).

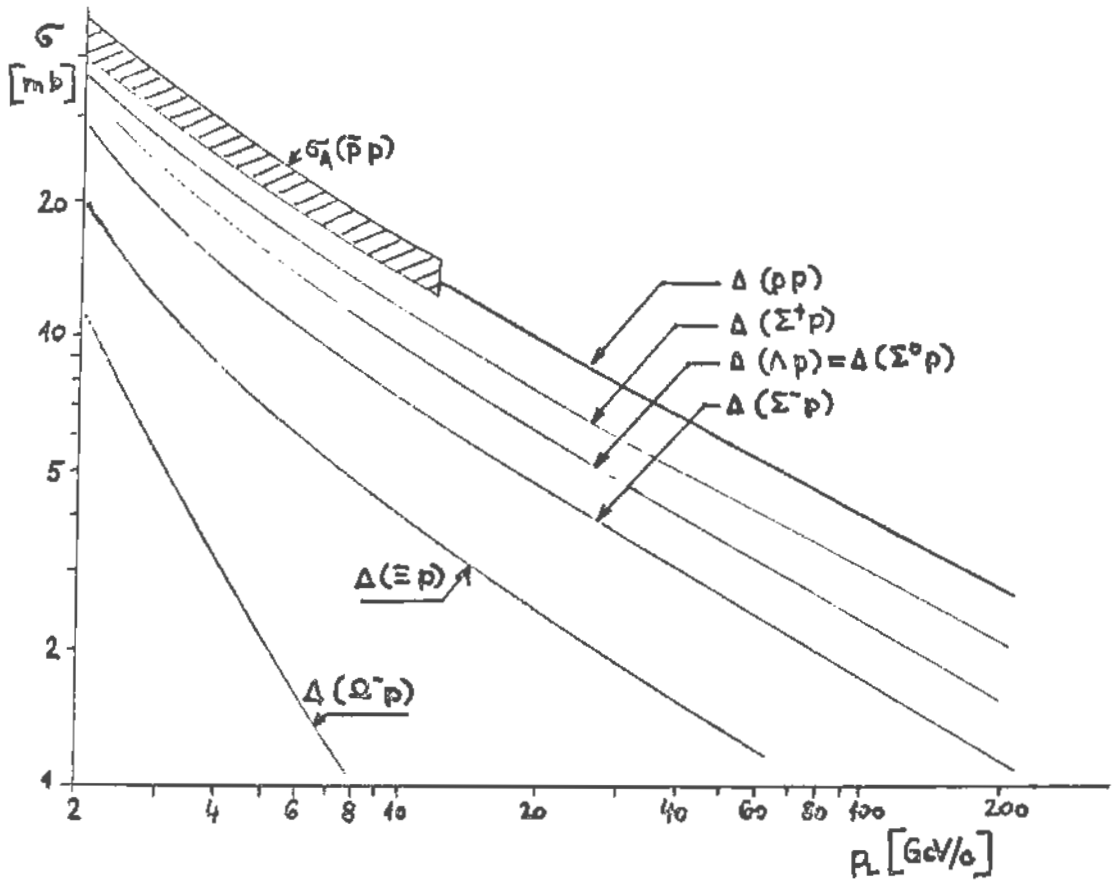

Figure 5.7

Distributions of the difference (Δ) in antiparticle-particle cross-section on hydrogen as a function of the incident momentum. The distribution are obtained from the additive quark model and are supposed to give the $\overline{Y}$-p annihilation cross section [Ref.43].

6. MULTIPLICITIES

6.1 - Statistical moments

The variables to which one has easy access in high-energy reactions are those which are built up from the charged multiplicity distributions. This kind of information is very simple to obtain and explains therefore why study of multiplicity distributions is so popular. We will discuss here the multiplicity distributions obtained from reactions induced by $\bar{p}$ and we will compare them with those obtained in other types of hadron - hadron interactions.

Before doing this, let us remember the most commonly used quantities in the study of charged multiplicity distributions[44]. They are: the mean multiplicity $\langle n \rangle$, the fluctuation $D = [\langle n^2 \rangle - \langle n \rangle^2]^{1/2}$ around the mean, the reduced moments $c_q = \langle n^q \rangle / \langle n \rangle^q$ (q being a positive number), and the Mueller correlation parameter $f_2 = \langle n(n-1) \rangle - \langle n \rangle^2 \equiv D^2 - \langle n \rangle$. Here n denotes the number of charged particles observed in a given type of collision. In the following we will also use σ_n and σ_{in} to denote the n charged particle cross-section and the inelastic cross-section, respectively.

The interest of the c_q moments is that in the case of KNO scaling [namely the quantity $\langle n \rangle \sigma_n / \sigma_{in}$ depending only on $n/\langle n \rangle$] they should be independent of S for large S. Then one has as immediate consequence that $D \sim \langle n \rangle$ and $f_2 \sim \langle n \rangle^2$. The f_2 parameter gives information about the correlation between the outgoing particles. If the charged particles are emitted independently from one another and according to a Poisson law one has $f_2 = 0$. The departure of zero indicates thus the degree of correlation between the emitted particles. In fact, f_2 is defined as the integral of the two-particle correlation function. This function defined for convenience in rapidity space is written as

$$C_2(y_1,y_2) = \rho_2(y_1,y_2) - \rho_1(y_1)\rho_1(y_2)$$

The indices 1 and 2 label the particles entering in the studied pairs. The $\rho_2(y_1,y_2)$ term represents the double density distribution of the particles, each having the rapidity y_1 and y_2, while $\rho_1(y_{1,2})$ are the single density distributions. In the absence of correlation, $\rho_2(y_1,y_2)$ is expected to factorize, i.e. $\rho_2(y_1,y_2) \propto \rho_1(y_1)\rho_1(y_2)$. Using property normalized densities[44] one obtains that no correlation leads to $C_2(y_1,y_2) = 0$. By definition the f_2 parameter is the integral of the two-particle correlation function:

$$f_2 = \int C_2(y_1, y_2)\, dy_1\, dy_2 .$$

One thus get

$$f_2 = \langle n(n-1) \rangle - \langle n \rangle^2$$

if no distinction is made between the considered particles or

$$f_2 = \langle n_{c_1}\, n_{c_2} \rangle - \langle n_{c_1} \rangle \langle n_{c_2} \rangle$$

whenever correlation between particles of types c_1 and c_2 are studied. The variation of f_2 with the c.m. energy of the collision is a very good indication for the validity of phenomenological models. This is shown in Table 6.1 which indicates the trends for f_2 in the framework of several simple models[44].

6.2 - Experimental data

Let us now look into the data. Figure 6.1 presents a compilation of the average charged multiplicity $\langle n \rangle$ obtained in $\bar{p}N$ interactions as a function of P_{inc} whereas the dispersion D is displayed in Fig. 6.2 as a function of $\langle n \rangle$[45]. One first notices that the values obtained for $\bar{p}n$ interactions have larger errors than for $\bar{p}p$ ones. The reason is that there is an intrinsic difficulty in estimating the inelastic one-prong cross-section [σ_1] in $\bar{p}n$ interactions. This is because the spectator scheme cannot be applied easily to the break-up reaction (Section 2.3). The one cross-section is then calculated by a substraction procedure:

$$\sigma_1 = \sigma_t(\bar{p}n) - \sum_{i=3} \sigma_n - \sigma_{el}(\bar{p}n)$$

introducing large errors on σ_1 and hence on any quantity deduced from the charged multiplicity distribution [$\sigma_{el}(\bar{p}N)$ is the elastic $\bar{p}N$ cross-section]. Whenever the quantities are calculated from the data with $n \geq 3$ the errors becomes much smaller, as in the $\bar{p}p$ case (Fig.6.1.b and 6.2.b).

We also notice from Fig.6.1 that for a given P_{inc}, $\langle n \rangle$ is greater for $\bar{p}p$ than for $\bar{p}n$ interactions, but for fixed $\langle n \rangle$ one has $D_{\bar{p}n} > D_{\bar{p}p}$ [In the following we will also us the notation D_{ab} and $\langle n_{ab} \rangle$, indicating that these quantities are obtained from a b collisions]. Similarly to pp interactions $D_{\bar{p}p}$ can be related linearly to $\langle n \rangle$. A best fit to the $\bar{p}p$ data shown in Fig.6.2a yields[45]

TABLE 6.1 - Trends for the f_2 Mueller parameters in the framework of simple phenomenological models. One always assumes that $\langle n \rangle \propto \ell n S$ [see for instance Ref.(44)]

$f_2 < 0$	Influence of the energy momentum conservation constraint for $\sqrt{S} \leqslant 6$ GeV.
$f_2 = 0$	Poisson distribution for the emitted particles
$\bar{f}_2 = 0$	Multi-Regge model calculated from the $n_t - 2$ produced particles, n_t being here the total number of particles including neutral.
$f_2 = (C_2 - 1)\langle n \rangle^2 - \langle n \rangle$ $\sim (\ell n S)^2$	KNO for which $c_q = \langle n^q \rangle / \langle n \rangle^q$ is independent of $\sqrt{S}$.
$f_2 = \frac{\langle K(K-1) \rangle}{\langle K \rangle} \langle n \rangle$	Independent cluster model, the cluster being produced according to a Poisson law. Here K is the number of particles coming from one cluster.
$f_2 \propto \langle n \rangle$ $\propto \ell n S$	Short-range order where $C_2(y_1,y_2) \approx \exp[-\lvert y_1 - y_2 \rvert / L]$, L being the correlation length, hence $f_2 = \int C(y_1,y_2) dy_1 dy_2 \sim \ell n S$.
$f_2 \propto \sqrt{S}$	Diffraction dissociation models.

$$D_{\bar{p}p} = (0.44 \pm 0.02)\langle n \rangle + (0.27 \pm 0.05),$$

which can be compared with

$$D_{pp} = (0.58 \pm 0.02)\langle n \rangle - (0.58 \pm 0.02)$$

for pp data[46].

This means that in the $\langle n \rangle$ range for which $\bar{p}N$ data exist, one has for a given $\langle n \rangle$, $D_{\bar{p}n} > D_{\bar{p}p} > D_{pp}$. This already shows that plotted in the KNO form, the $\bar{p}n$, $\bar{p}p$ and pp data will be distributed on different curves as shown in Fig.6.3. Indeed as already mentioned above, KNO scaling is equivalent for large S to the statement that the reduced c_q moments should be independent of S and therefore $D = \langle n \rangle \sqrt{C_2 - 1} \propto \langle n \rangle$. As this relation is not fulfilled by the data and because for fixed $\langle n \rangle$ the dispersions present great differences for $\bar{p}n$, $\bar{p}p$ and pp interactions, the three pieces of data cannot be distributed on the same curves, as indeed seen in Fig. 6.3. One can notice that if one would like to obtain the linear relation $D = K[\langle n \rangle - \alpha]$, K and α being constants for a given type of collision there are the moments $\bar{c}_q = \langle (n-\alpha)^q \rangle / \langle (n-\alpha) \rangle^q$ which should be independent of S[47]. At the present level of statistics for the $\bar{p}N$ data it is difficult to know which of the c_q or $\bar{c}_q$ moments tend to be really independent of S.

Let us now turn to multiplicity distribution obtained from annihilation reactions. We will still assume that in the region where there is no annihilation data ($P_{inc} > 12$ GeV/c) the total and topological $\bar{p}p$ annihilation cross-sections can be obtained by making differences between $\bar{p}p$ and pp cross-sections. Figure 6.4 presents the average of the negatively charged particles $\langle n_- \rangle$ as a function of S for annihilation and pp interactions. The variation of the Mueller parameter for the negatively charged particles $f_2^{--} = \langle n_-(n_- - 1) \rangle - \langle n_- \rangle^2$ versus $\langle n_- \rangle$ is also very different for both processes (Note that $f_2^{--} = f_2/4 - \langle n_- \rangle/2 + Q/4$, Q being the total charge of the initial state.) The strong decreasing behaviour for f_2^{--} can be partly reproduced by assuming that the charged particles are emitted in annihilations according to a Poisson law. Then one has $f_2 = 0$, leading to $f_2^{--} = -0.5\langle n_- \rangle$. It is interesting to note that the description of f_2^{--} versus $\langle n_- \rangle$ becomes worse if one assumes that both positive and negative particles are separately emitted according to Poisson laws (dashed line of Fig.6.4b), taking into account the overall charge-conservation constraint[41]. A better description of the $f_2^{--}, \langle n_- \rangle$ plot is obtained by assuming that a single cluster or fireball is formed during the annihilation processes, which then subsequently decays through a linear statistical decay chain[48] [$f_2 = -0.73 \langle n_- \rangle$]. These models, giving a linear relation between f_2^{--} and $\langle n_- \rangle$, fail to explain the $\langle n_- \rangle \gg 3$ region. The departure of the straight line in this region has been explained in the framework of multiperipheral dual models[49]. In this approach the change in the variation of f_2^{--} results from a change in the régime of cluster production, namely from a single to multicluster production.

The striking differences mentioned, observed between $\bar{p}p$ annihilations and pp interactions, can also be seen by plotting these data in the KNO form[40] (Fig.6.5). One clearly sees that the $n_a/\langle n_a \rangle$ has a smaller dispersion than the $n_{pp}/\langle n_{pp} \rangle$, i.e.

$$\frac{D_a}{\langle n_a \rangle} < \frac{D_{pp}}{\langle n_{pp} \rangle},$$

the indice a denoting the annihilation. It has been proposed[50] to compare pp and annihilation data at the same available energy. This can be done in several ways. Let us examine here one possible method. Since in annihilation reactions the colliding baryons disappear, the same available energy will approximately be obtained whenever the c.m. energy in pp collision ($\sqrt{S'}$) is related to that in annihilation reaction ($\sqrt{S}$) by $\sqrt{S'} = \sqrt{S} + 2m_p$ (m_p being the nucleon mass). But in pp interactions the leading protons take on an average one half of the c.m. energy and there is an average number of 1.4 proton in the final state (we will come back to the determination of this number). Then it can be conceived that one possible way to make a comparison is to consider the $\langle n_a(S) \rangle$ and $\langle n_{pp}(4S') - 1.4 \rangle$ quantities. As can be seen from Fig.6.4a it turns out that these quantities are nearly equal for $P_{inc} \lesssim 20\,\text{GeV/c}$[41]. Of course the 1.4 number is some kind of average number and can be a function of S. It was measured at 19 GeV/c[51] [~1.4] and also at 200 GeV/c[52] [1.12 ± 0.32]. In any case, Fig.6.4b confirms clearly that in the first approximation the average number of emitted charged particles depends mainly on the available c.m. energy and not on the quantum numbers of the colliding particles. The situation is different for the other statistical moments as for all the actual data one has[41]:

$$\frac{D_a(S)}{\langle n_a(S) \rangle} < \frac{D_{pp}}{\langle n_{pp} \rangle - 1} \simeq 0.58$$

or

$$\frac{D_a(S)}{\langle n_a(S) \rangle} < \frac{D_{pp}(4S')}{\langle n_{pp}(4S') - 1.4 \rangle} \simeq 0.58 + \frac{0.23}{\langle n_{pp}(4S') - 1.4 \rangle}.$$

The fact that the distribution of the $(n_{pp} - 1)/\langle n_{pp} - 1 \rangle$ or $\langle n_{pp} - 1.4 \rangle / \langle n_{pp} - 1.4 \rangle$ variables is larger than obtained for the annihilations using the $n_a/\langle n_a \rangle$ variable can be explained in the framework of the geometrical model[53]. Indeed in this approach the average number of produced particles is largest for near - zero

impact parameter collisions. At each impact parameter one can associate multiplicity distributions, the average of which depends on the impact parameter. As $\bar{p}p$ annihilation occurs through central collisions[50,54] (see also Section 7.2) many more multiplicity distributions are summed up in pp collisions than in $\bar{p}p$ annihilations. This leads to a broader multiplicity distribution in the pp case than in annihilation at the same available energy.

Let us now come back to the way that the average number of protons in the final state is evaluated in pp collisions. At 19 GeV/c this average has been measured by identifying the outgoing particles. At higher energies the identification of particles presents difficulties. Therefore the average at 200 GeV/c has been determined by comparing average charged multiplicities obtained from pp and pn interactions at the same c.m. energy[52]. To this end, we draw in Fig.6.6 production diagrams for pp and pn interactions without specifying what are the objects exchanged in the t-channel. At each nucleon vertex the incident proton (neutron) can transform itself into a neutron (proton) or remains unchanged. Defining α as being the fractional rate of charge exchange at a nucleon vertex (α = ratio of the cross-section of charge exchange $p \leftrightarrow n$ to the cross-section for producing particles at the nucleon vertex), the average number of outgoing protons in pp collisions is simply $2(1-\alpha)$. A simple calculation shows (see Fig.6.6) that α can be determined from the relation $\langle n_{pn} \rangle - \langle n_{pp} \rangle = 1 - 2\alpha$. At 200 GeV/c one thus obtains an average number of protons of 1.12 ± 0.32, which is compatible with the 1.4 value taken above.

Attempts have also been made to compare $\bar{p}p$ with e^+e^- annihilations[55]. Of course both processes are different at least because the e^+e^- is mainly coupled to one photon, i.e. to a state of spin (J) and parity (P) $J^P = 1^-$. One sees, however, from Fig.6.7 that the average charged multiplicities for both processes, plotted as a function of the c.m. energy, tend to cluster on the same distribution. Finally, let us also mention a work[56] suggesting that it is the quark-antiquark interaction which should be compared with e^+e^- annihilation. As illustrated in Fig.6.8 the three possible diagrams shown there lead to different relations between $\bar{p}p$ and e^+e^- multiplicities. The graphs have a different S dependence so that at high energy the annihilation of three $\bar{q}q$ should predominate. In this region at least $\bar{p}p$ cannot be compared directly with e^+e^-.

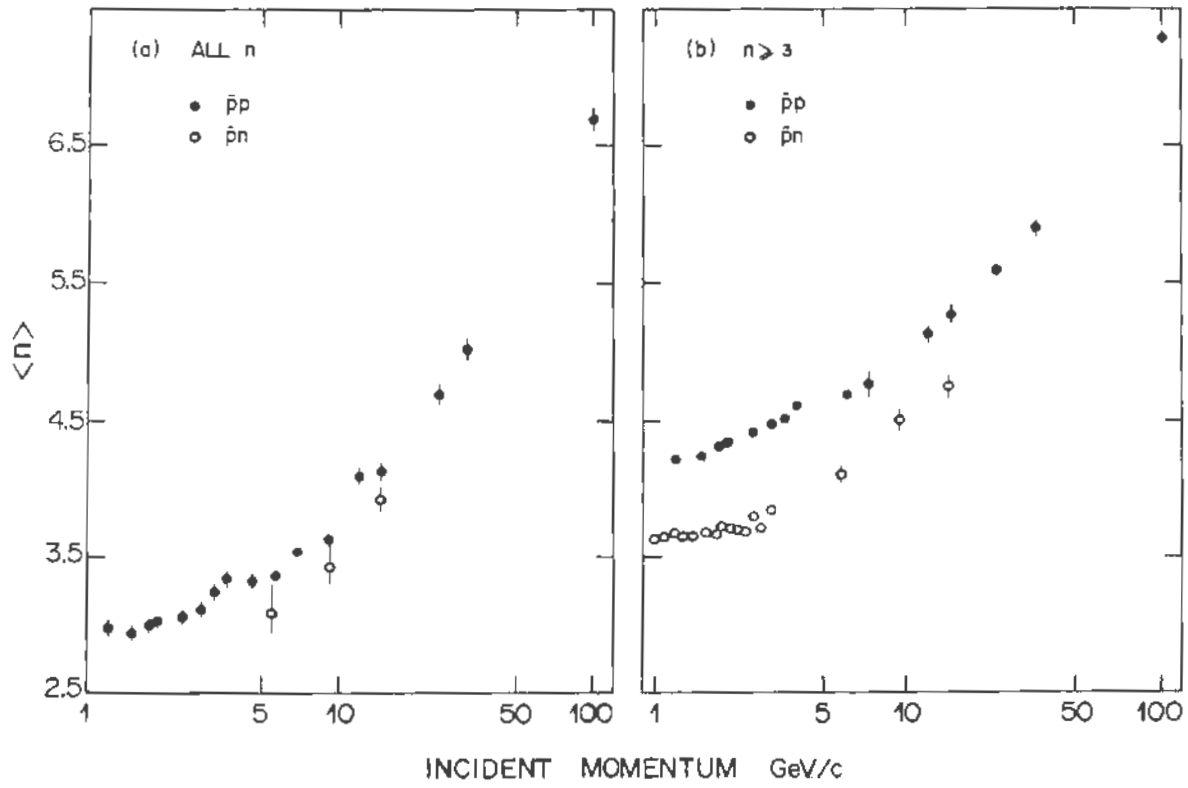

Figure 6.1

a). Comparison between the average multiplicity for $\bar{p}p$ and $\bar{p}n$ interactions

b). Same distributions as in (a) but obtained from multiplicity distributions when the number of charged particles is $n \geq 3$ [Ref. 45].

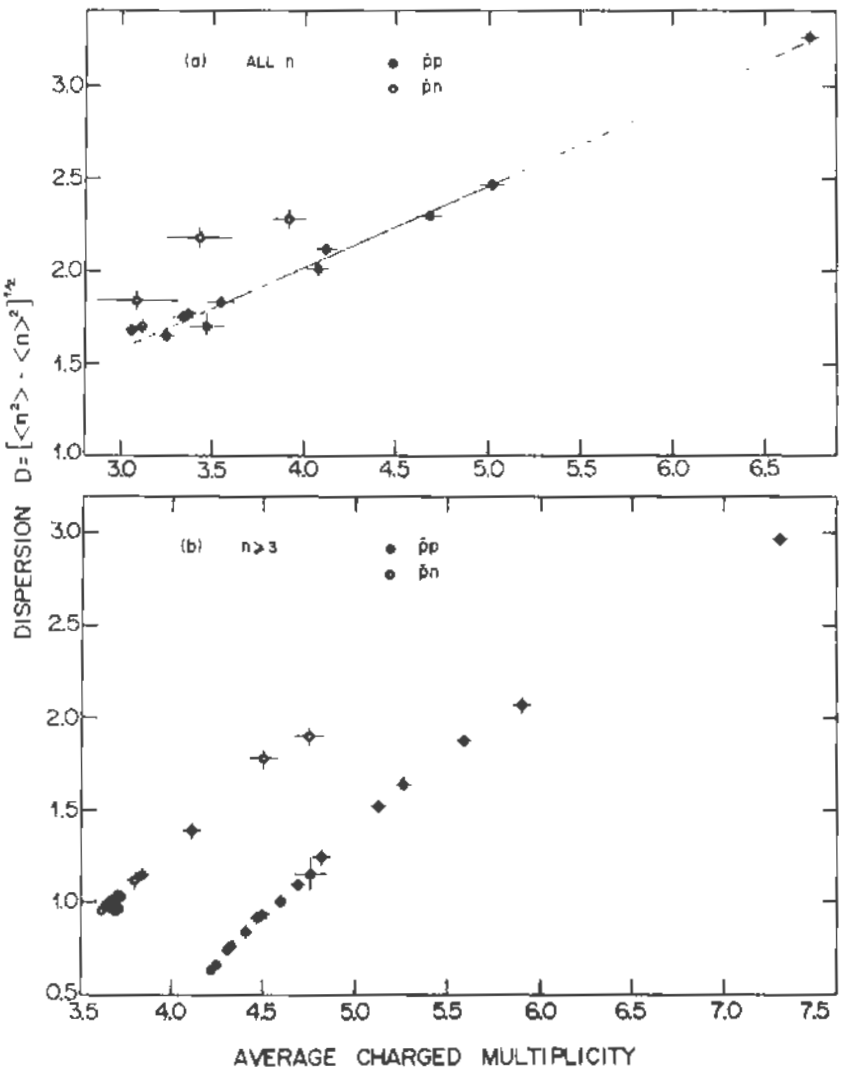

Figure 6.2

a): The dispersion D of the charged multiplicities versus its average $\langle n \rangle$ for $\bar{p}p$ and $\bar{p}n$ interactions. The full line represents a linear fit to the data in the $3.5 < \langle n \rangle < 5.5$ region. By including the 100 GeV/c point one obtains $D = (0.44 \pm 0.02)\langle n \rangle + (0.27 \pm 0.05)$

b). The same distributions as above but obtained from multiplicities with $n \geq 3$ [Ref. 45].

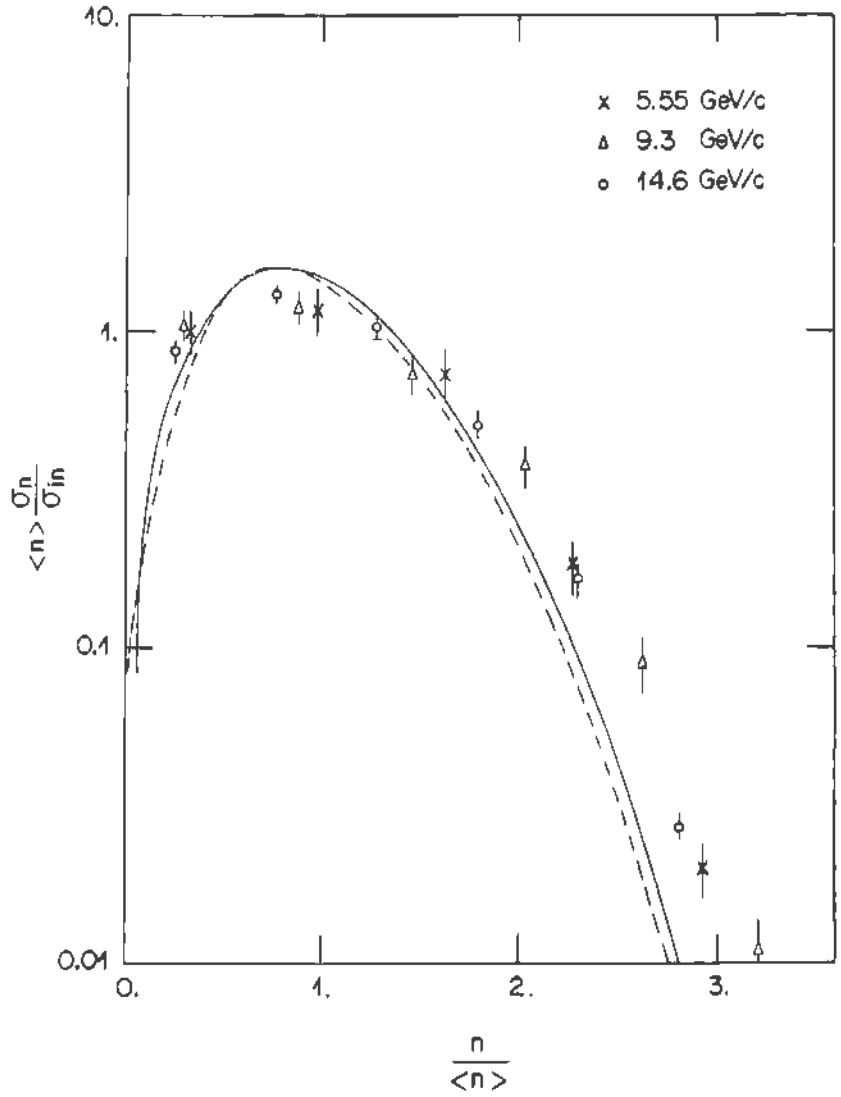

Figure 6.3

The distribution of $\langle n\rangle\sigma_n/\sigma_{in}$ versus $n/\langle n\rangle$ for $\bar{p}n$ interactions at 5.55, 9.3 and 14.6 GeV/c. The full and dashed lines are obtained from fits to pp and $\bar{p}p$ data, respectively [Ref.5].

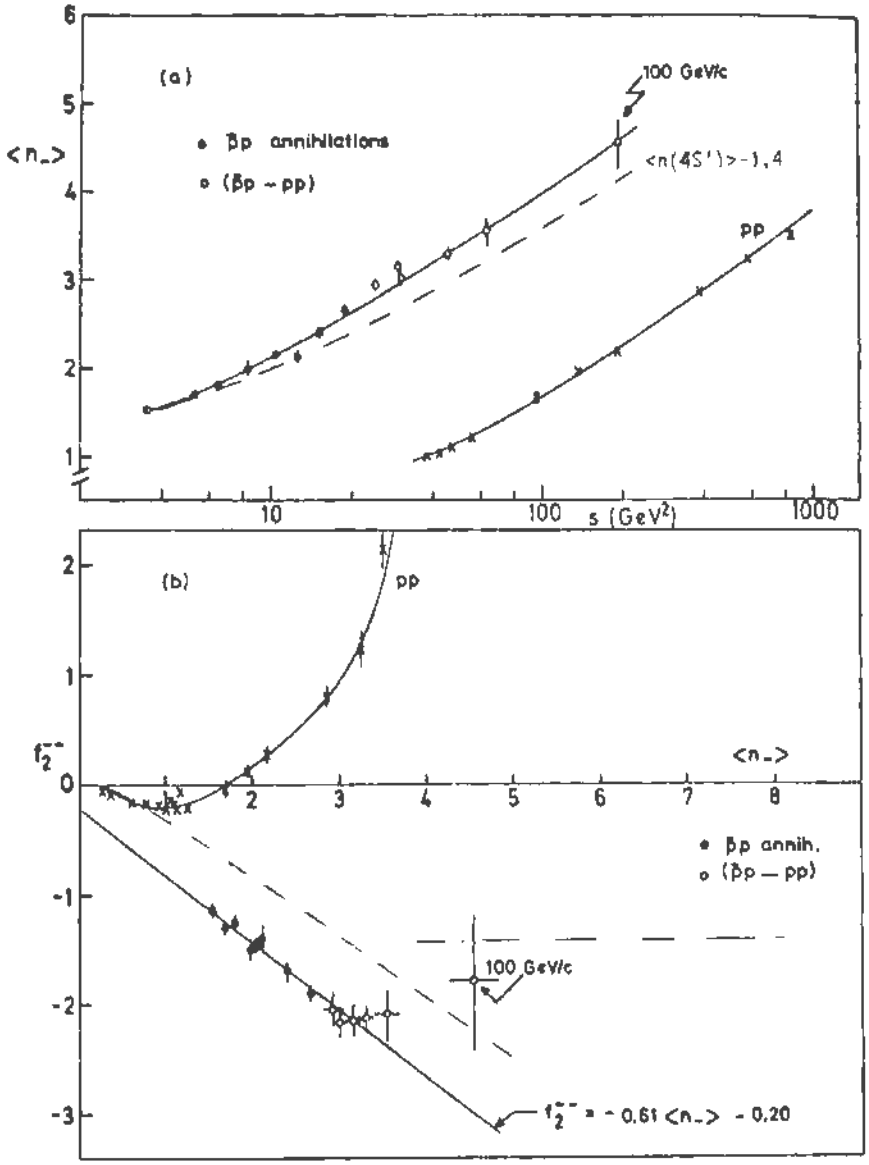

Figure 6.4

a). Distribution of the average negatively charged multiplicity $\langle n_- \rangle$ for $\bar{p}p$ annihilations and pp interactions as a function of S [Refs. 40 and 41]. The lines are drawn to guide the eye.

b). The $f_2^{--} = \langle n_-(n-1) \rangle - \langle n_- \rangle^2$ parameter for negatively charged particles as a function of $\langle n_- \rangle$ for $\bar{p}p$ annihilation and pp interactions. The dashed curves is obtained assuming that the negative and charged particles are emitted each according to a Poisson law with the constraint $\langle n_- \rangle = \langle n_+ \rangle$. The dot-dashed curve is the Webber prediction [Ref. 49].

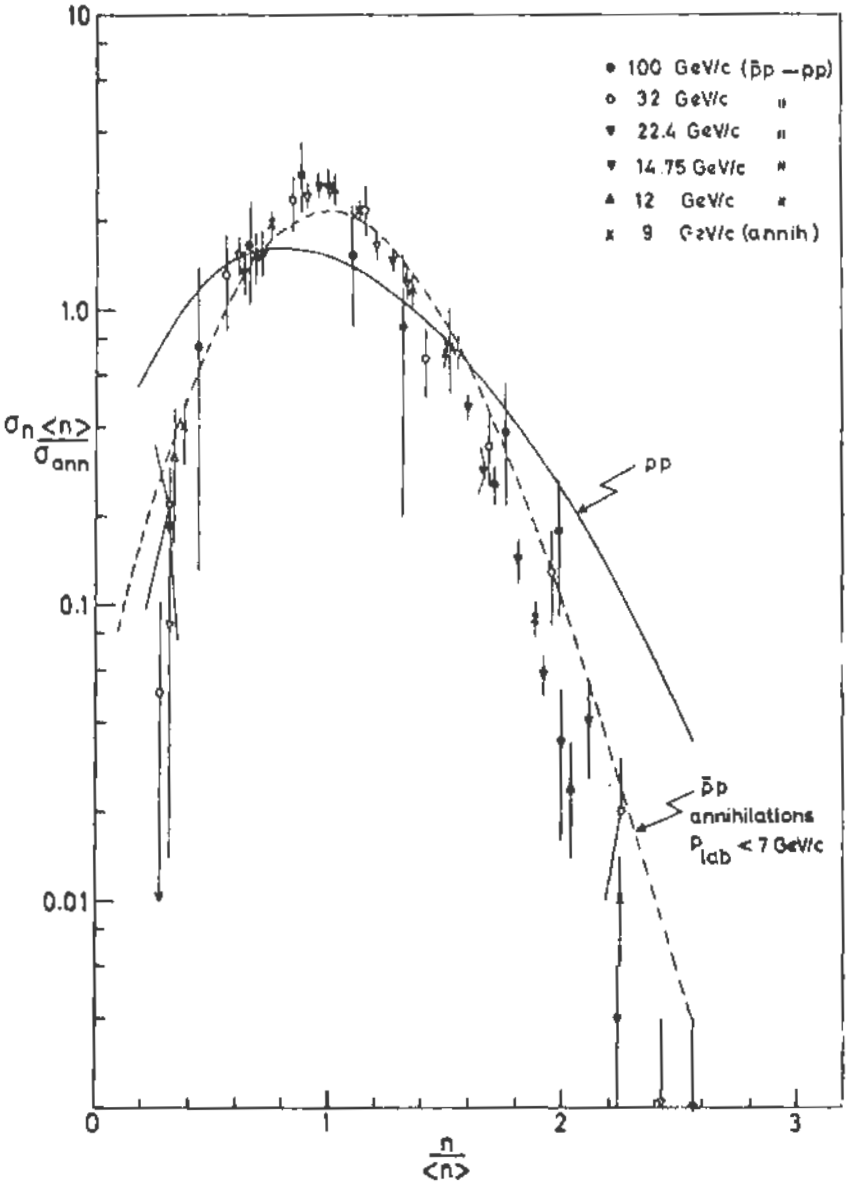

Figure 6.5

Distribution of $\langle n \rangle \sigma_n / \sigma_{ann.}$ versus $n/\langle n \rangle$ taken from Reference 40. Here σ_n represents the annihilation cross-section for n charged outgoing particles and $\sigma_{ann.}$ is the annihilation cross section (σ_a in the text).

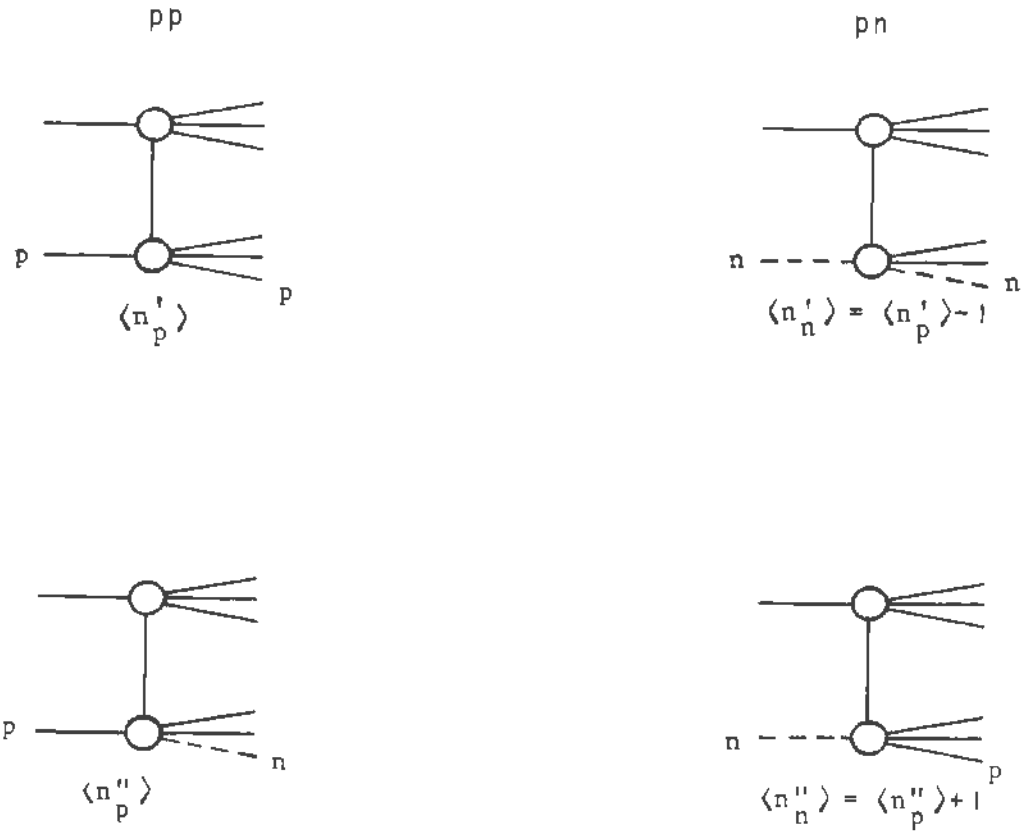

$$\langle n_p^{\ell} \rangle = \langle n'_p \rangle (1-\alpha) + \alpha \langle n''_p \rangle$$

$$\langle n_n^{\ell} \rangle = \langle n'_n \rangle (1-\alpha) + \alpha \langle n''_n \rangle$$

$$= [\langle n'_p \rangle - 1][1-\alpha] + \alpha[\langle n''_p \rangle + 1]$$

$$\langle n_p^{\ell} \rangle - \langle n_n^{\ell} \rangle = \langle n_{pp} \rangle - n_{pn} \rangle = 1 - 2\alpha$$

Figure 6.6

Diagrams vizualising pp and pn interactions. The average multiplicities with prime or double prime represent the multiplicity associated to the lower vertex, when the initial particle remains as it was or when a charge exchange occurs ($p \leftrightarrow n$), respectively. The total multiplicity due to the lower vertex is denoted by the superscript ℓ. Note that because the upper vertex are identical in pp and pn interactions one has $\langle n_p^{\ell} \rangle - \langle n_n^{\ell} \rangle = \langle n_{pp} \rangle - \langle n_{pn} \rangle$ allowing to determine α. Here α is the probability that a charge exchange occurs ($p \leftrightarrow n$) at a given vertex.

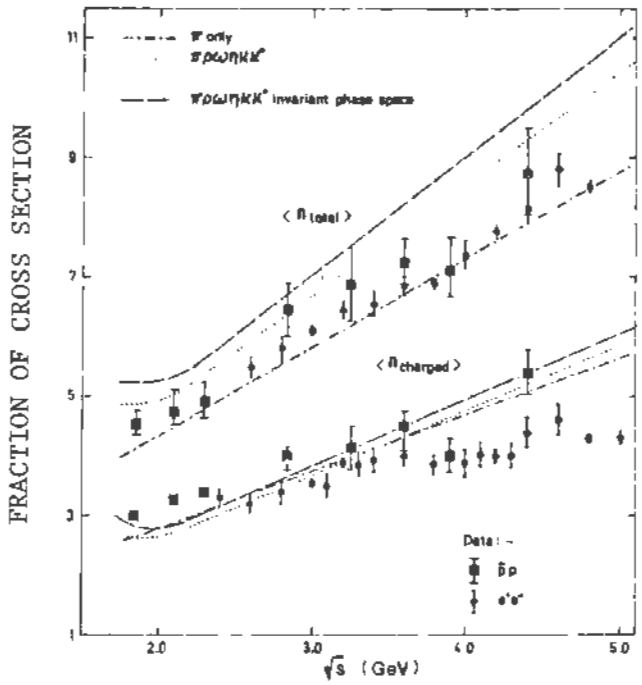

Figure 6.7

The charge average multiplicity for $\bar{p}p$ and e^+e^- annihilations as a function of $\sqrt{S}$. The curves are the predictions of the statistical model as used in Reference 55.

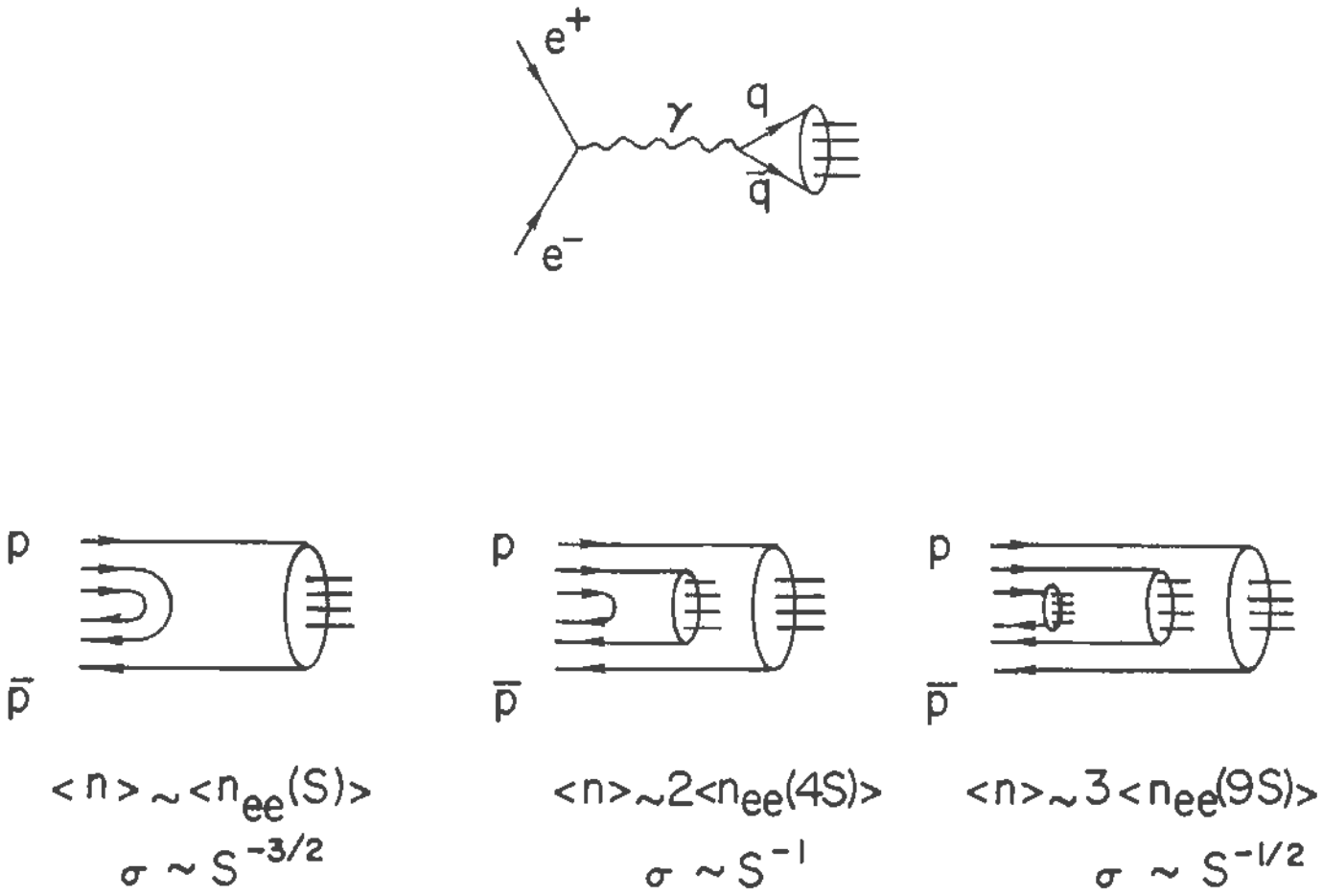

Figure 6.8

Comparison of diagrams leading to e^+e^- and $\bar{p}p$ annihilations. In this latter case, one has one, two or three quark - antiquark ($q\bar{q}$) pairs which are producing hadrons. The e^+e^- average charged multiplicity ($\langle n_{ee} \rangle$) at $\sqrt{S}$ is compared with that of $\bar{p}p$ ($\langle n \rangle$) at the same available energy for the $\bar{q}q$ pairs producing hadrons. Note the different S dependence of the cross sections (σ) corresponding to the different $\bar{p}p$ annihilation diagrams.

7. ANNIHILATION PROCESSES

7.1 - Introduction

Let us discuss some general features characterizing annihilation processes. As seen above, the annihilation component leads to events in which the number of emitted particles is large. For instance the average charged multiplicity for $\bar{p}p$ annihilation at 15 GeV/c is approximatively as large as that obtained in pp collisions at 100 GeV/c [$\langle n \rangle \approx 6$]. Therefore, for many years $\bar{p}$ annihilation physics has been faced with the same problems one has now in studying hadron - hadron collisions at very high energies ($\sqrt{S} \gtrsim 15$ GeV), i.e. how to extract from a flood of information that part which is essential for understanding multiparticle production phenomena.

Up to now there exists real information about annihilations only for $P_{inc} \leq 12$ GeV/c, as one has there exclusive annihilation channels. Above 12 GeV/c knowledge about annihilation is obtained by making differences between $\bar{p}p$ and pp data with all the uncertainties introduced by this procedure. An annihilation event is usually defined as a final state without baryons. When the c.m. energy increases, the $\bar{N}N$ pair production may become important complicating thus the identification of annihilation events. It is likely although not sure that $\bar{N}N$ pairs will be produced centrally, the two particles being close in rapidity (see below). Therefore the presence of leading particles can help to sign a non annihilation event. In any case, for $P_{inc} \leq 12$ GeV/c there is no difficulty in identifying by the usual method (no baryons in the final state) annihilation reactions as the $\bar{N}N$ production cross section is negligible (of the order of a tens of nb as shown by recent Ω experiments, see also Section 3.4).

Let us now discuss some specific aspects of the annihilation channels for $P_{inc} \leq 12$ GeV/c. One characteristic of these processes is that many resonances are produced in the final state. In the following we will ignore this resonance production but examine some more general features such as cross-section, peripherality and two-particle correlation behaviour.

7.2 - General features

Concerning $\bar{p}p$ or $\bar{p}n$ exclusive annihilation channels, one observes for a given $\sqrt{S}$ a fluctuation of these cross-sections whenever they are plotted as a function of the total number of outgoing pions (charged plus neutral). This is

illustrated by an example shown in Fig.7.1 which presents the $\bar{p}p$ (5.7 GeV/c) and $\bar{p}n$ (5.55 GeV/c) exclusive annihilation cross-sections at nearly the same incident momentum[54]. One sees from this figure that the $\bar{p}p$ and $\bar{p}n$ data are distributed on two smoth curves characterized by the presence or absence of a π^o in the final state. As the π^o appears in $\bar{p}p$ ($\bar{p}n$) channels for an odd (even) number of produced pions, the observed fluctuation is not due to a G-parity effect. In fact, multiperipheral models can give an intuitive explanation of this fluctuation. In these models one assumes that it is the nucleon trajectory which gives the dominant contribution to annihilation reactions. Then the positive and negative charge of the outgoing pions has to alternate along the multiperipheral as shown in Fig.7.2. A π^o however can be placed everywhere along the chain. One can then conceive that as a consequence of this freedom the cross-section tends to increase when a π^o is present in the final state. In any case, by comparing the cross-section of $\bar{p}p$ and $\bar{p}n$ channels with the same number of outgoing pions the channel with a π^o has always the bigger cross-section.

A feature which also characterizes the annihilation reactions is that they appear to be produced more centrally than usual production reactions. In other words the transverse momenta of the secondaries do not present the strong limiting behaviour seen elsewhere. This is shown by the example of Fig.7.3, which presents the average transverse momenta $\langle r \rangle$ of the outgoing pions versus the average of their absolute c.m. longitudinal momenta for $\bar{p}n$ annihilations at 5.55 GeV/c[54]. One sees that $\langle r \rangle$ is not so small as for non-annihilation channels [$\langle r \rangle \sim 300$ MeV/c] and that the data are approaching phase space when the number of produced pions increases. That annihilation reactions occur through central collisions has already been mentioned in the discussion about multiplicity distributions (Section 6.2). Other methods are also used in order to investigate the peripheral nature of the reactions. Let us only mention here that it becomes rather popular to analyse the peripherality of events by means of the lower limit of the root mean square impact parameter[57].

Much effort has been devoted to the study of two particle correlation in annihilation channels. Because of the numerous produced pions it was suggested to use annihilation reactions to search for the influence of the Bose-Einstein statistics among the outgoing particles. The study of the c.m. opening angle between two pions showed that differences appear for like ($\pi^{\pm}\pi^{\pm}$) and unlike ($\pi^+\pi^-$, $\pi^{\pm}\pi^o$) pairs. This so-called Goldhaber effect is generally explained in terms of the Bose-Einstein statistics.

There are, of course, other methods utilized for studying correlation between produced particles. Let us immediately point out that the two-particle correlation function, as defined in Section 6.1, is not very useful. At low $\sqrt{s}$ the behaviour of a correlation function reflects mainly the energy-momentum constraint whatever kinematical variables one chosen[58]. Other methods are based on the observation that the average transverse momentum of the secondaries is limited to a few hundred MeV/c, although this effect is not so marked for annihilations. Thus increase of the c.m. energy leads primarily to an increase of the longitudinal momenta of the outgoing particles. It might then be conceivable that one can learn about production mechanism by studying the longitudinal momentum configuration of an event (using the longitudinal phase-space plot or for instance correlation in the longitudinal momentum space). Alternatively, another point of view is to consider correlation effects in the transverse plane (the plane perpendicular to the c.m. beam momentum), precisely because of the similarity of the transverse momentum distributions. Then correlation study will perhaps allow to stress the influence of the type of the colliding particles. Moreover, comparison between various reactions at different energies can be carried out. We take the latter attitude and we will discuss here a method of studying two-particle correlation in the transverse plane[58,59]. Although the method described below is based on a rather phenomenological approach, it has the merit of allowing the measurement of the correlation via a single parameter.

To this end, we consider the variables $\vec{P}_{\pm} = \vec{r}_1 \pm \vec{r}_2$ (modulus $P_{\pm}$), $\vec{r}_1$ and $\vec{r}_2$ being the transverse momenta (modulus $r_{1,2}$) of the particles entering in given studied pairs. Whenever the distributions of $\vec{P}_+$ and $\vec{P}_-$ are different, a correlation between $\vec{r}_1$ and $\vec{r}_2$ must be present. An analysis of $\bar{p}p$ data at 5.7 GeV/c[59] has shown that the P_+^2 distributions for like and unlike pairs have exponential shapes (see Fig.7.4), i.e. $dN/dP_{\pm}^2 \propto \exp[-A_+ P_{\pm}^2]$. Furthermore the single transverse momentum distributions ($dN/dr_{1,2}^2$) can also be approximated by exponential functions $dN/dr_{1,2}^2 \propto \exp[-A_{1,2}\, r_{1,2}^2]$ as shown in Fig.7.5. This approximation is less valid for small $r_{1,2}^2$, as one observes there a small excess of particles due mainly to resonance production. In order to reproduce these exponential shapes one can make the assumption that the two-particle density distribution in the transverse plane is given by:

$$\frac{dN}{d\vec{r}_1 d\vec{r}_2} \propto \exp[-a_1 r_1^2 - a_2 r_2^2 - b\,\vec{r}_1\vec{r}_2]$$

Here a_1, a_2 and b are constants depending on the reaction and on the type of studied pairs. Such a density introduces the correlation between $\vec{r}_1$ and $\vec{r}_2$ via the $b\vec{r}_1\vec{r}_2$ term. Thus the magnitude of b can serve as a measure of the two particle correlation in the transverse plane.

Let us now show that the above density leads to exponential distributions in the $P_\pm^2$ and $r_{1,2}^2$ variables. Using polar coordinates in the transverse plane the integration over angles of the chosen density yields ;

$$\frac{dN}{dr_1^2\, dr_2^2} \sim \exp[-a_1 r_1^2 - a_2 r_2^2]\, J_0(i\, b\, r_1 r_2)$$

J_0 being the zeroth-order Bessel function. A further integration over r_1 or r_2 gives indeed the exponential function

$$\frac{dN}{dr_{1,2}^2} \propto \exp[-a_{1,2}(1 - \frac{b^2}{4a_1a_2})r_{1,2}^2] \equiv \exp(-A_{1,2}\, r_{1,2}^2)$$

As one has

$$\frac{dN}{d\vec{P}_+\, d\vec{P}_-} = \frac{4\, dN}{d\vec{r}_1\, d\vec{r}_2}$$

one obtains in a similar way

$$\frac{dN}{dP_\pm^2} \propto \exp[-\alpha_{1,2}(1 - \frac{\beta^2}{4\alpha_1\alpha_2})P_\pm^2] \equiv \exp[-A_\pm P_\pm^2]$$

with

$$\alpha_{1,2} = (a_1 + a_2 \pm b)/4$$

$$\beta = (a_1 - a_2)/2$$

Thus if the expression chosen for $dN/(d\vec{r}_1 d\vec{r}_2)$ is really meaningfull the correlation between transverse momenta can be measured by the $|b|$ parameter. For $\bar{p}p$ annihilation C - invariance implies identical transverse momentum distributions for the π^+ and the π^-, hence $\beta = 0$. Then one has :

$$\frac{dN}{dP_\pm^2} \propto \exp[-\frac{2a_1 \pm b}{4} P_\pm^2]$$

The exponential slopes of the P_+^2 and P_-^2 distributions gives then immediately b. For other cases one can fit the data with the

$$\frac{dN}{dr_1^2 dr_2^2} \sim \exp[-a_1 r_1^2 + a_2 r_2^2]\, J_0(i\, b\, r_1 r_2)$$

expression and extract b. The analysis made with $\bar{p}p$ at 5.7 GeV/c showed that the correlation parameter $|b|$ is significantly greater for $\pi^+\pi^-$ pairs than for the $\pi^\pm\pi^\pm$ ones as given in the Table 7.1[59].

TABLE 7.1 - Values of the $|b|$ parameter for $\bar{p}p$ annihilation into pions at 5.7 GeV/c

Final state		$\|b\|$ $(GeV/c)^{-2}$
$3\pi^+3\pi^-$	$\pi^\pm\pi^\pm$	1.2 ± 0.2
	$\pi^+\pi^-$	2.0 ± 0.2
$3\pi^+3\pi^-\pi^o$	$\pi^\pm\pi^\pm$	1.0 ± 0.2
	$\pi^+\pi^-$	2.0 ± 0.1
$4\pi^+4\pi^-$	$\pi^\pm\pi^\pm$	1.0 ± 0.6
	$\pi^+\pi^-$	3.0 ± 0.4
$4\pi^+4\pi^-\pi^o$	$\pi^\pm\pi^\pm$	0.6 ± 0.3
	$\pi^+\pi^-$	2.8 ± 0.3

This is exactly what one would expect from a multi-Regge model, as any correlation should be more important for adjacent particles (i.e. $\pi^+\pi^-$ or $\pi^\pm\pi^o$) along the multipheripheral chain than for others ($\pi^\pm\pi^\pm$).

The approach discussed has the advantage of defining a quantity which measures the intensity of the two-particle correlation in the transverse plane. However, the form chosen for the two-particle density $dN/(d\vec{r}_1 d\vec{r}_2)$ is not really based on a model. Nevertheless, by analysing data which the above method, one obtains results which are in agreement with multiperipheral models. The method is all the more interesting since in some cases (as in limited transverse momentum

phase space) one can appreciate the correlation introduced by the kinematical constraints[60]. An alternative point of view to the present discussion can also be taken. Indeed assuming that multiperipheral graphs are responsible for the annihilations, the values for b given in Table 7.1 show clearly that the dominant exchange is the nucleon trajectory (and not the Δ one).

7.3 - Annihilation at high energy

At high energy the main question which has to be solved is how will we define an annihilation event when the $\bar{N}N$ pair production becomes important. The study of the production of $\bar{\Lambda}\Lambda$ pairs in $\bar{p}p$ and pp interactions seems to indicate that the Λ and $\bar{\Lambda}$ are produced close in rapidity[40,61]. A comparison between $\bar{p}p$ and pp data at 100 GeV/c shows in addition that the excess of $\bar{\Lambda}\Lambda$ in $\bar{p}p$ interactions seems to come from central production. If one still assumes that the difference between $\bar{p}p$ and pp in $\bar{\Lambda}\Lambda$ production is due to annihilation one may conjecture that the $\bar{N}$ and N will also be produced centrally and close in rapidity. This may as well be not the case if one believes that the Λ and $\bar{\Lambda}$ are produced close in rapidity to minimize the flow of quantum numbers (Fig.7.2)) along the rapidity axis (the particles being ordered as in multiperipheral models according to rapidity). Then the $\bar{\Lambda}$ and Λ (or $\bar{N}$ and N) will be produced close in rapidity to minimize the flow of the baryonic number in pp interactions, while the $\bar{B}$ and B will tend to be separated by large rapidity gap in $\bar{p}p$ interactions.

That such a mechanism may exist is also supported by the study of the charge structure of the final state in high-energy reactions[62]. The data show a tendency of the charge to be locally conserved in the rapidity space. This simply means that the total charge flow along the rapidity axis tends to be small. A way of measuring the total charge flow has been proposed in the study of pn interactions at 200 GeV/c[62] by using collective variables evaluated event by event. In particular, one can consider the variable $V_1 = \Sigma_i |Q_i|$, the sum running over all the rapidity gaps in a given event as shown in Fig.7.6. The average value $\langle V_1 \rangle$ is displayed in Fig.7.6 as a function of n, the number of charged outgoing particles. That $\langle V_1 \rangle$ increases with n is an expected result. This merely means that the total charge flow increases with n or the number of gaps, although $\langle V_1 \rangle$ is smaller than the statistical model predictions. One can consider the more interesting weighted variable $V_2 = \Sigma_i |Q_i| \Delta y_i / (\Sigma_i \Delta y_i)$, where Δy_i is the width of the rapidity gap carrying the charge Q_i. The sum $\Sigma \Delta y_i$ is the length of the total rapidity interval calculated for each event. The V_2 variable

has the property of minimizing the contribution of particles closely spaced in rapidity where the ordering procedure may be incertain or where the particles come from the same cluster or resonance. As can be seen from Fig.7.6 the averages $\langle V_2 \rangle$ all have small values (i.e. $\langle V_2 \rangle \leq 1$). This clearly indicates that there is a limited charge flow in a given event whenever the rapidity gaps are large.

Thus if one really believes that particles are produced in such a way that a minimal flow of quantum numbers occurs along the rapidity axis we are faced with the following problem. In the case of $\bar{N}N$ production the $\bar{N}$ and N will tend to be pushed away in the rapidity space for $\bar{p}p$ interactions so that the total baryonic flow should decrease (Fig.7.2). If this should be the case one would still have difficulty in separating such an event from a non-annihilation one. Therefore the question whether or not annihilation presents at high energy will still be settled by means of reactions (if any) in which no baryon are present in the final state. Thiw will give a lower limit of annihilation cross-section and needs an experimental device allowing the veto of events with $\bar{p}p$, $\bar{p}n$, $\bar{n}p$, or $\bar{n}n$ in the final state. Furthermore, exclusive annihilation channels will also be of great help to determine whether of not annihilation persists at high energy.

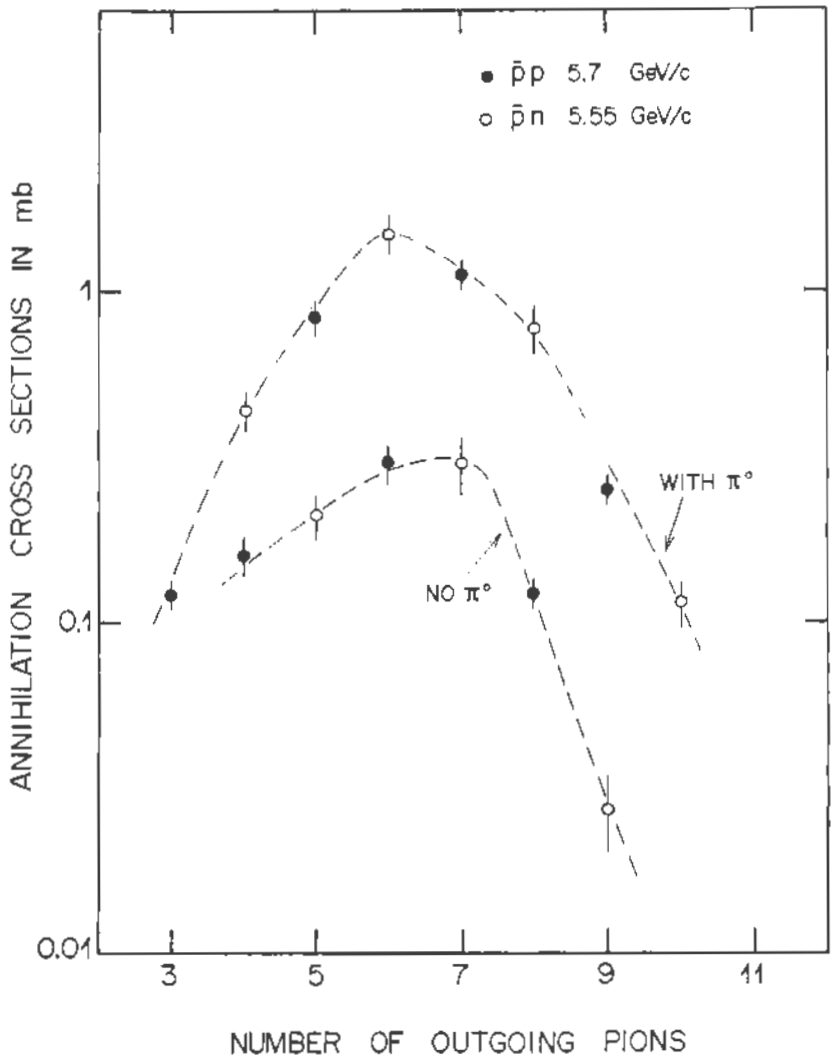

Figure 7.1

Comparison of the $\bar{p}p$ and our $\bar{p}n$ cross sections as a function of the number of outgoing pions for reactions having at most one π^0 in the final state. The curves are drawn to guide the eye [Ref.54].

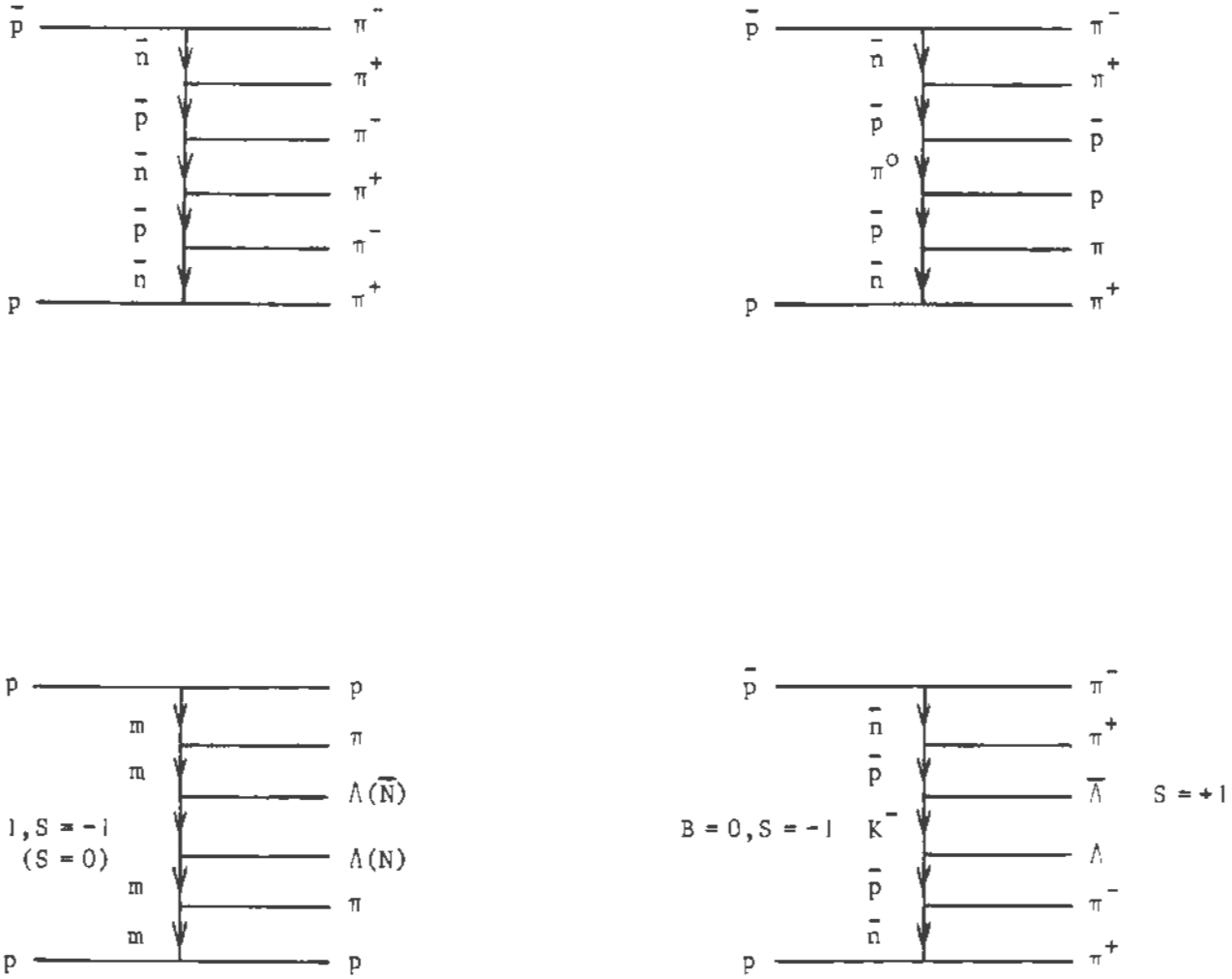

Figure 7.2

Multiperipheral graphs which may contribute to $\bar{p}p$ annihilations and to $\bar{B}B$ production in $\bar{p}p$ and pp interactions.

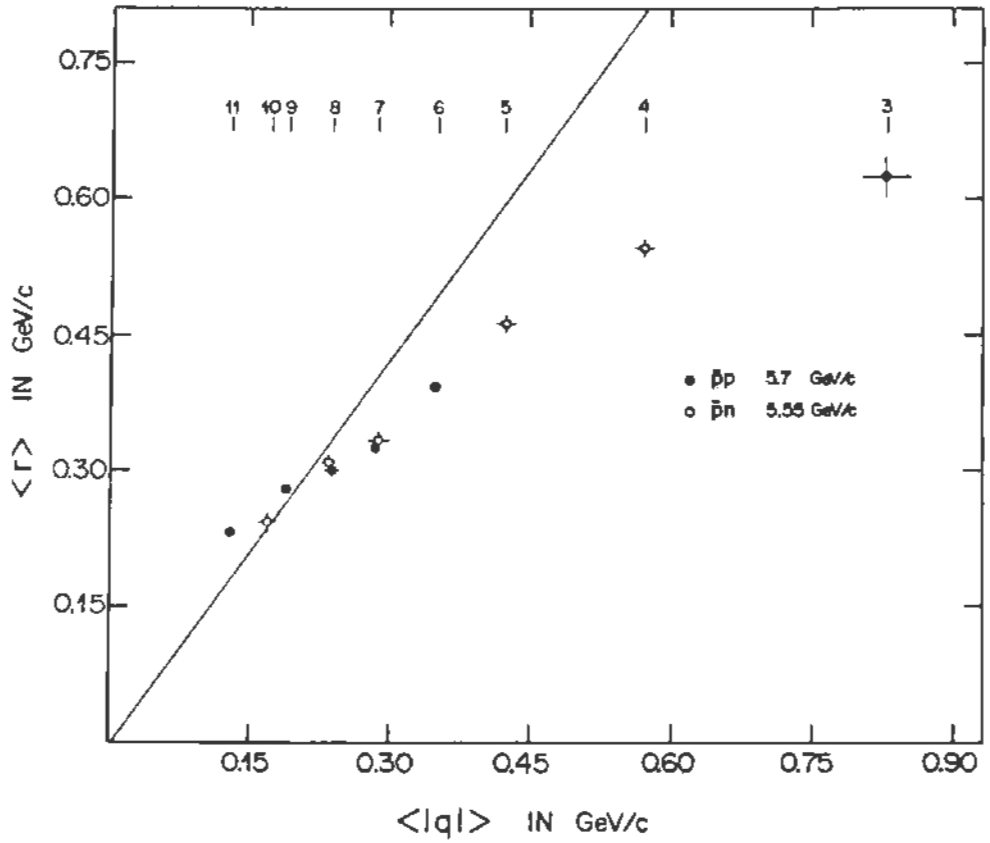

Figure 7.3

The average of the transverse momenta of the emitted π [$\langle r \rangle$] versus the average of their absolute c.m. longitudinal momenta [$\langle |q| \rangle$]. The straight line corresponds to an isotropic emission of the π. The numbers in the top of the figure represent the number of outgoing pions associated to each data point [Ref.54].

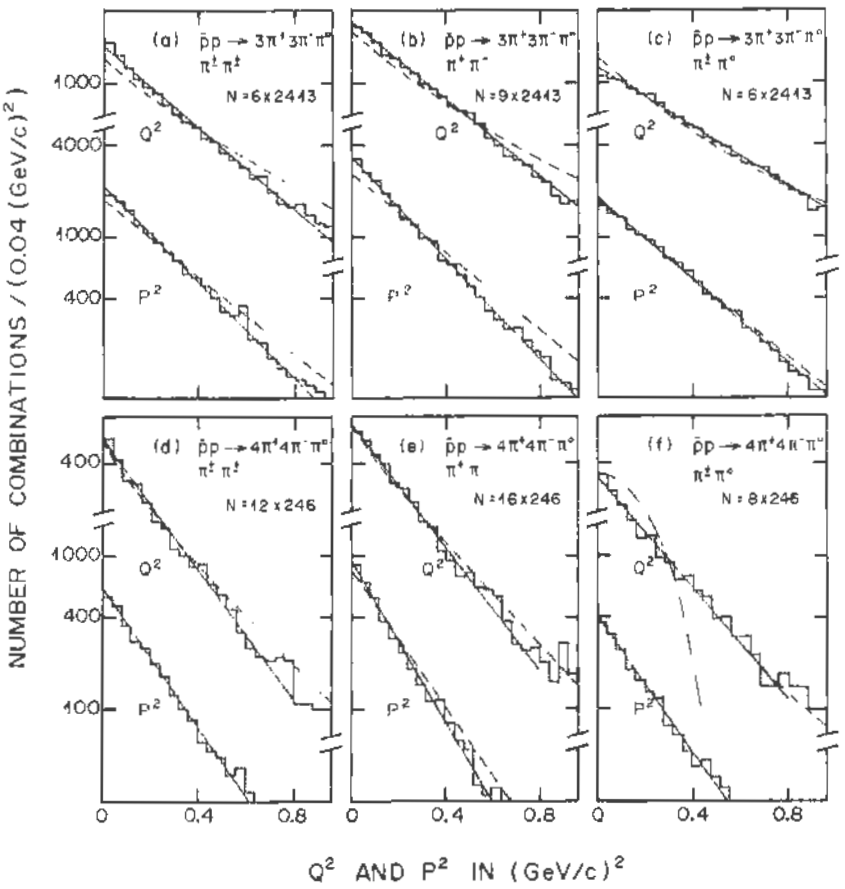

Figure 7.4

The P^2 [$P^2 \equiv P_+^2 = (\vec{r}_1 + \vec{r}_2)^2$] and Q^2 [$Q^2 \equiv P_-^2 = (\vec{r}_1 - \vec{r}_2)^2$] distributions for the like and unlike pions pairs. In (d) and (f) the phase space predictions (dashed curves) are nearly identical with the fitted dN/dP^2 distributions (full curves). The dot-dashed line in (f) is obtained from a pair of decay pions coming from the ω in the generated $\bar{p}p \to \omega\, 3\pi^+3\pi^-$ events [Ref.59].

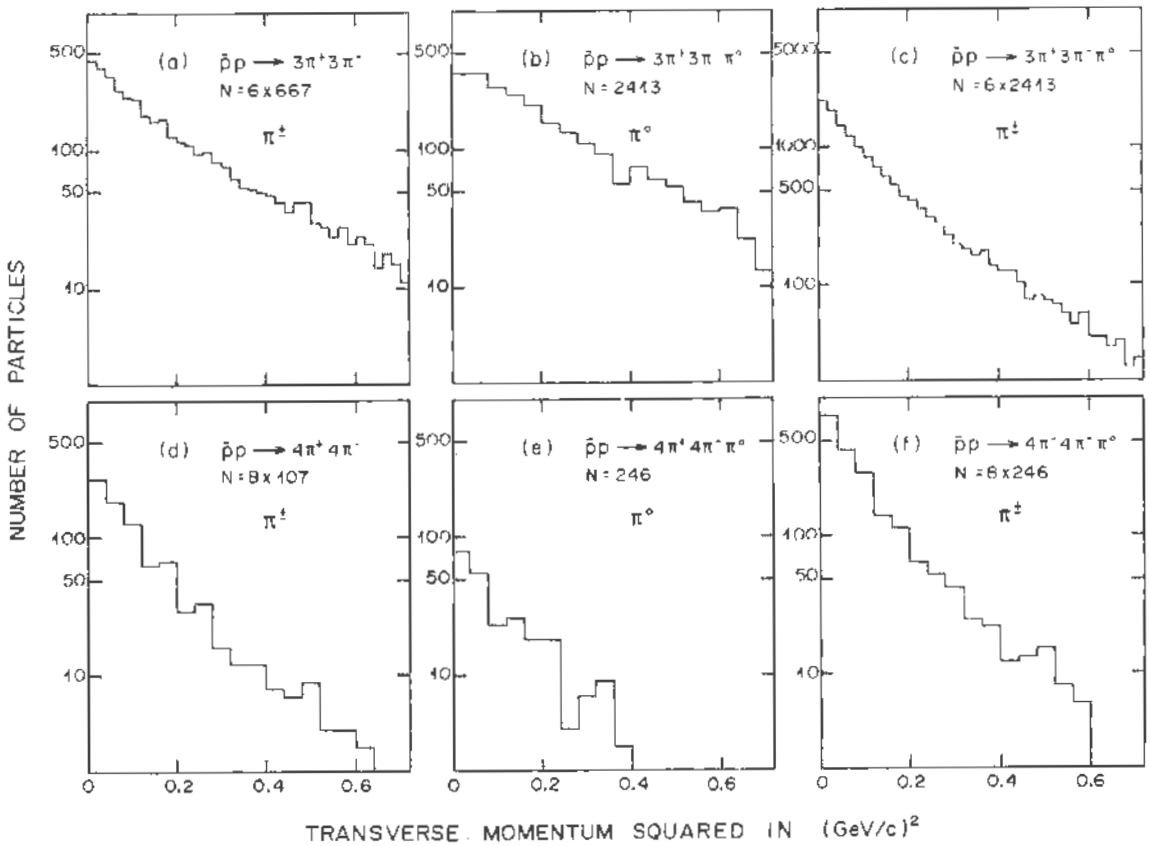

Figure 7.5

Single - π transverse momentum squared distributions obtained from the channels under study.

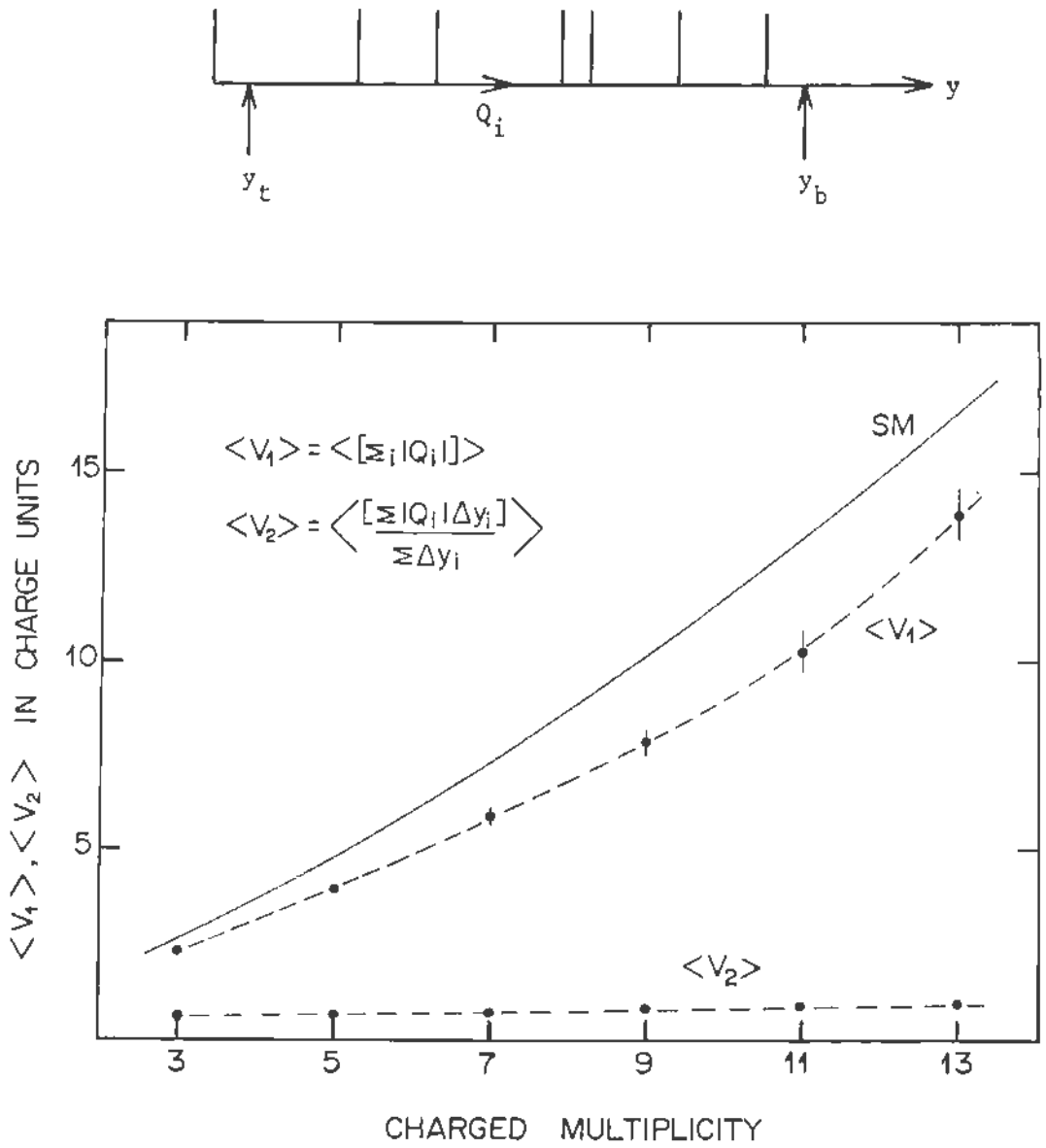

Figure 7.6

Diagram (top) representing the rapidity configuration of an event . The vertical lines represent outgoing particles while y_t and y_b are the rapidity of the target and the beam, respectively. The averages of the collective variables V_1 and V_2 (bottom) used to evaluate the total charge flow in an event. The dashed lines are drawn to guide the eye while the full line is the statistical model prediction [Ref.62].

References

1). A. Pais, Phys. Rev. Lett , 3, 243 (1959)

2). L. Hulthen and N. Sugawara, Structure of Atomic Nuclei (Encyclopedie of Physics, Vol. 39, 1957, Springer Verlag)

3). G.F. Chew, Phys. Rev., 80, 196 (1950) ; G.F. Chew and F.E. Low, Phys. Rev., 113, 1640 (1959)

4). See reference (2) and : M.J. Moravcsik, Nucl. Phys., 7, 113 (1958), I.J. McGee , Phys. Rev., 151, 772 (1966) and T. Hamada and I.D. Johnston, Nucl. Phys., 34, 382 (1962) and J.E. Elias et al., Phys. Rev., 177, 2075 (1969)

5). A. Fridman et al., Phys. Rev., D12, 3414 (1975)

6). A. Fridman, Fortschritte der Physik, Band 23, 244 (1975)

7). R.J. Glauber, Phys. Rev., 100, 242(1955)

8). This expression violates isospin invariance. Instead a sligthly different expression can be used which fulfil isospin conservation ; C. Wilkin, Phys. Rev. Letters, 17, 561 (1966)

9). V. Franco and R.J. Glauber, Phys. Rev., 142, 1195 (1966)

10). H. Braun, D. Brick, A. Fridman, J-P. Gerber, E. Jegham, P. Juillot, and C. Voltolini, Phys. Rev., D10, 3573 (1974)

11). H. Braun, A. Fridman, E. Jegham, P. Juillot, A. Malko, C. Voltolini, G.R. Charlton, W.A. Cooper, B. Musgrave, Nucl.Phys., B54, 61 (1973)

12). Dubna - Moscow - Kosice - Strasbourg - Tbilissi - Warsaw Collaboration, V.V. Glagolev et al., to be published in Phys. Rev. C (1978)

13). A. Astbury , Proceedings of the Antiproton Symposium p.46, Liblice - Prague, 1974, CERN 74-18 Yellow Report

14). E. Eisenhandler, Proceedings of the III European Antiproton Symposium, p. 91, 1976, published by Pergamon Press, Wenner - Green, Vol.29

15). R.J. Abrams, R.L. Cool, G. Giacomelli, T.F. Kycia, B.A. Leontic, K.K. Li and D.N. Michael, Phys. Rev., D1, 1917 (1970)

16). A.S. Carrol, I.H. Chiang, T.F. Kycia, K.K. Li, P.O. Mazur, D.N. Michael, P. Mockett, D.C. Rahm and R. Rubinstein, Phys. Rev. Lett., 32, 247 (1974)

17). See the following report and references quoted there :
L. Montanet, paper submitted to the V International Conference on Experimental Meson Spectroscopy hold at Boston, 1977, CERN/EP/PHYS 77-22 Report

18). E. Eisenhandler et al., Nucl. Phys., B113, 1 (1976)

19). V. Chaloupka et al., Phys. Rev. Lett., 32, 247 (1974)

20). J. Alspector, K.J. Cohen, W.C. Harrison, B. Maglic, F. Sannes, D. Van Harlingen, G. Cvijanovich, M. Martin and J. Oostens, Phys. Rev. Lett. 30, 511 (1973)

21). A.A. Carter, M. Coupland, E. Eisenhandler, W.R. Gibson, P.I.P. Kalmus, D.P. Kimber, A. Astbury and D.P. Jones, Phys. Lett., 67B, 117 (1977)

22). H. Braun, A. Fridman, J-P. Gerber, A. Givernaud, R. Kahn, G. Maurer, A. Michalon, B. Schiby, R. Strub, C. Voltolini, Nucl.Phys., B30,713 (1971)

23) E.L. Berger, Phys. Rev. D11, 3214 (1975)

24). Strasbourg data, to be published

25). H. Braun, D. Brick, A. Fridman, J-P. Gerber, P. Juillot, G. Maurer, A. Michalon, M-E. Michalon-Mentzer, C. Voltolini, Phys. Lett., 60B, 481 (1976)

26). A. Apostolakis et al., Phys. Lett., 66B, 125 (1977)

27). S. Nillson, Proceedings of the Antiproton Symposium, p. 189, Liblice-Prague 1974, Yellow Report CERN 74 - 18

28). P. Benkheiri et al., Phys. Lett., 68B, 483 (1977)

29). G. Yekutieli et al., Phys. Rev. Lett., 25, 184 (1970)

30). E.L. Berger and R.A. Morrow, Phys. Rev. Lett., 25, 1136 (1970)

31). H.W. Atherton, L.M. Celnikier, B.R. French, B. Ghidini, L. Mandelli, J.P. Moebes and E. Quercigh, Phys. Lett., 42B, 522 (1972)

32). H. Braun, A. Fridman, J-P. Gerber, A. Givernaud, P. Juillot, J.A. Malko, G. Maurer, A. Michalon, B. Schiby, C. Voltolini, Phys. Rev., D6, 2311 (1972)

33). P. Juillot, Proceedings of the III European Antiproton Symposium, p. 403 (1974) published by Pergamon Press, Wenner-Green, Vol. 29

34) A. Fridman, Proceedings of the Antiproton Symposium, p.248, Liblice - Prague, 1974, Yellow Report CERN 74 - 18

35). H. Braun et al., Phys. Rev., D2, 488 (1970)

36). See for instance : L. Jauneau, Introduction to Regge poles. Lectures given in the International Herceg - Novi School (1964) and published by the Centre de Recherches Nucléaires de Strasbourg

37). LBL $\bar{N}N$ and $\bar{N}d$ compilation, J.E. Enstrom et al., Particle Data Group, Lawrence Berkeley Laboratory, LBL - 58 (1972)

38). A.S. Carrol et al., Phys. Lett., 61B, 303 (1976)

39). V. Barger, Proceedings of the XVII International Conference on High Energy Physics, London 1974 (Science Research Council, UK,1974) p. I-193

40). J.G. Rushbrooke, Proceedings of the III European Antiproton Symposium, Stockholm, 1976 (Pergamon Press, London, 1976) p. 277

41). A. Fridman, Proceedings of the VIII International Symposium on Multiparticle Dynamics (Kaysersberg, 1977) p. A129

42). Y. Eylon and H. Harari, Nucl. Phys., B80, 349 (1974)

43). V. Simak, On the antihyperon annihilation in the quark model, Contribution to the VIII International Symposium on Multiparticle Dynamics (Kaysersberg, 1977)

44). A. Fridman, Introduction lecture to multiparticle production, published by the CRN de Strasbourg in the "Série de Cours et Conférences sur la Physique des Hautes Energies, n° 11 (1976)

45). A. Fridman, Proceedings of the III European Antiproton Symposium, Stockholm, 1976 (Pergamon Press, London, 1076) p. 409

46). A. Wroblewski, Acta Phys. Pol., B4, 857 (1973)

47). A.J. Buras, J. Dias de Deus and R. Møller, Phys. Lett., 47B, 251 (1973)

48). S.J. Orfanides and V. Rittenberg, Nucl. Phys., B59, 570 (1973)

49). B.R. Webber, Nucl. Phys. B117, 445 (1976)

50). S. Barshay, A. Fridman and . Juillot, Phys. Rev., D15, 2702 (1977)

51). H. Bøggild et al., Nucl. Phys., B27, 285 (1971)

52). Strasbourg - Weizmann Collaboration, Y. Eisenberg et al., Phys. Rev., Lett., 38, 108 (1977)

53). S. Barshay, Phys. Lett., 42B, 457 (1972)

54). H. Braun, A. Fridman, P. Fischer, J-P. Gerber, P. Juillot, G. Maurer, A. Michalon, M-E. Michalon-Mentzer and C. Voltolini, Proceedings of the European Antiproton Symposium, Stockholm, 1976 (Pergamon Press, London, 1976) p. 337

55). B. Margolis, Proceedings of the III European Antiproton Symposium, Stockholm, 1976 (Pergamon Press, London, 1976) p. 223

B. Margolis, W.J. Meggs and N. Weiss, Phys. Rev., D13, 2551 (1976)

56) G.T. Rossi and G. Veneziano, Nucl. Phys., B123, 507 (1977)

57). H. Braun, P. Fischer, A. Fridman, J-P. Gerber, P. Juillot, G. Maurer, A. Michalon, M-E. Michalon - Mentzer and C. Voltolini, Phys. Rev., D15, 1293 (1977)

58). H. Braun, A. Fridman, J-P. Gerber, A. Givernaud, P. Juillot, J.A. Malko, G. Maurer, A. Michalon, B. Schiby, R. Strub and C. Voltolini, Phys. Rev., D7, 3243 (1973)

59). H. Braun, A. Fridman, J-P. Gerber, P. Juillot, J.A. Malko, G. Maurer, A. Michalon and M-E. Michalon-Mentzer, Phys. Rev., D8, 2034 (1973)

60). A. Fridman and P. Juillot, Z. Physik, 268, 317 (1974)

61). D.R. Ward et al., Phys. Lett., 62B, 237 (1976)

62). Strasbourg - Weizmann Collaboration, Charge structure and correlation features in pn multiparticle final states at 195 GeV/c, H. Braun et al. in press Phys. Rev. D (1978)